



RETURNING MATERIALS:

Place in book drop to  
remove this checkout from  
your record. FINES will  
be charged if book is  
returned after the date  
stamped below.

--	--	--

HIGH ENERGY GAMMA RAYS IN INTERMEDIATE  
ENERGY NUCLEUS-NUCLEUS COLLISIONS

By

Kevin Breckenridge Beard

A DISSERTATION

Submitted to  
Michigan State University  
in partial fulfillment of the requirements  
for the degree of

DOCTOR OF PHILOSOPHY

Department of Physics

1986

ABSTRACT

HIGH ENERGY GAMMA RAYS IN INTERMEDIATE  
ENERGY NUCLEUS-NUCLEUS COLLISIONS

By

Kevin Breckenridge Beard

During an experiment to measure charged pion production for  $^{14}\text{N} + \text{Cu}$  collisions at  $E/A = 40$  MeV using an Enge split-pole magnetic spectrograph, a much larger than expected background of high energy electrons and positrons was observed. By comparison of the target-in to target-out spectra, it was deduced that most of the leptons were produced by gamma rays which were converted to electron-positron pairs in the material of the entrance aperture of the spectrograph. An experiment was constructed and carried out to determine the photon, electron, and positron yield.

The method for the detection of the high energy gamma rays was to convert the photons to electron-positron pairs immediately at a stopping Cu target. The energy spectrum of the electrons and positrons was measured using a magnetic spectrograph with specially constructed multiwire proportional counter plus Cherenkov detectors. The beam was

$^{14}\text{N}$  accelerated by the National Superconducting Cyclotron Laboratory K500 cyclotron to an energy  $E/A = 40$  MeV. Use of three converter elements with very different conversion efficiencies permitted the separation of the yield of electrons and positrons due to the pair conversion of gamma rays from that originating in the collision. The direct yield of  $e^+e^-$  pairs is less than 2% of the gamma yield.

An improved experiment using a telescope of active converter backed by a stack of Cherenkov counters was then used to measure the high energy gamma rays for  $^{14}\text{N}+\text{Pb}$ ,  $\text{Zn}$ , and  $\text{C}$  at  $E/A=40$  MeV, and  $^{14}\text{N}+\text{Pb}$  at  $E/A=30$  MeV. The cross sections are nearly isotropic. For gamma rays of energy  $E_\gamma > 20$  MeV,  $\sigma_{^{14}\text{N}+\text{Pb}} = 0.3$  mb.

The gamma ray cross section is compared to the neutral pion cross section allowing for the difference in mass and phase space; the two appear quite similar. Several theoretical models are compared to the data.

DEDICATION

To my wife, Jan.

s  
es  
a  
M  
E

## ACKNOWLEDGEMENTS

This work has been supported through the efforts of the staff of the National Superconducting Cyclotron Laboratory, especially Drs. W.Benenson, J.Stevenson, J.van der Plicht, and J.Yurkon. Additional support from my parents, Dr. and Mrs. G.B.Beard, grandparents, Mr. and Mrs. W.Roehling, and my wife Janet M. Hodgson-Beard is gratefully acknowledged.

## TABLE OF CONTENTS

LIST OF TABLES.....	vii
LIST OF FIGURES.....	viii
Chapter 1 - Introduction.....	1
Chapter 2 - The Pion Experiment and the Observation of High Energy Electrons and Positrons.....	7
2.1 Pion Production in Nucleus-Nucleus Collisions..	7
2.2 Experimental Technique for the Pion Measurement	9
2.3 Results of the Pion Experiment.....	16
2.4 The First Electron and Positron Experiment.....	18
Chapter 3 - The Positron Experiment.....	21
3.1 The Converter Concept.....	21
3.2 Modifications to the Spectrograph and Scattering Chamber.....	24
3.3 Changes in the Detector.....	26
3.4 Verification Tests.....	29
3.5 Results.....	29
Chapter 4 - Analysis of the $e^{\pm}$ Experiment.....	39
4.1 Introduction and an Example of a Monte Carlo Calculation.....	39
4.2 Modelling the Detector Efficiency.....	45
4.2.1 Verification Tests.....	53
4.3 The Pair Production Cross Section.....	53
4.4 Other Processes.....	59
4.5 Modeling of the Target and Converter.....	61

Chapter 5 - Gamma Ray Telescope Experiment.....	68
5.1 Introduction.....	68
5.2 The Design of the High Energy Gamma Ray Telescope.....	70
5.3 The Experiment.....	74
5.4 The Results.....	76
Chapter 6 - Theoretical Models.....	83
6.1 Comparison of Photons and Pions.....	83
6.2 Coherent Bremsstrahlung.....	87
6.3 Hard Sphere Bremsstrahlung.....	93
6.4 Fireball.....	93
6.5 Incoherent Bremsstrahlung From the Fireball....	101
Chapter 7 - Conclusions.....	107
Appendix A - Theoretical Calculations.....	109
A.1 Bremsstrahlung.....	109
A.2 Hard Sphere Bremsstrahlung.....	116
A.3 Fireball.....	118
A.4 Incoherent Fireball Bremsstrahlung.....	121
Appendix B - Experimental Hardware.....	127
B.1 The Enge Split-Pole Spectrograph.....	127
B.1.1 General Relationships.....	127
B.1.2 Nonrelativistic Kinematic Corrections....	131
B.1.3 Exit Window.....	133
B.1.4 New Scattering Chamber and Aperture.....	133

B.2	General Design of the $\pi^\pm$ experiment.....	135
B.3	Experimental Electronics.....	141
B.3.1	The $\pi^\pm$ Experiment Electronics.....	143
B.3.2	The $e^\pm$ Experiment Electronics.....	146
B.3.4	The $\gamma$ Telescope Electronics.....	148
B.4	PCOS III Electronics.....	149
B.5	Delay Cards.....	152
Appendix C	- Detector Development and Design.....	154
C.1	MIW Counter.....	154
C.1.1	Introduction.....	154
C.1.2	MIW Prototypes.....	157
C.1.3	MIW IV.....	164
C.2	The $^{12}\text{C}(\alpha, p)^{15}\text{N}^*$ Test of the MIW.....	168
C.3	Scintillators.....	171
C.3.1	Introduction.....	171
C.3.2	Scintillator Design.....	172
C.4	Cherenkov Detectors.....	176
Appendix D	- Computer Codes.....	180
D.1	Acquisition Code.....	180
D.2	MIW Detector Simulation SCATTER and Subroutines.....	182
D.3	Pair Production Simulation GAMMATEE and Subroutines.....	198
LIST OF REFERENCES	.....	206

LIST OF TABLES	Page
2.1 Results of the first search for high energy electrons.....	19
4.1 Steps for the example Monte Carlo simulation....	44
4.2 Initial limits of the $e^+$ and $e^-$ distribution for the code SCATTER.....	48
4.3 Parameter T values taken from a fit to the difference in positron results between the Pb and Be converters.....	66
6.1 The angle between the original direction and the direction at impact for two nuclei just touching.....	92
6.2 Fireball parameters for $^{14}\text{N}+\text{Pb}$ at 40 MeV/u.....	97
6.3 Temperature of the fireball used in the incoherent bremsstrahlung model.....	102
B.1 General Specification of the Enge Spectrograph.....	128
C.1 MIW III Specifications.....	161
C.2. MIW connectors.....	161
C.3 MIW IV specifications.....	166
C.4 Dimensions of the active region of the scintillators.....	173

LIST OF FIGURES	Page
2.1 The original charged pion experiment.....	10
2.2 The original charged pion detector.....	11
2.3 Idealized particle identification plot; the dark regions represent the range of momenta selected by the magnetic spectrograph.....	14
2.4 Pion detector modified to identify energetic electrons and positrons.....	15
2.5 Particle identification plot from the first electron experiment.....	17
2.6 Particle identification plot with the requirement that the Cherenkov counter produce a signal in coincidence with the event..	17
3.1 Positron experiment concept; stopping target backed by photon converter.....	22
3.2 Configuration of the $e^{\pm}$ Experiment.....	25
3.3 Configuration of the $e^{\pm}$ Detector.....	27
3.4 Typical $e^{\pm}$ positron spectrum.....	30
3.5 Pulse height in Cherenkov#1 vs. pulse height in the E scintillator detector.....	32
3.6 The same as in 3.5. but with the requirement of a good angle in the MIW counter.....	32
3.7 The same as in 3.5. but with the additional requirement that Cherenkov#2 produced a pulse...	32
3.8 Electron yield as a function of electron energy for the three converters at $17^{\circ}$ .....	33
3.9 Positron yield as a function of positron energy for the three converters at $17^{\circ}$ .....	34
3.10 Positron yield as a function of positron energy for the three converters at $0^{\circ}$ .....	35



3

3

4.

4.

4.

4.

4.

4.

4.7

4.8

4.9

4.1

4.11

4.12

3.11	Positron yield as a function of positron energy for the three converters at 40°.....	36
3.12	Angular dependence of the high energy positron (70 - 105 MeV) yield for the three converters.....	37
4.1	A particle scattering through N thin identical slabs.....	40
4.2	Example probability distribution P( $\theta$ ).....	43
4.3	Integrated probability distribution F( $\theta$ ).....	43
4.4	Inverse of the integrated probability distribution F <sup>-1</sup> (X).....	43
4.5	Co-ordinate system used in the Monte Carlo calculation.....	47
4.6	Calculated efficiency of the detector for electrons penetrating the scintillator and the first Cherenkov counter, and for electrons then penetrating the second Cherenkov counter.....	51
4.7	The calculated and measured effect of inserting a 1" aluminum plate between the Cherenkov counters.....	52
4.8	Differential pair production cross section in Pb for 20, 50, and 100 MeV photons.....	56
4.9	Total pair production cross section in Pb as a function of photon energy.....	58
4.10	Superposition of the difference in yield from the Pb and Be converter for electrons at 17°, positrons at 0°, 17°, and 40°. The solid lines are an assumed gamma ray spectrum with a slope parameter of 18 MeV and the resulting positron spectrum from the calculation.....	60
4.11	Typical plot of $\chi^2$ vs. slope parameter.....	64
4.12	The data points give the e <sup>±</sup> yield as a function of energy for <sup>14</sup> N + Cu at E/A=40 MeV for three different converters at $\theta_L = 17^\circ$ . The dashed curve shows an assumed gamma-ray yield based upon a thermal source and the solid curves show results of the Monte Carlo calculation for the conversion positrons.....	65

5.1	Concept of the High Energy Gamma-Ray Telescope..	69
5.2	Efficiency of the CsI converter as a function of gamma-ray energy.....	71
5.3	The High Energy Gamma-Ray Telescope.....	73
5.4	Output of the top phototube vs. output of the bottom phototube for a single element.....	75
5.5	Output of one element gated by a higher element.....	75
5.6	Gamma-ray cross section as a function of gamma-ray energy at $\theta_{\text{Lab}}=90^\circ$ for $^{14}\text{N}$ on Pb, Zn, and C at 40 MeV/u.....	77
5.7	Gamma-ray cross section as a function of gamma-ray energy for $^{14}\text{N}+\text{Pb}$ at 40 MeV/u at $\theta_{\text{Lab}} = 30^\circ, 90^\circ, \text{ and } 150^\circ$ .....	78
5.8	Gamma-ray cross section as a function of gamma-ray energy for $^{14}\text{N}+\text{C}$ at 40 MeV/u at $\theta_{\text{Lab}} = 30^\circ, 90^\circ, \text{ and } 150^\circ$ .....	79
5.9	Integrated gamma-ray cross section for $E_\gamma > 20$ MeV as a function of angle for $^{14}\text{N}+\text{C}$ , Zn, and Pb at 40 MeV/u.....	80
5.10	Gamma-ray cross section as a function of gamma-ray energy for $^{14}\text{N}+\text{Pb}$ at 40 and 30 MeV/u at $\theta_{\text{Lab}} = 90^\circ$ .....	81
6.1	Comparison of the high energy gamma-ray cross section and the neutral pion cross section multiplied by the relative phase space as a function of the total energy of the photon or pion.....	84
6.2	System used in the coherent bremsstrahlung calculation.....	88
6.3	Cross section for the coherent bremsstrahlung model as a function of gamma-ray energy for $^{14}\text{N}+\text{Pb}$ at 40 MeV/u and $\theta_{\text{Lab}} = 90^\circ$ with stopping times of 10, 15, and 20 fm/c.....	90
6.4	Cross section for $^{14}\text{N}+\text{Pb}$ at 40 MeV/u as a function of lab angle for $E_\gamma = 40$ MeV using the coherent bremsstrahlung model with $\tau=15$ fm/c.....	91



6

5

3.

.

.

.

.

2

3

4

5

6

7

8

9

0

1

2

6.5	Cross section for $^{14}\text{N}+\text{Pb}$ at 40 MeV/u and $E_\gamma = 50$ MeV using the hard sphere bremsstrahlung model for various maximum impact parameters.....	94
6.6	Cross section for $^{14}\text{N}+\text{Pb}$ at 40 MeV/u and $\theta_{\text{Lab}} = 30^\circ$ using the hard sphere bremsstrahlung model with the maximum impact parameter 37% of the radii.....	95
6.7	Cross section for $^{14}\text{N}+\text{Pb}$ at 40 MeV/u and $\theta_{\text{Lab}} = 30^\circ$ using the fireball model.....	99
6.8	Cross section for $^{14}\text{N}+\text{Pb}$ at 40 MeV/u and $E_\gamma = 40$ MeV using the fireball model.....	100
6.9	Cross section for $^{14}\text{N}+\text{C}, \text{Pb}$ at $\theta_{\text{Lab}} = 90^\circ$ using the incoherent bremsstrahlung model.....	104
6.10	Cross section for $^{14}\text{N}+\text{Pb}$ at 40, 30 MeV/u using the incoherent bremsstrahlung model.....	105
B.1	The Enge split-pole magnetic spectrograph.....	129
B.2	The $\pi^\pm$ experimental configuration.....	136
B.3	The $\pi^\pm$ experiment detector.....	138
B.4	The $\pi^\pm$ experiment electronics.....	142
B.5	The $e^\pm$ experiment electronics.....	145
B.6	The High Energy Gamma-Ray Telescope electronics.....	147
B.7	Design of the delay cards.....	153
C.1	The Multi-Inclined Wire concept.....	156
C.2	The MIW counter.....	158
C.3	Operating voltages of the MIW III prototype using 1 atm 50-50 argon-ethane.....	163
C.4	Assembly view of the MIW IV counter.....	165
C.5	Spectrum of alpha particles from $^{12}\text{C}(\alpha, \alpha')^{12}\text{C}^*$ at $E_\alpha = 80$ MeV.....	169

C.6	Protons measured simultaneously using the reaction $^{12}\text{C}(\alpha, p)^{15}\text{N}$ .....	169
C.7	Scintillator and Cherenkov detector used in the $e^{\pm}$ experiment.....	175
C.8	Cherenkov element of the High Energy Gamma-Ray Telescope.....	178

## Chapter 1

### Introduction

This dissertation deals with the observation of high energy photons from intermediate energy nucleus-nucleus collisions. It includes the third and fourth in a series of experiments I participated in while a graduate student in Physics at the National Superconducting Cyclotron Laboratory (NSCL) at Michigan State University.

The first experiment in which I was heavily involved with at NSCL was my original thesis project, the use of the  $(d, {}^2\text{He})$  reaction to study certain transitions in nuclei [Ja76], [Be82]. The  ${}^2\text{He}$  system is unbound, but can be detected as a "diproton", two protons closely correlated in energy and direction. To use this reaction to examine a variety of nuclei, it was necessary to build a detector compatible with the NSCL Enge Split-Pole spectrograph and capable of identifying and measuring the position of two protons simultaneously. This need led to my development of the Multi-Inclined Wire detector, which is described in detail in Appendix C.

We carried out an experiment using the reaction  ${}^{12}\text{C}(d, {}^2\text{He}){}^{12}\text{B}$  with  $E_d = 99.2$  MeV at the Indiana University

11

Cy  
use  
pos  
cha  
(d,  
AT-  
ava  
tha  
tne  
one  
obe  
  
inv  
was  
rea  
ene  
May  
  
bea  
dia  
espe  
rec  
Ener  
by  
pio  
sto  
nee

Cyclotron Facility (IUCF). To measure the diprotons, we used two solid state detector telescopes mounted as close as possible to each other within the IUCF 60" scattering chamber. The goal of the experiment was to see if the  $(d, ^2\text{He})$  reaction would be a useful probe of  $\Delta T = \Delta |T_z| = \Delta S = \Delta J = 1, \Delta L = 0$  transitions at the higher energies available with the NSCL cyclotrons. The results indicated that  $(d, ^2\text{He})$  would be of limited usefulness as a probe at these higher energies, primarily because random proton pairs created by deuteron breakup into protons and neutrons obscures the diprotons.

I then participated in two very different experiments involving the production and detection of pions. The first was the measurement of the mass of  $^{59}\text{Zn}$  using the  $(p, \pi^-)$  reaction, and the second a measurement of the yield of energetic protons and pions from  $^{139}\text{La}$  on  $^{139}\text{La}$  at 246 MeV/u.

The  $^{58}\text{Ni}(p, \pi^-)^{59}\text{Zn}$  experiment used a 200 MeV proton beam at IUCF, and the QQSP spectrometer [Sh83], [Gr82]. The Quadrupole-Quadrupole Split-Pole spectrometer had been especially constructed to measure pions, and used a track reconstruction technique to obtain a large solid angle. Energetic electrons were a source of a large background, but by using an aluminum wedge to slow the pions, some of the pions stopped in the plastic scintillator. Those that stopped were absorbed into nuclei, causing the nucleus to receive 140 MeV of excitation, which then is released in a

variety of ways, forming a pion "star". The large energy released in the star was used as a signature of a pion.

The  $^{139}\text{La}$  pion experiment used the one arm of the TASS (Two Arm Spectrometer System) spectrometer at Lawrence Berkeley Laboratory [Kr86]. In our configuration, the track through the spectrometer was determined by three plastic scintillator hodoscopes. Separation of the pions, electrons, and protons was by virtual mass calculated from the momentum and time-of-flight through the spectrometer and by use of a water filled Cherenkov counter beyond the last hodoscope. Again, a large background of electrons and positrons was observed with the same momenta as the pions.

In the course of these experiments, I became curious as to the origin of these high energy electrons and positrons. The coincidence of both experiments having an electron rate comparable to the pion rate was remarkable, and I had no good idea of their source.

As third series of experiments began, my thesis project had become a measurement of the pion yield for  $^{58}\text{Ni}(^{14}\text{N}, \pi^{\pm})$  at 40 MeV/u. Production of pions with the beam energy per nucleon below that necessary for nucleon-nucleon pion creation ( $\sim 290$  MeV/u) is referred to as "subthreshold pion production", and is of interest as a measure of collective nuclear effects, where the energy of many nucleons is pooled to create a pion. Although first measurements in this energy range were made using neutral pions [Br84], the project was still interesting as a way of measuring the



r/r

that

velo

to a

exper

lowe

nece

backg

spec

chan

stop

chan

thro

posi

stop

part

the

the

numb

elec

Chan

sign

were

simi

expe

$\pi^-/\pi^+$  ratio. Previous work at high energy had discovered that the  $\pi^-/\pi^+$  ratio became very large for pions with velocity near the beam velocity, and had shown it to be due to a Coulomb effect[Be79]. Part of the motivation for this experiment was to determine if this effect persisted at much lower energy. Because of the small cross section, it was necessary to construct the system in such a way that background would be minimized.

The experiment used the NSCL Enge Split-Pole spectrograph[Sp67]. The beam entered the 14" scattering chamber, passed through a relatively thin target, and stopped in a water filled Faraday cup at the back of the chamber. The path for the pions passed through the slits, through the spectrograph, through a window and air, the MIW position sensitive detector, the  $\Delta E$  scintillator, and stopped in the E scintillator. Only pions and lighter particles would have sufficient range to reach the MIW for the field settings for 20-40 MeV pions.

While running the experiment in this configuration, a number of events were observed which were apparently electrons and positrons. To test this, a plexiglas Cherenkov counter was placed behind the  $\Delta E$ -E telescope. The signals from the Cherenkov counter confirmed that the events were indeed electrons and positrons of about 100 MeV, similar to the background I had observed in the other pion experiments.

Encouraged by recent theoretical models[Va84], we then attempted to measure the electron and positron yield as a function of their energy, but we found the rate to be nearly independent of whether the target was in or out of the beam. As discussed later, the electrons and positrons we saw were shown to have been created by pair conversion of very high energy gamma-rays from the Faraday cup. To measure the photon, positron, and electron flux from the target it was necessary to limit pair conversion to a well defined, calculable geometry.

The final experiment in this series used "converters" placed directly behind the target and demonstrated a relatively large cross section for the formation of very high energy photons, whose subsequent conversions in matter give rise to high energy electrons and positrons.

This surprising result, which indicates some cooperative process is taking place, has generated much theoretical interest, and further experiments are in progress at GSI in Europe[No85] and at NSCL.

The results of this experiment immediately led to the development of the fourth series of experiments, in which a specially constructed telescope, made of a stack of Cherenkov counters, was used to measure the high energy gamma spectrum for a variety of beam energies, targets, and angles[St85c]. The first of these experiments has been completed, and similar experiments looking for high energy  $\gamma$  - charged particle coincidences have been proposed.

At much higher beam energies[Bu81], energetic photons from the decay of the prolifically produced neutral pions mask these photons. At much lower energies, the production of high energy photons decreases rapidly, and can be hidden by neutron interactions in conventional detectors[Mo85]. The fortuitous choice of detector and system led to their observation.

## Chapter 2

### The Pion Experiment and the Observation of High Energy Electrons and Positrons

#### 2.1 Pion Production in Nucleus-Nucleus Collisions

The production of pions in nuclear collisions when the energy per nucleon is below the nucleon-nucleon threshold, usually referred to as subthreshold pion production, is the subject of recent experimental and theoretical study after a gap of thirty years since it was first proposed[Ri50]. The first manmade pions were produced at Berkeley[Ga48] in 1948, but until 1978 there was little data available.

When the incident nuclei have energy per nucleon well above the nucleon-nucleon threshold of 290 MeV (the nucleon-nucleon threshold), the production of pions by heavy ion collisions is well explained by the sum of the production by the individual nucleon-nucleon collisions. A class of calculations known as the cascade model use a Monte-Carlo technique to follow each nucleon throughout the collision, and has been successful describing many of the characteristics of these collisions. Nucleons within a nucleus are not at rest, but have a momentum distribution. Production of pions at energies per nucleon less than the

nucleon-nucleon threshold is energetically possible due to the additional energy available from the other nucleons.

It was found, however, that as the beam energy decreased, the pion production cross section did not fall as predicted. At energies of 25-50 MeV/u, the cascade model underpredicts pion production by many orders of magnitude[Sh84a]. Pion production has been observed near the absolute limit[St85a], the point at which there is just sufficient energy in the entire system to produce a pion.

Several theories have been advanced to explain this phenomenon, but all require the nucleus to show collective behavior. This collective behavior may give insight into the nuclear equation of state, and into the nature of nuclear matter far from equilibrium. Several models are discussed in Chapter 6.

At these "subthreshold" energies the collisions giving rise to the pions are of great interest, since the collective behavior is manifest. Moving source fits to a variety of emitted particles suggest that the region has about  $1/2$  the beam velocity, and about 2x the beam mass[Go77]. An additional discovery, made by Benenson et al., that the ratio of  $\pi^-/\pi^+$  becomes very large near  $0^\circ$  and the beam velocity, was explained as being due to Coulomb repulsion between the interacting region and the  $\pi^+$ [Be79].

The motivation for our pion experiment was to measure the  $\pi^\pm$  production cross section at a beam energy lower than had been done before, measure the angular distribution, and



inve  
enha

2.2

very

26 n

a gi

chang

stop

by t

many

emis

range

prod

spec

tang

absor

of t

with

reach

The b

pass

The s

seal,

investigate the  $\pi^-/\pi^+$  ratio to determine whether the enhancement effect persisted at much lower energies.

## 2.2 Experimental Technique for the Pion Measurement

Charged pions are produced at low beam energies with a very small cross section. The pion has a mean lifetime of 26 nS and a mass of 140 MeV. Because of its small mass, for a given energy it has a small  $\frac{dE}{dX}$ , a large range, and a large charge-to-mass ratio relative to a proton. In addition, the stopping  $\pi^-$  is absorbed by a nucleus, exciting the nucleus by the pion rest mass. Subsequent de-excitation takes place many ways forming a pion "star", the most common being the emission of several neutrons.

The  $\pi^\pm$  experiment used the fact that pions have a large range and charge-to-mass ratio relative to the more commonly produced hadrons such as p, d, t, and  $\alpha$ . A magnetic spectrometer separated the charged particles coming from the target according to their momentum-to-charge ratio, and absorbing matter in front of the detector on the focal plane of the spectrometer prevented protons and heavier particles with the same momentum but lesser range than the pions from reaching the detector.

The experimental configuration is shown in Figure 2.1. The beam of  $^{14}\text{N}^{+5}$  ions enters from the bottom of the figure, passes through the target, and stops in the Faraday cup. The spectrograph is connected to the target with a sliding seal, so the dipole is also under vacuum. Pions produced by



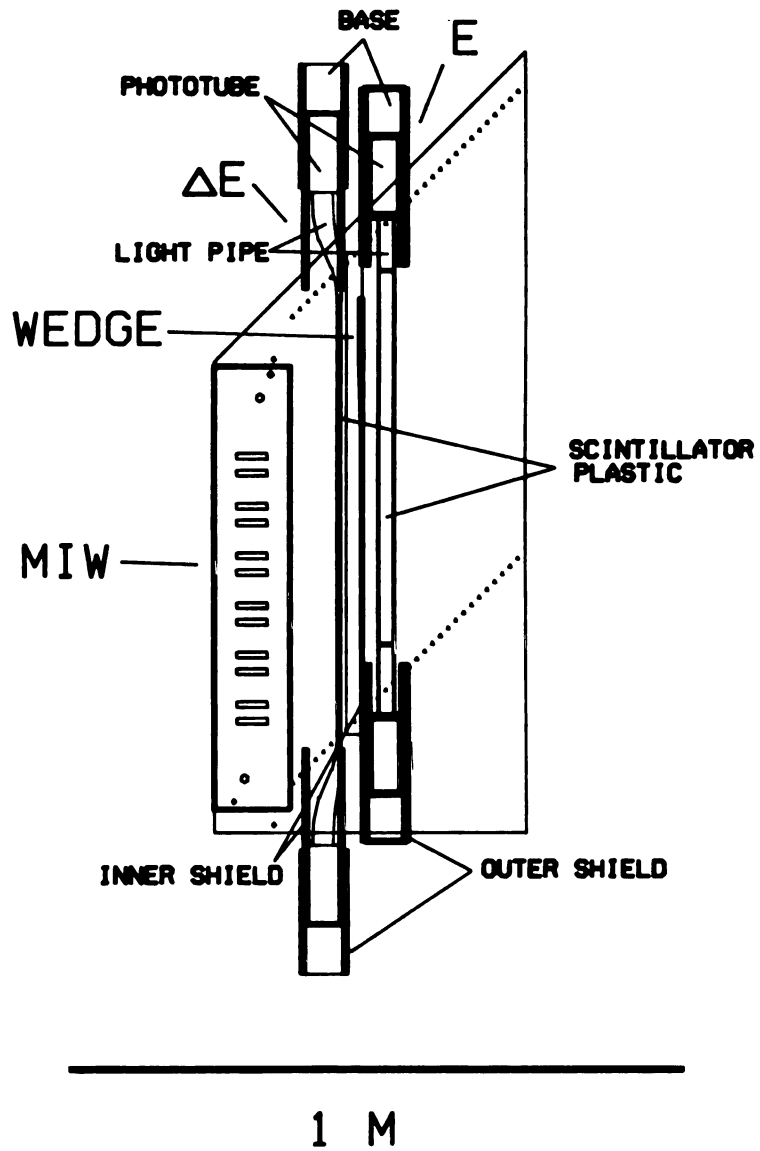


Figure 2.2. The original charged pion detector.



reactions in the target and which enter the spectrograph are bent by the magnetic field, exit the dipole and enter the camera box through a thin window. The camera box is at atmospheric pressure. The pions pass through the position sensitive counter, through the  $\Delta E$  plastic scintillator, through an aluminum wedge, and stop in the E plastic scintillator. The spectrograph and the experimental configuration are discussed in detail in Appendix B.

The detector consists of several components, the detail of which are in Appendix C. The Multi-Inclined Wire (MIW) detector measures a location on and the angle to the focal plane for each particle, and the  $\Delta E$ -E plastic scintillator telescope behind the focal plane detector provides an energy loss and energy signal for each particle (Figure 2.2).

The MIW detector is a multiwire proportional counter, designed and built specifically for the Enge spectrograph. It has two planes of 96 active wires which serve to determine both the position and angle of a particle. A particle passes through the thin front plastic window, through an active region filled with a gas, and out through the thin rear plastic window. The active region has an electric field, with a cathode on the bottom, and anode wires above. Free electrons created in the gas by the ionization caused by the passage of the particle drift up to the anode wires. The small diameter of the anode wires creates a very large electric field, where the number of free electrons is multiplied through collisions with the

gas. Each anode wire is electrically connected to its own amplifier outside the detector. In addition, a signal is induced on the cathodes. The energy loss resolution is poor; the small amount of energy deposited in the detector is not used for particle identification.

Behind the MIW are two plastic scintillators forming the particle identification telescope. The scintillator plastic converts a fraction of the energy deposited by the charged particles into light. Some of this light is contained by total internal reflection until it strikes photomultiplier tubes at either end of the scintillator, where it is converted into an electronic pulse.

The front scintillator, called  $\Delta E$ , is thin enough for the particle to pass through. The next scintillator, called E, stops the particle. A plot of  $\Delta E$  against E is used to identify the particles. Empirically (very similar to the Bethe equation), the energy loss of a nonrelativistic particle (heavier than the electron) in material is:

$$\frac{dE}{dX} \propto \frac{M^{0.8} Z^2}{E^{0.8}}$$

so that when particles enter the telescope, the plot appears as curved bands, but the limited range of momentum-to-charge ratio which reaches the detector breaks the bands into islands in the  $\Delta E$ -E plot, as illustrated in Figure 2.3.



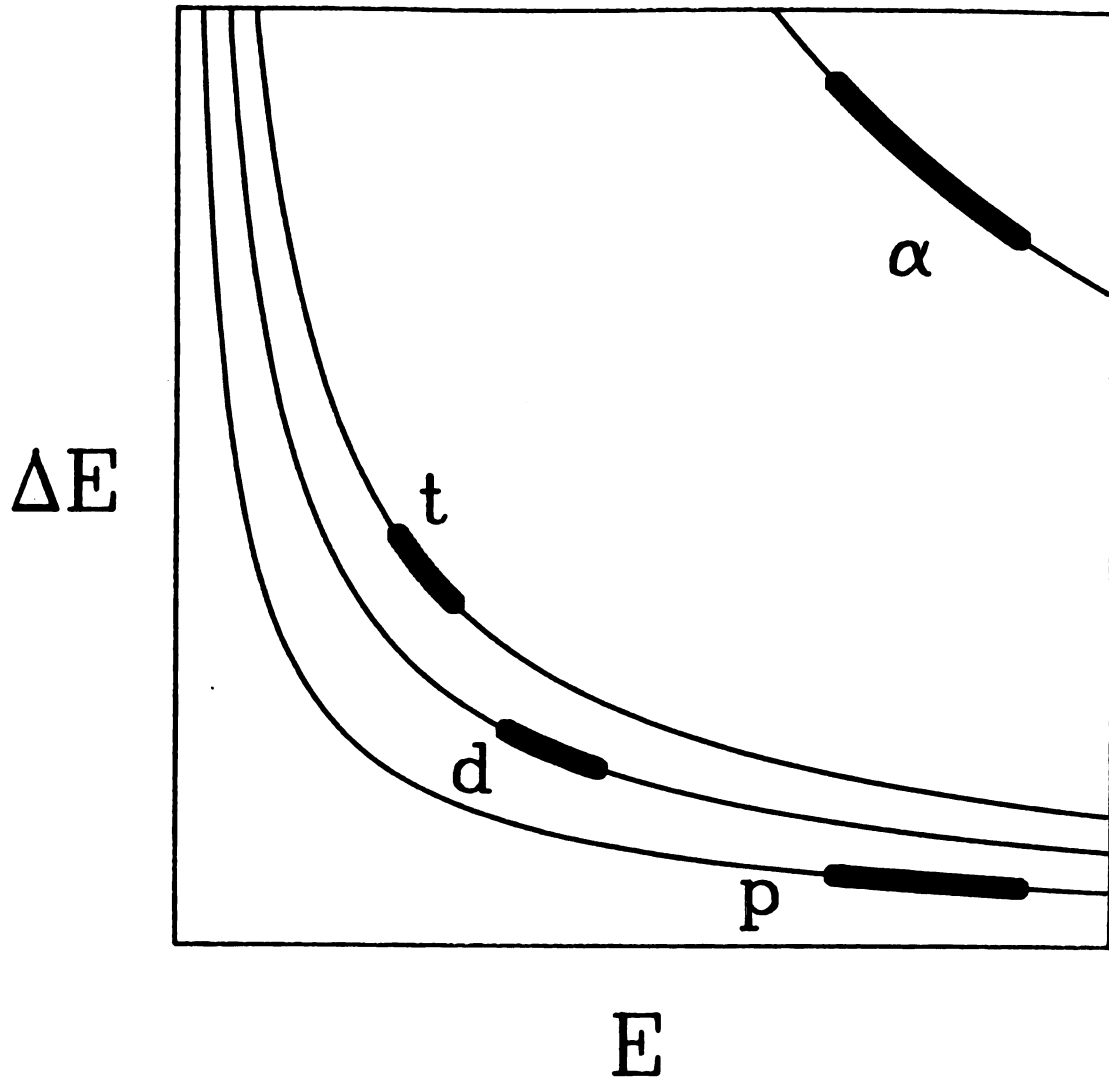


Figure 2.3. Idealized particle identification plot; the dark regions represent the range of momenta selected by the magnetic spectrograph.

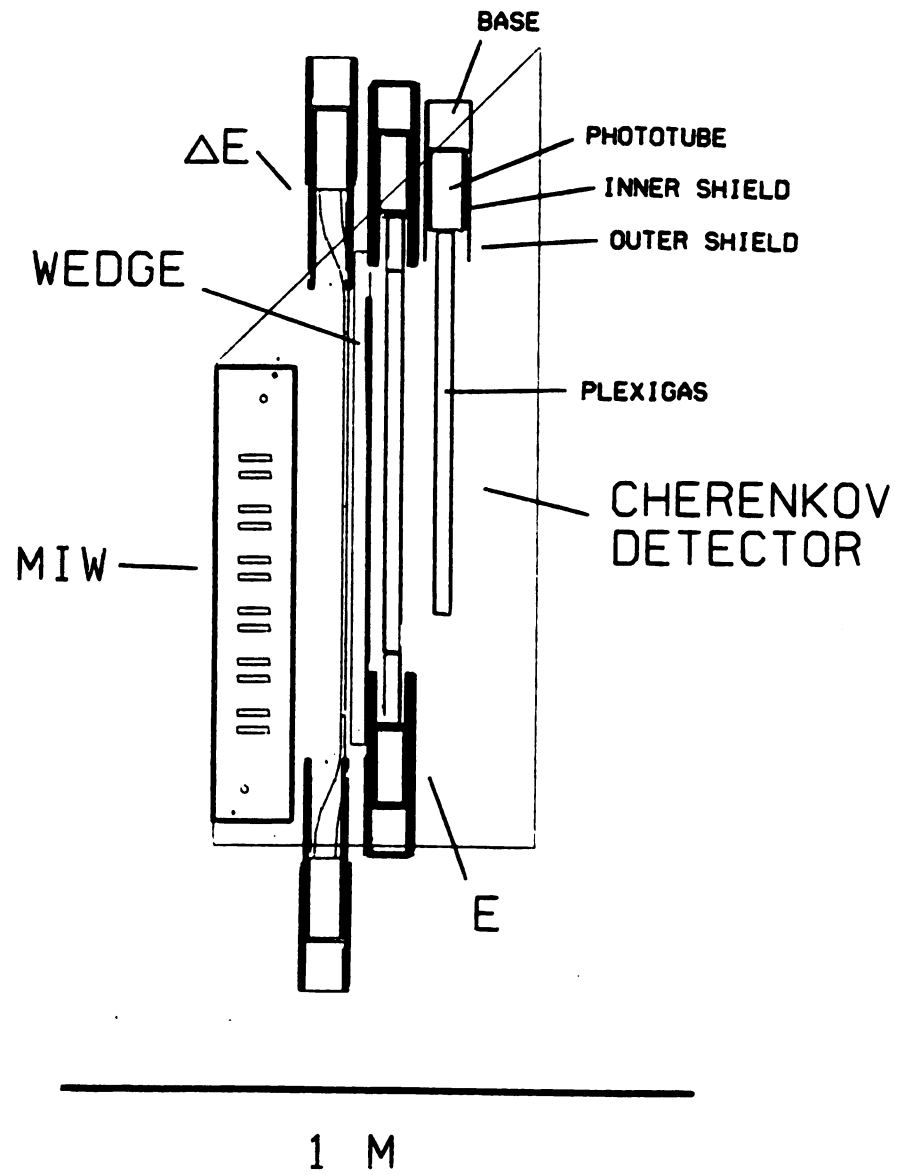


Figure 2.4. Pion detector modified to identify energetic electrons and positrons.

In the later runs, a Cherenkov detector was placed behind the  $\Delta E-E$  telescope (Figure 2.4). Cherenkov detectors, discussed in detail in Appendix C, use the light created in a material when the speed of a charged particle exceeds the speed of light in that medium. For the plexiglas used ( $n=1.5$ ), the speed of a particle needs to exceed  $c/n=.67c$  before any light is produced. The Cherenkov light is produced in a cone around the particle's path; in the Enge the path runs around  $45^\circ$  to the detector, so most of the internally reflecting light ends up at the high radius end of the detector, hence only one phototube was used. For particles that follow a proper orbit through the spectrograph, only  $e^\pm$  have sufficient velocity to produce a pulse in the Cherenkov detector.

### 2.3 Results of the Pion Experiment

Figure 2.5 shows a particle ID plot made during a pion run. Figure 2.6 shows the same data, but has the added requirement that there be a good track in the MIW position sensitive counter. These figures show that particles with low specific ionization were exiting the spectrograph, that these particles have a range of greater than 4.5 cm of plastic, and that these particles have a speed greater than  $.67c$  in the Cherenkov detector. A typical yield of 50 per hour for a beam current of 30 pA was observed, and zero with no beam. The only particles compatible with these

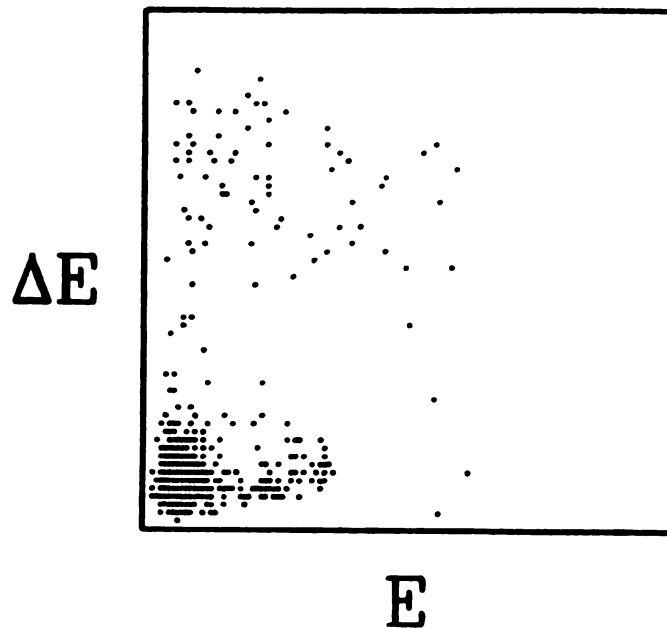


Figure 2.5. Particle identification plot from the first electron experiment.

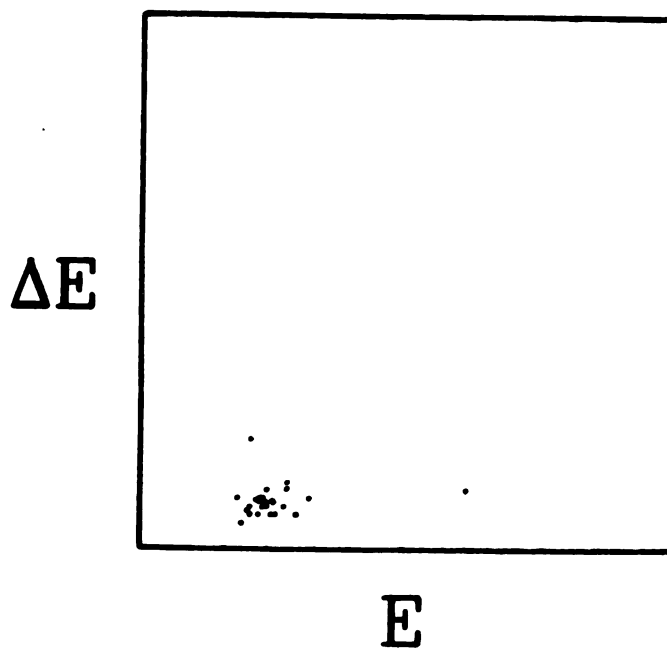


Figure 2.6. Particle identification plot with the requirement that the Cherenkov counter produce a signal in coincidence with the event.

conditions and the momentum selected by the spectrograph are electrons and positrons of around 100 MeV.

These results were obtained in June, 1984. In other pion experiments in which I had participated [Kr86], [Sh83], electrons and positrons have also been observed, but had been treated as uncharacterized background. While I had been curious as to their source, I failed to find an explanation which seemed plausible. At the same time, Walter Greiner, the well known nuclear theorist, came to NSCL and gave a talk on his theory of pionic bremsstrahlung [Va84]. His model made subthreshold pions through a process analogous to classical electromagnetic bremsstrahlung. When asked if these high energy electrons and positrons could also be produced by the acceleration, Dr. Greiner responded positively, and suggested an immediate measurement of these electrons and positrons.

#### 2.4 The First Electron and Positron Experiment

The experimental configuration previously used in the pion experiment remained unchanged, except for the target which was 60 mg/cm<sup>2</sup> natural nickel (67.95% <sup>58</sup>Ni, 26.10% <sup>60</sup>Ni, 1.13% <sup>61</sup>Ni, 3.59% <sup>62</sup>Ni, and 0.91% <sup>64</sup>Ni) [We81]. The polarity and field of the spectrograph were varied so electrons and positrons of 20-140 MeV could be measured. The lower limit of 20 MeV was chosen since multiple scattering of the  $e^{\pm}$  in the scintillator would drastically reduce the efficiency of these particles to reach the

Table 2.1. Results of the first search for high energy electrons.

<u>polarity</u>	<u>T<sub>e</sub>(MeV)</u>	<u>relative yield (cts/μC)</u>	
		<u>target in</u>	<u>out</u>
+	80 -111	8.9	9.4
+	38 - 52	9.0	9.9
+	22 - 31	9.5	10.1
-	22 - 31	11.5	12.5
-	38 - 52	11.6	12.8
-	80 -111	13.4	-

Cherenkov counter. The results of this run appear in Table 2.1. The number of  $e^+$  and  $e^-$  observed were about the same for a given momentum setting, but surprisingly were produced at nearly the same rate whether or not the target was in the beam.

The explanation for this strange result is that most high energy photons were being produced in the Faraday cup used to stop the beam. These photons then were interacting with the nearby aperture slits of the spectrograph entrance and were being converted into electron-positron pairs. The tantalum slits were about 65% of a radiation length, and acted as a fairly efficient converter of high energy gamma rays.

It was then clear that a different technique was needed to measure and separate the high energy electrons, positrons, and gamma rays.

## Chapter 3

### The Positron Experiment

#### 3.1 The Converter Concept

The previous experiment proved unable to separate electrons and positrons produced directly by the nucleus-nucleus collision and those produced by subsequent pair conversions of photons. To solve this problem, the main change was to use a stopping target. In addition, a converter was placed directly behind the target (Figure 3.1). The converter is a piece of metal whose function is to convert high energy photons to electron-positron pairs. The converter was a known photon energy dependent conversion efficiency[Mo69]. Three different converters were used. A comparison of the positron yield for the same target with two different converters allows the determination of the high energy photon flux as well as the direct positron yield from the target.

The emerging positrons include those directly created by the nucleus-nucleus collision (direct positrons) and those created by a pair conversion of a photon into an electron and a positron within the target or converter (conversion positrons). Because of the small yield of the

Figure  
Large

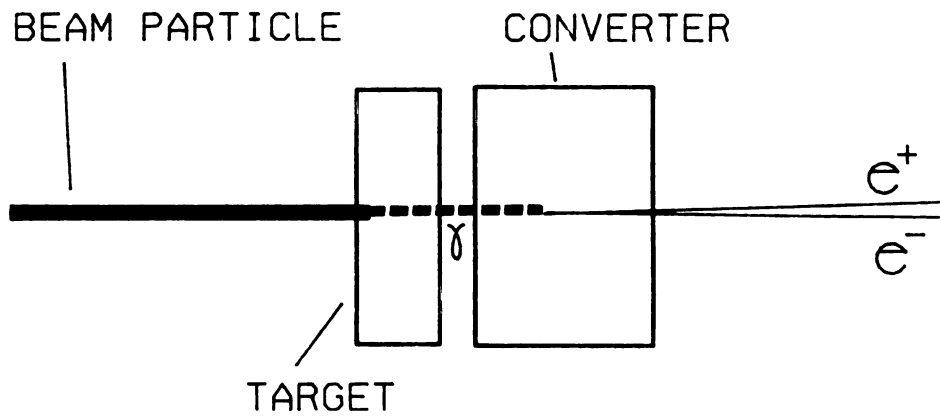


Figure 3.1. Positron experiment concept; stopping target backed by photon converter.

direct positrons, only an upper limit could be obtained from this data.

The target was changed from nickel to copper for convenience. The atomic number  $Z$  and mass  $A$  of copper are close to those of nickel, and subthreshold pion experiments had shown only a slow dependence on target mass [Br84]. The range of the  ${}^{14}\text{N}$  40 MeV/u in copper is  $.77 \text{ g/cm}^2$ , [Li80] so the target was made that thickness.

Three converters, rather than the minimum of two, were selected so that the consistency of the model could be checked. Since the cross section for pair production goes as the square of the atomic number [Ma69], three metals available in pure form were chosen, beryllium, copper, and lead with atomic numbers 4, 26, and 82 respectively.

The three converters were made the same area density so that the contribution from processes which depend on the atomic electrons rather than the nuclei would be approximately the same for all converters. The choice of thickness was a compromise between high conversion efficiency and low multiple scattering and energy loss, so all three were made with area density  $3 \text{ g/cm}^2$ . This made the conversion efficiency of the beryllium comparable to that of the target. The conversion efficiency for 50 MeV gamma rays for the target and converter were 4, 13, and 24% respectively for the beryllium, copper, and lead (as calculated in Chapter 4).

1

0

M

0

0

0

0

0

0

0

0

0

0

0

0

0

0

0

0

0

0

0

0

0

0

0

0

0

The angle between the original photon and the electron or positron is small for the high energy photons [Ma69]. Multiple scattering of the electron and positron within the converter deflects the electrons and positrons from their original direction. Better angular resolution could have been obtained by placing the converter at the entrance of the spectrograph at the expense of efficiency for detecting the electron-positron pairs. Since the previous experiment had not shown a marked angular dependence, it was decided to place the converter in contact with the target. The efficiency would be maximized, since the number of electrons and positrons scattered out of the entrance direction would approximately equal the number scattered in. Angular resolution would be sacrificed, being limited to about the mean scattering angle within the converter. The energy lost by the electron and positron was approximately the same in all the converters.

### **3.2 Modifications to the Spectrograph and Scattering Chamber**

In order to minimize the presence of electron-positron pairs produced by interactions outside the target and converter, as much mass as possible was removed from the entrance of the spectrograph (Appendix B). The 14" scattering chamber was removed and replaced with a 4" chamber with 0.60" thick aluminum walls and an exit hole covered with .003" Kapton to maintain vacuum. The aperture slits were far too thin to limit the acceptance of energetic

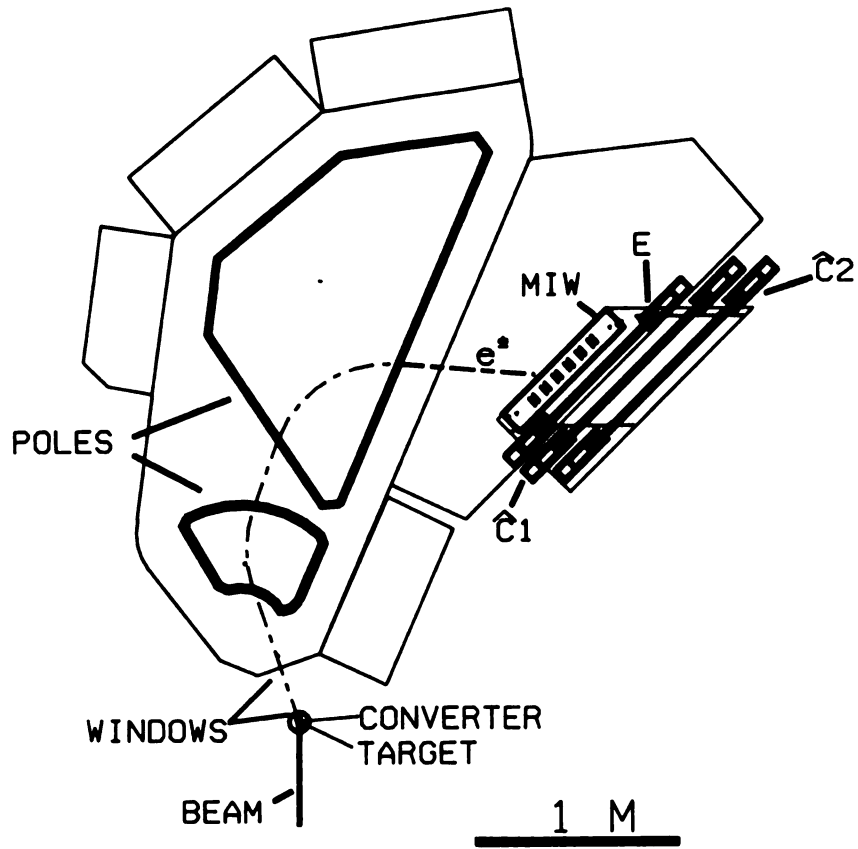


Figure 3.2. Configuration of the  $e^\pm$  experiment.

electrons and positrons; they only served as a source of multiple scattering and conversion. The entire slit mechanism was removed and a large thin window placed across the spectrograph entrance. Electrons and positrons from the target and converter were required to go through the scattering chamber window, air, the entrance window, through the spectrograph, through the exit window, through air to the detector (Figure 3.2). Multiple scattering in the converter was much larger than that due to the windows and air, so the latter was ignored in subsequent calculations. The effective aperture was determined by the steel pole tips of the spectrograph vertically, and by the angular acceptance based on the horizontal angle measured at the detector.

### 3.3 Changes in the Detector

The detector was modified to improve electron identification (Figure 3.3). The MIW counter was unaltered, but the telescope was replaced with a 1" thick plastic E scintillator and two 1" thick Cherenkov counters. These Cherenkov counters were a substantial improvement over the simple plexiglas Cherenkov counter used in the pion experiment (Appendix C). A wavelength shifting plastic developed by Bicron Corp. specifically for Cherenkov counting was used. This plastic absorbs the Cherenkov light and re-emits it isotropically and at a longer wavelength more suited to the photomultiplier tubes [Hu84]. This plastic

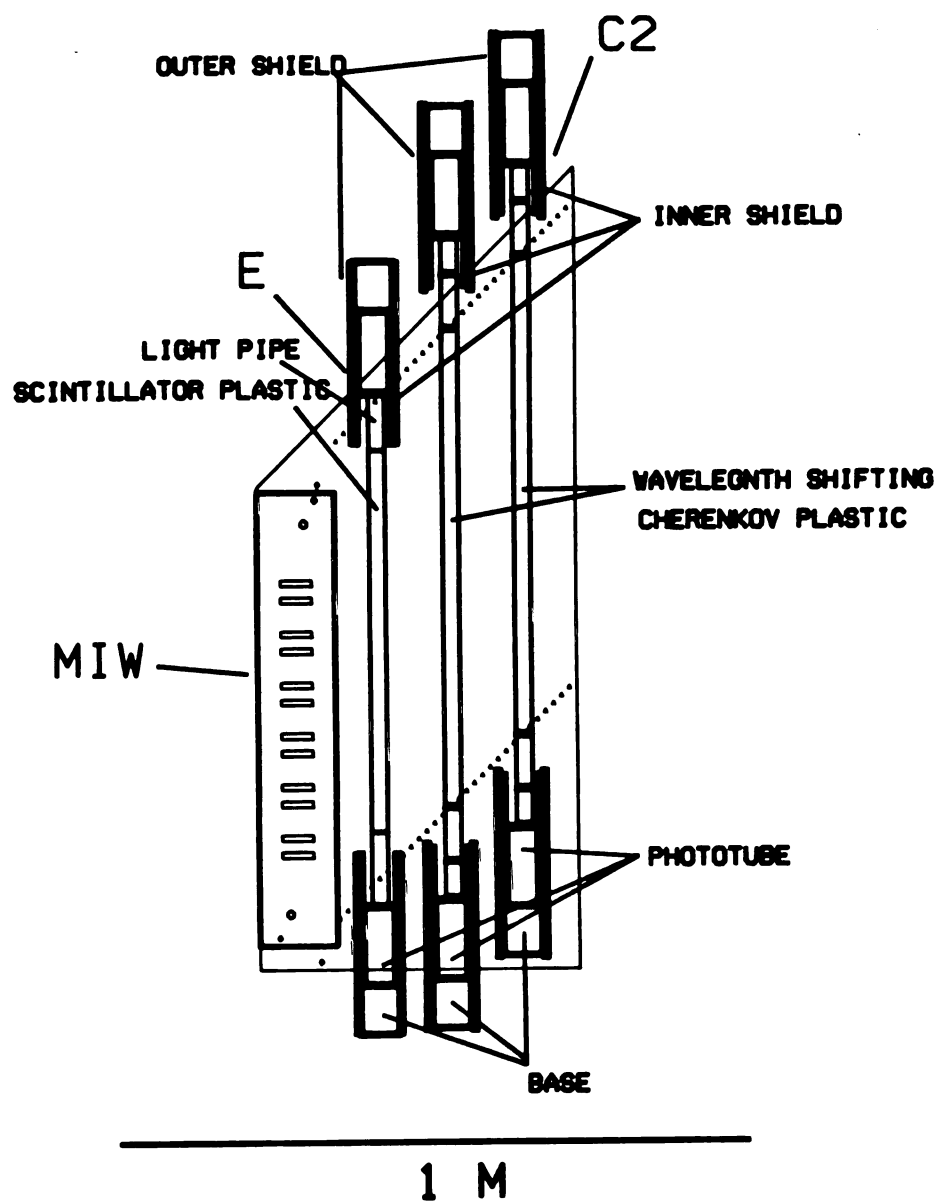


Figure 3.3. Configuration of the  $e^\pm$  detector.

allowed the Cherenkov counters to have a phototube at either end, so that a coincidence between the two ends reduced random noise. In addition, the Cherenkov counters were made much larger than the previous one to allow for the greater multiple scattering of lower energy electrons in the scintillator. The scintillator's increased thickness provided a much stronger signal for the near minimum ionizing electrons or positrons.

The multiple scattering of the positrons or electrons in the plastic increases rapidly with decreasing energy; the size of the Cherenkov counters is a compromise between being able to detect low energy positrons and electrons with good efficiency and keeping the background low. Details of the design of the telescope are in the Appendix. While the plastic scintillator is sensitive to neutrons and gamma rays in the room background, the Cherenkov counter is sensitive only to the gamma rays, which produce relativistic electrons within the counter by Compton scattering, and to cosmic rays, primarily relativistic muons. In addition, the two Cherenkov counters were made identical to simplify design and minimize cost. With the final design, the telescope had nearly unit efficiency for electrons and positrons of energies of greater than 40 MeV.

An event of interest required a signal in both phototubes of the scintillator and first Cherenkov counter. The firing pattern of the MIW, as well as the time and height of each pulse from the scintillator, Cherenkov

counters, and MIW cathode was recorded by the acquisition system. In the process of data analysis the requirement that the MIW pattern correspond to a particle within the correct solid angle, and that the scintillator and both Cherenkov counters produce proper pulses, eliminated the events due to cosmic rays and room background.

### 3.4 Verification Tests

The interpretation of these data depended strongly on the calculations of the efficiency of the converter and detector. Since high energy electrons can be created not only by pair production, but also by Compton scattering of high energy photons, most of the data was taken with positrons. During the course of the experiment, several tests were carried out to check that the high energy positrons being observed were of an energy consistent with the energy deduced from the spectrograph magnetic field setting. These tests were based on the range and multiple scattering of the positrons, and consisted of placing absorber between the Cherenkov counters. The calculations and results of the tests are described in detail in the next chapter.

### 3.5 Results

The highest energy  $^{14}\text{N}$  beam available, 40 MeV/u, was used since it was assumed that the yield of these high energy photons, electrons, and positrons would increase with

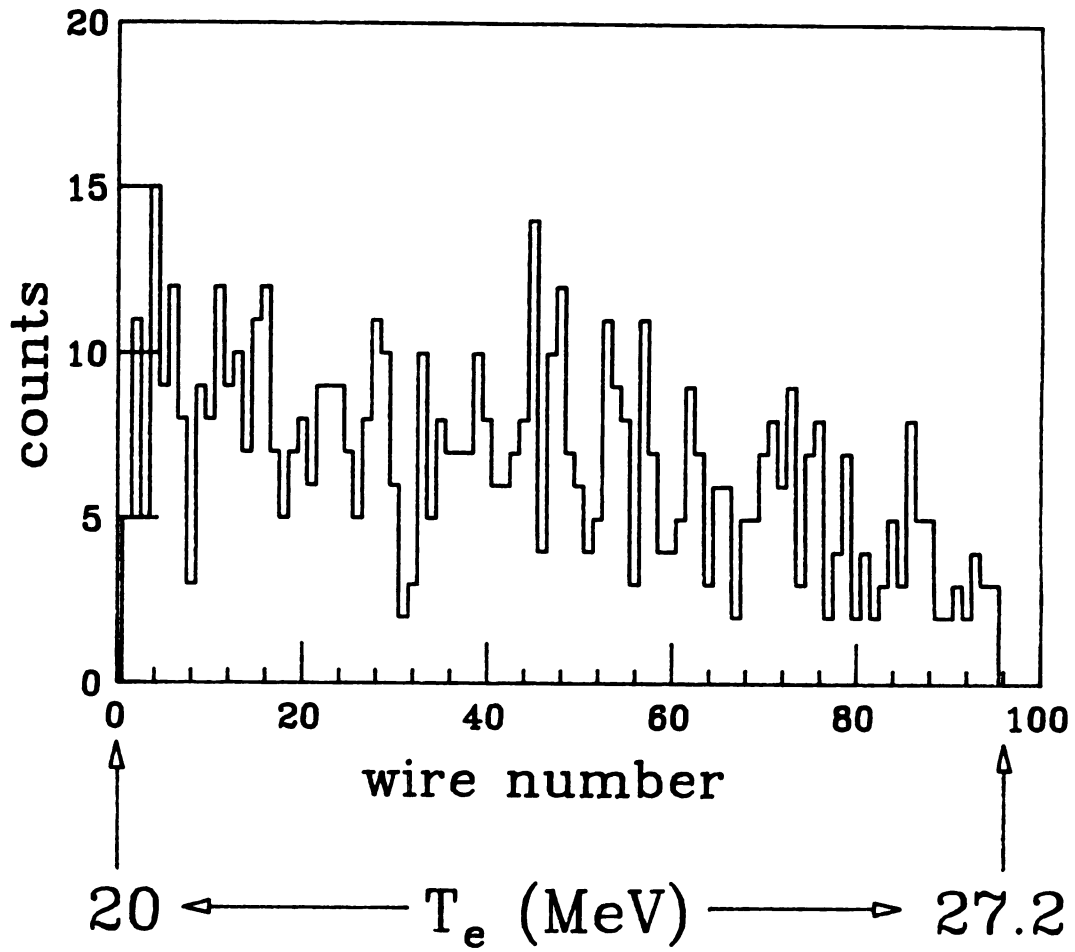


Figure 3.4 Typical  $e^+$  position spectrum.

energy. The target was copper, and the laboratory angles measured  $0^\circ$ ,  $17^\circ$ , and  $40^\circ$ . Greater angles could not be reached with this system, since target and converter needed to stay fixed normal to the spectrograph entrance, and the beam spot size increased as the angle was increased. The details of the data acquisition are in Appendix B and D. A typical ungated positron position spectrum in the MIW counter is shown in Figure 3.4. Figure 3.5 is a plot of Cherenkov#1 pulse height vs. the E scintillator pulse height signal. The same plot is shown in Figure 3.6 but has in addition the requirement of a good angle from the MIW counter. Finally, Figure 3.7 has the additional requirement of a valid signal from Cherenkov#2. With these requirements, the counts remaining in Figure 3.7 represent positrons which are within the aperture of the spectrograph and penetrate the scintillator and both Cherenkov counters. Figure 3.8 is a plot of the electron yield vs. the electron energy at  $17^\circ$  for the three converters. Figures 3.9, 3.10, and 3.11 are plots of the positron yield at  $17^\circ$ ,  $0^\circ$ , and  $40^\circ$  respectively for the three converters.

Multiple scattering in the converter smooths the angular distribution; 20 MeV positrons have a mean scattering angle of  $27^\circ$  in the Pb converter, whereas 70 MeV positrons have a mean scattering angle of  $8^\circ$ . Thus, the angular distribution of the high energy positrons reflects the angular distribution of the gamma rays (shown in Figure 3.12).

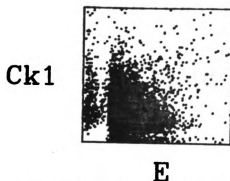


Figure 3.5. Pulse height in Cherenkov counter #1 vs. pulse height in the E scintillator.

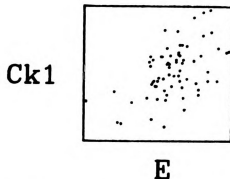


Figure 3.6. The same as in Figure 3.5. but with the requirement of a good angle in the MIW counter.

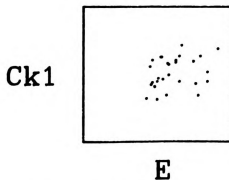


Figure 3.7 The same as in Figure 3.6. but with the additional requirement that Cherenkov#2 produced a pulse.

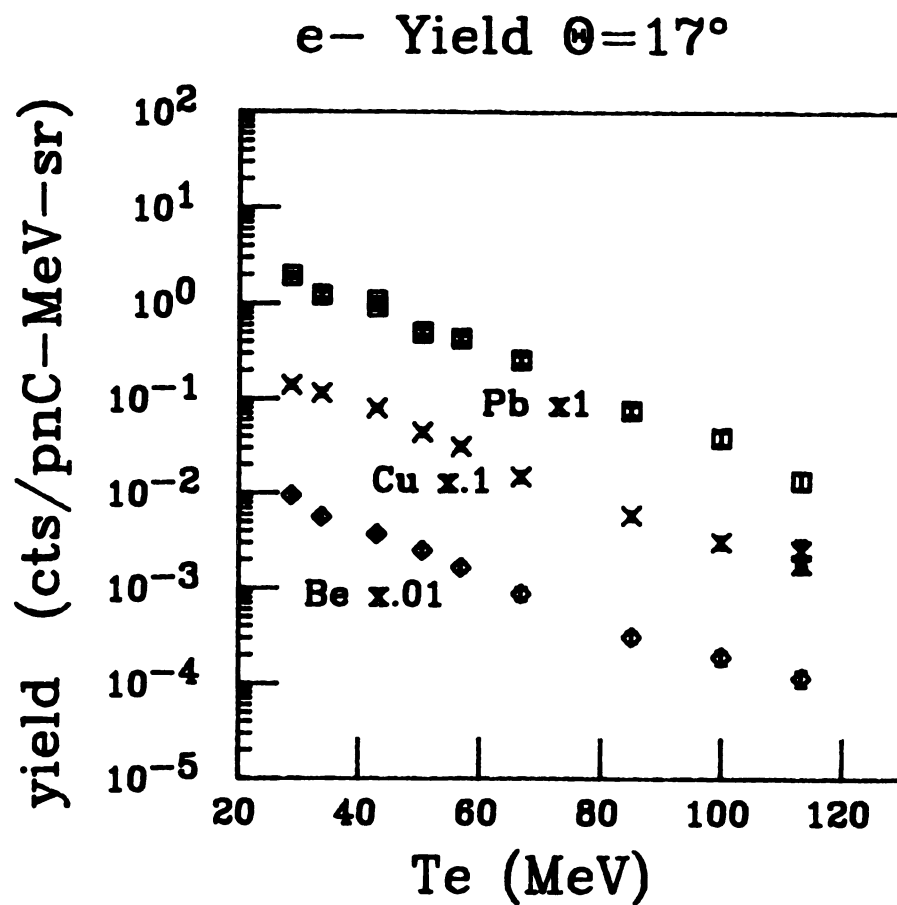


Figure 3.8. Electron yield as a function of electron energy for the three converters at  $17^\circ$ .

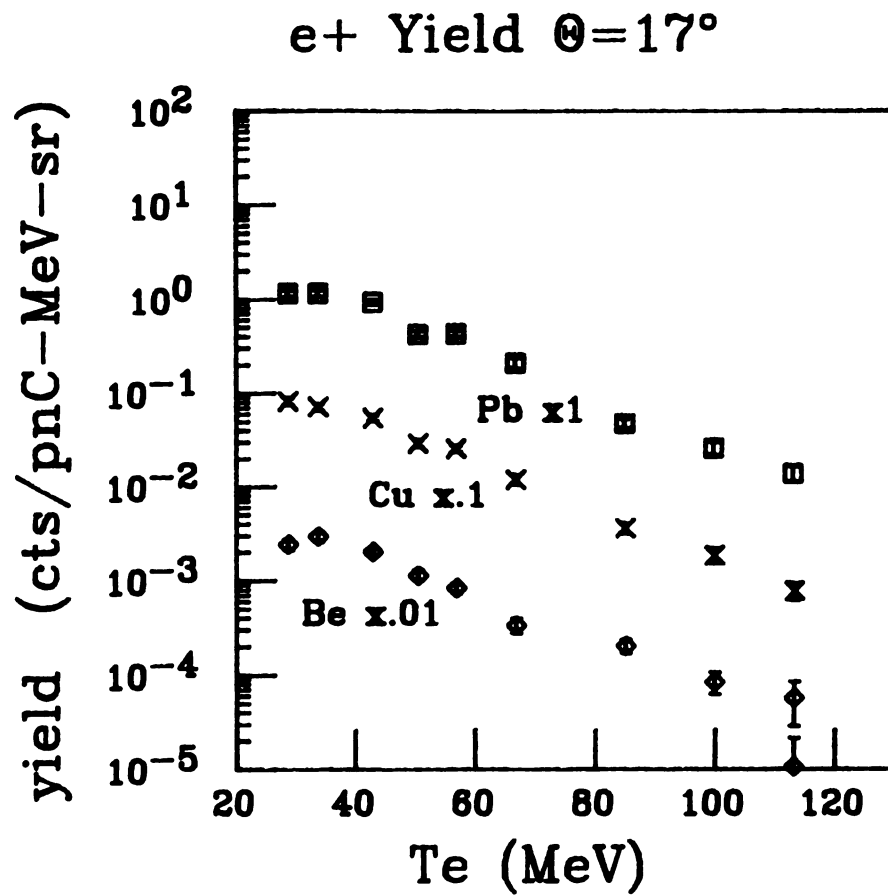


Figure 3.9. Positron yield as a function of positron energy for the three converters at  $17^\circ$ .

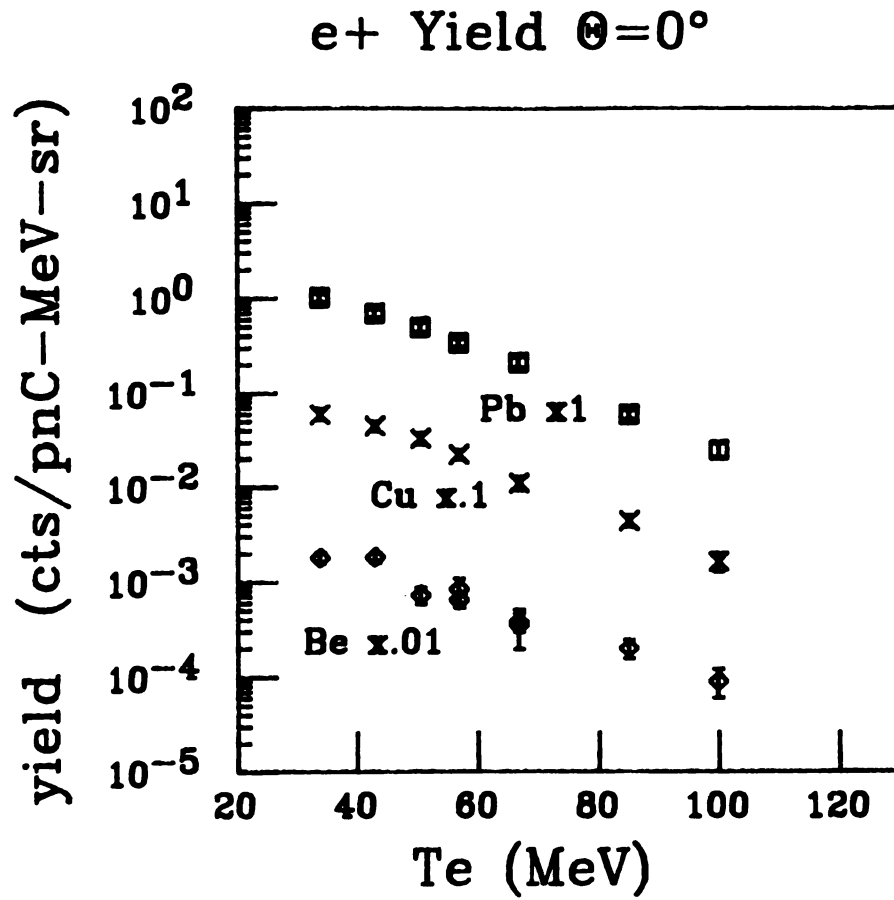


Figure 3.10. Positron yield as a function of positron energy for the three converters at  $0^\circ$ .

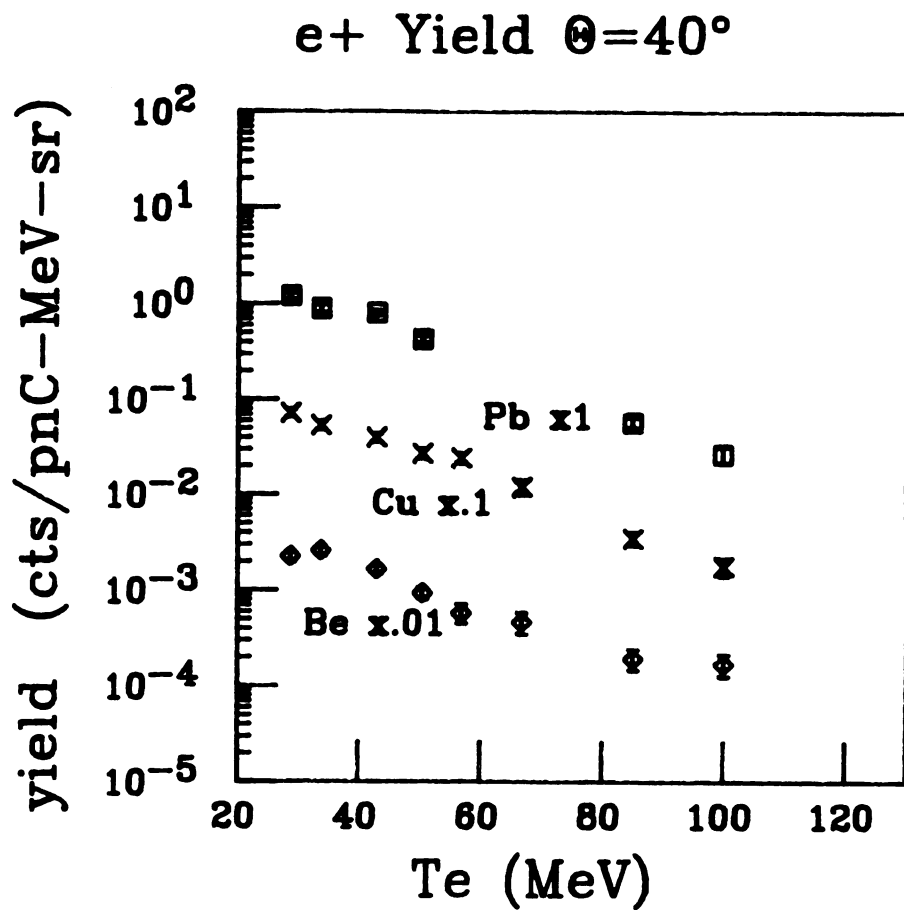


Figure 3.11. Positron yield as a function of positron energy for the three converters at  $40^\circ$ .

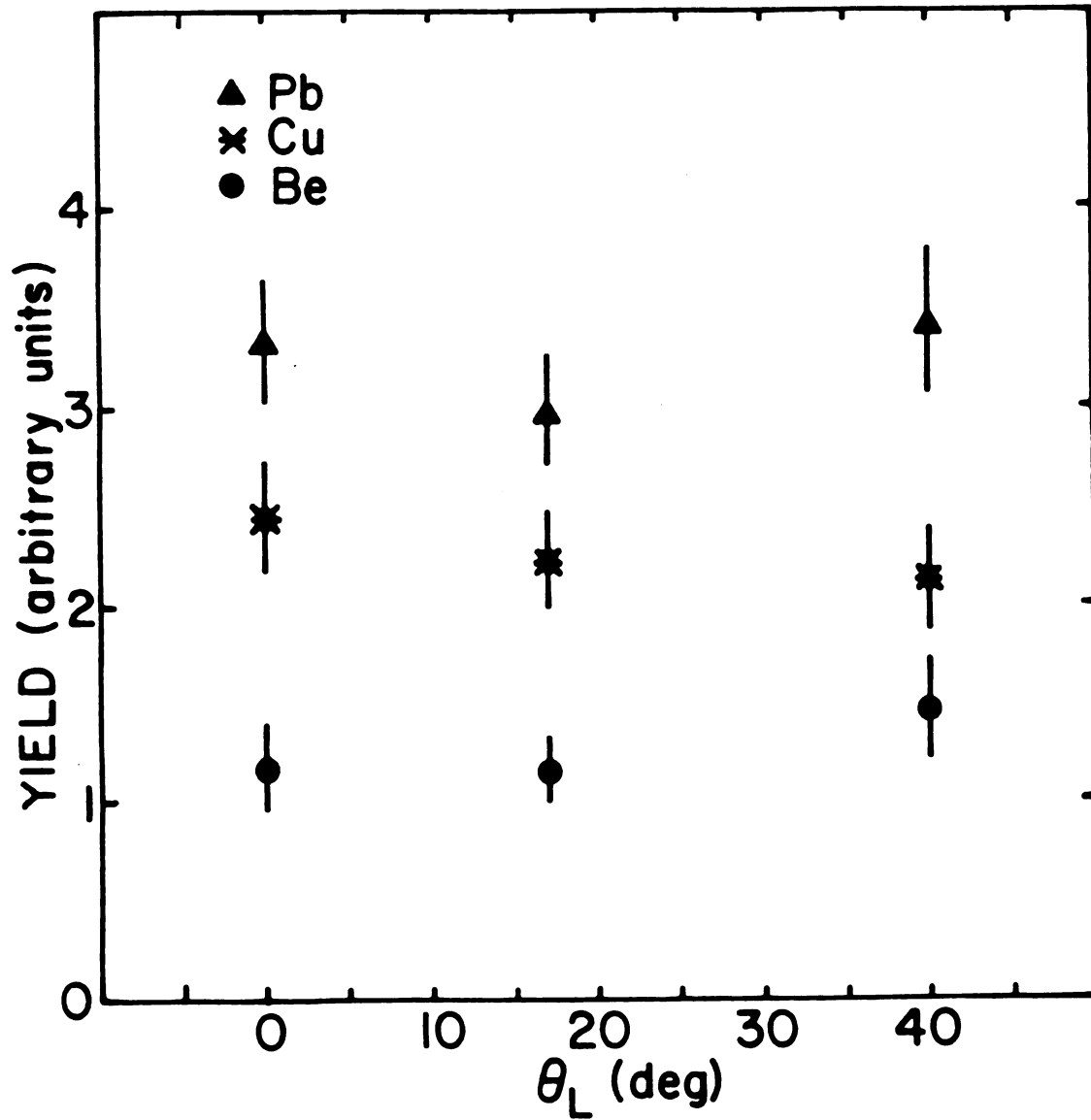


Figure 3.12. Angular dependence of the high energy positron (70 - 105 MeV) yield for the three converters.

The Monte-Carlo simulation of the detector used in the analysis of the data reflected that a positron scattered in the first Cherenkov counter sometimes misses the second counter. This is discussed in the next chapter.

## Chapter 4

Analysis of the  $e^{\pm}$  Experiment

## 4.1 Introduction and an Example of a Monte Carlo Calculation

The results of this experiment depend strongly on efficiency of the converter and detector. Two separate calculations were done; one to simulate the conversion of the photons into positrons, the other to simulate the response of the detector to those positrons. Both used Monte-Carlo techniques and were run on the NSCL VAX-780 computer.

As an overview of the technique, consider the two-dimensional example of a particle passing through  $N$  identical thin slabs (Figure 4.1). In each slab of thickness  $t$ , the particle loses no energy, but scatters into a new direction  $\Delta\theta$  from the entrance angle with a mean angle of  $\phi_0$ . To find the exit angle distribution for the entire stack, one could find the distribution for exiting the first slab, solve for the distribution after the second slab as a function of its entrance angle, combine these to get the net

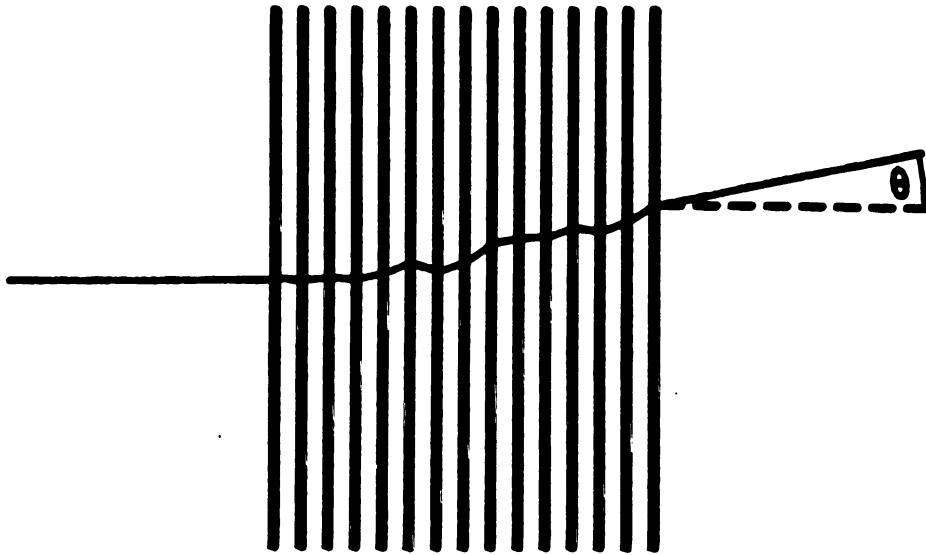


Figure 4.1. A particle scattering through  $N$  thin identical slabs.

distribution after the second slab, and repeat this for all the slabs. If the scattering angle is small:

$$\theta \ll 1 \quad \frac{t}{\cos \theta} \approx t$$

the slab 1 distribution is

$$P(\Delta\theta_1) = \frac{1}{\phi_0 \sqrt{\pi}} e^{-\Delta\theta_1^2 / \phi_0^2}$$

and for N identical slabs

$$P(\theta) = \int P(\Delta\theta_1) \dots P(\Delta\theta_N) \delta(\theta - \Sigma \Delta\theta_i) d\Delta\theta_1 \dots d\Delta\theta_N$$

$$P(\theta) = \frac{1}{\phi_0 \sqrt{\pi}^N} \int e^{-\Sigma (\Delta\theta_i)^2 / \phi_0^2} \delta(\theta - \Sigma \Delta\theta_i) d\Delta\theta_1 \dots d\Delta\theta_N$$

Using  $\delta(x) = \frac{1}{2\pi} \int e^{-ikx} dk$  [Re65]

$$P(\theta) = \frac{1}{2\pi \phi_0 \sqrt{\pi}^N} \int e^{-ik\theta} \left[ \int e^{-[(\Delta\theta_i)^2 / \phi_0^2 + ik\Delta\theta_i]} d\Delta\theta_i \right]^N dk$$

completing the square in the exponential and integrating,

$$P(\theta) = \frac{1}{2\pi \phi_0 \sqrt{\pi}^N} \int e^{-ik\theta} \left[ \phi_0 \sqrt{\pi} e^{-k^2 \phi_0^2 / 4} \right]^N dk$$

$$P(\theta) = \frac{1}{2\pi} \int e^{-\left[\frac{Nk^2 \phi_0^2}{4} - ik\theta\right]} dk = \frac{1}{2\pi} e^{-\frac{\theta^2}{N\phi_0^2}} \int e^{-N\left[\frac{k\phi_0}{2} - \frac{i\theta}{\phi_0 \sqrt{N}}\right]^2} dk$$

$$P(\theta) = \frac{1}{2\pi} \frac{2\sqrt{\pi}}{\phi_0 \sqrt{N}} e^{-\left[\frac{\theta^2}{N\phi_0^2}\right]} = \frac{1}{\phi_0 \sqrt{N} \sqrt{\pi}} e^{-\left[\frac{\theta^2}{N\phi_0^2}\right]} = \frac{1}{\phi \sqrt{\pi}} e^{-\theta^2 / \phi^2}$$

where  $\phi = \sqrt{N} \phi_0$ .

The exact integral could be attacked numerically, but an alternative is available.

The alternative is to start with one particle and follow it through the system, providing the scattering angle (and corresponding energy loss) from a random number generator whose output provides the correct probability distribution of scattering angle. The process is repeated for many particles so that an exit angle distribution is made.

In this example, a random number generator with the appropriate distribution must first be made. Starting with the probability distribution  $P(\Delta\theta)$  (Figure 4.2):

$$P(\Delta\theta_i) = \frac{1}{\sqrt{\pi}} e^{-\Delta\theta_i^2 \cos^2(\sum_{j<i} \Delta\theta_j) / \phi_0^2}$$

a new function  $F$  must be defined such that

$$F(\Delta\theta) = \frac{\int_{-\infty}^{\Delta\theta} P(\alpha) d\alpha}{\int_{-\infty}^{+\infty} P(\alpha) d\alpha}$$

and the inverse function  $F^{-1}(x)$  must be found for  $0 \leq x \leq 1$ .

Here (Figure 4.3)

$$F(\Delta\theta) = \frac{1}{\sqrt{\pi}} \frac{\cos(\sum_{j<i} \Delta\theta_j)}{\phi_0} \int_{-\infty}^{\Delta\theta} e^{-[\cos^2(\sum_{j<i} \Delta\theta_j) / \phi_0^2] \alpha^2} d\alpha$$

$$\text{recall } \text{erf}(u) = \frac{2}{\sqrt{\pi}} \int_0^u e^{-t^2} dt$$

Figure 4.2.

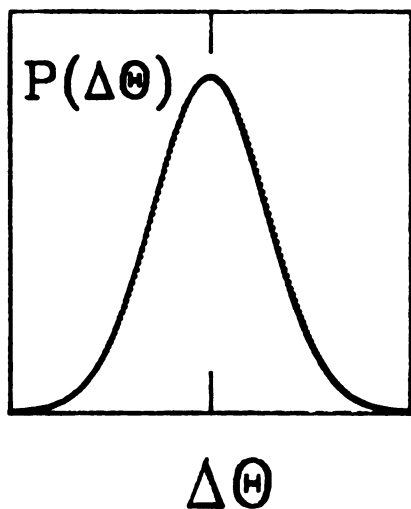


Figure 4.

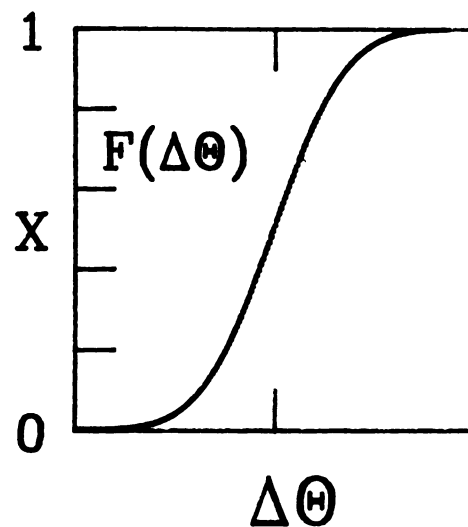
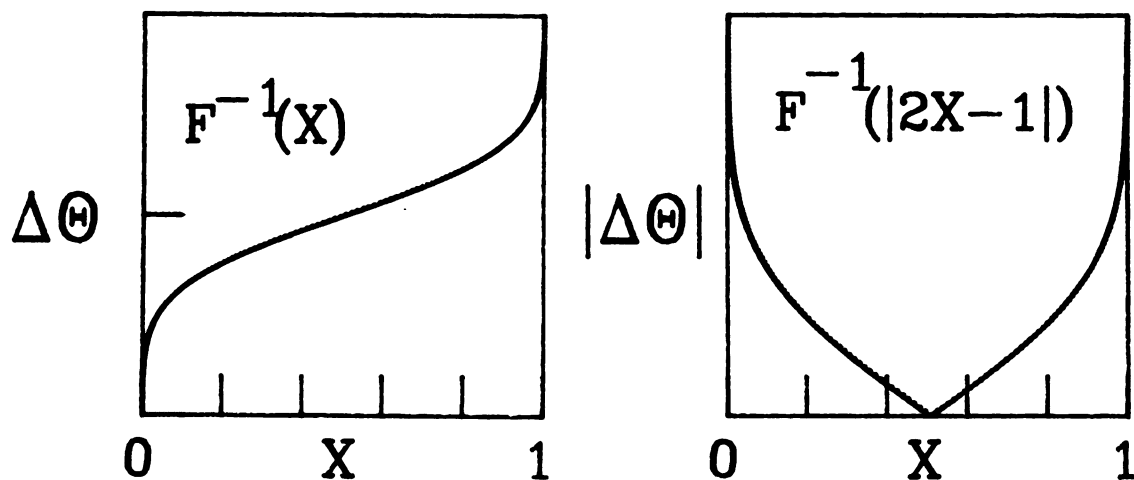
Figure 4.2. Example probability distribution  $P(\theta)$ .Figure 4.3. Integrated probability distribution  $F(\theta)$ .Figure 4.4. Inverse of the integrated probability distribution  $F^{-1}(X)$ .

Table 4.1. Steps for the example Monte Carlo simulation.

- 1 set  $\theta = 0$
- 2 choose  $0 \leq x \leq 1$  using a random number generator
- 3 choose  $0 \leq y \leq 1$  using a random number generator
- 4 get  $|\Delta\theta|$  from  $x$  using  $F^{-1}(x)$  for the current value of  $\theta$
- 5 if  $y \leq 1/2$ , set  $\theta = \theta - \Delta\theta_j$ , otherwise  $\theta = \theta + \Delta\theta_j$
- 6 repeat steps 2-5 for each of the  $N$  elements
- 7 record  $\theta_N$  and repeat entire sequence 1-6 many times

$$\text{hence } F(\Delta\theta) = \begin{cases} 1/2 + \text{erf}(+\Delta\theta)/2 & \Delta\theta > 0 \\ 1/2 - \text{erf}(-\Delta\theta)/2 & \Delta\theta < 0 \end{cases}$$

$$\text{so (Figure 4.4) } F^{-1}(x) = \frac{\pm\phi_0}{\left| \cos\left(\frac{\phi_0}{\sum_1 \Delta\theta_j}\right) \right|} \text{erf}^{-1}(|2x-1|)$$

This is a random number generator producing  $\Delta\theta$  with the distribution given by  $P(\Delta\theta)$ . The inverse of the error function ( $\text{erf}^{-1}$ ) is a FORTRAN library function available on the VAX-780 computer. Following the particle through the  $N$  elements is straight forward (Table 4.1).

The results are placed in bins, and form the exit angle distribution.

## 4.2 Modelling the Detector Efficiency

The  $e^\pm$  experiment measured the positrons at  $0^\circ$ ,  $17^\circ$ , and  $40^\circ$  and the electrons at  $17^\circ$ ; the efficiency of the detector at counting the positrons and electrons needed to be calculated. The detector consisted of four active elements of differing size and material, rigidly mounted on an aluminum plate fixed to the focal plane of the spectrograph, parallel to the focal plane but spaced apart along the central particle trajectory  $45^\circ$  to the focal plane. The program DESCRIMIW was used to generate a file describing the size, shape, and location of each element of the detector. The position of the elements could be changed

with respect to the MIW proportion chamber, which had a fixed relationship to the focal plane track.

A Monte-Carlo calculation, SCATTER, in principle very similar to the example, was used to determine the detector's efficiency. A positron begins at the focal plane, passes through the MIW chamber, enters the E scintillator, and then begins to lose energy and scatter in both the vertical and horizontal plane. The mass of the air and the MIW chamber is very low compared to the plastic elements and is ignored. The positron travels through the element in a series of short steps; after each the energy loss is deducted and the new direction determined (subroutines NEWCOORD and NEWDIRECT). This continues until the positron leaves the element or stops (as determined in function INSIDE). If the positron has not stopped, the particle then travels without interacting with the air to the next element (subroutine NEXT), and the process repeats. After each element, subroutines STATZ and FILEZ record the information. After the last element, the record is filed, another positron is generated, and the entire process repeats.

The initial distribution of positrons reaching the detector is taken to be spatially uniform, with the energy of the positron depending on its position. The relationships for position and energy in the spectrograph are given in Appendix B. The horizontal angle, vertical angle about the central ray, and the vertical position are also uniformly distributed over their range. The limits are

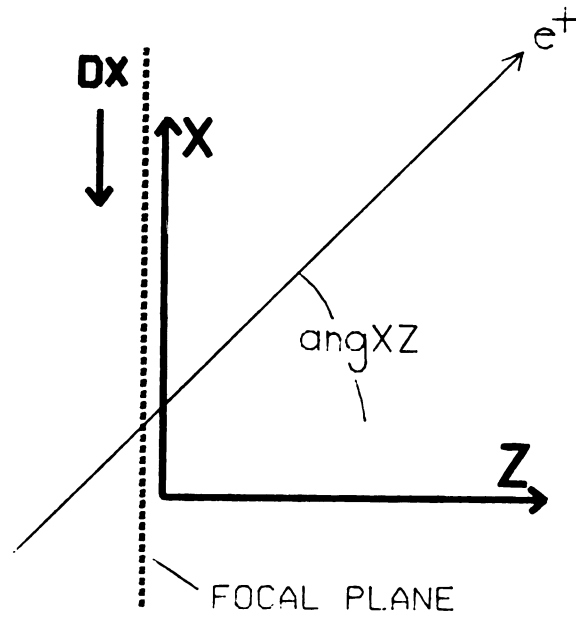


Figure 4.5. Co-ordinate system used in the Monte Carlo calculation.

Table 4.2. Initial limits of the  $e^+$  and  $e^-$  distribution for the code SCATTER.

<u>variable</u>	<u>minimum</u>	<u>maximum</u>
focal plane position DX	$\overline{41.025}$	$\overline{20.025}$ inches
horizontal position X	-2.54	+50.8 cm
vertical position Y	-1.0	+1.0 cm
horizontal angle angXZ	36°	54°
vertical angle angY	-1.2°	+1.2°

listed in Table 4.2 and the co-ordinate system is shown in Figure 4.5.

The energy loss of the positrons in all materials was taken to be the minimum ionizing value of  $1.9 \text{ MeV}/(\text{g}/\text{cm}^2)$ . For  $100 \text{ MeV } e^+$  in plastic, this is half the correct energy loss, but the mean scattering angle is decreased by only about 10%. Bremsstrahlung in the converters is difficult to model and was ignored.

Scattering within the detector was based on the scattering formula[Ag82]:

$$\theta_0 = \frac{14.1 \text{ MeV}/c}{p \beta} Z_{inc} \sqrt{L/L_R} \left[ 1 + \frac{1}{9} \log_{10}\{L/L_R\} \right] \text{ (radians)}$$

where  $p$  is the particle momentum in  $\text{MeV}/c$   
 $\beta$  is the particle velocity divided by  $c$   
 $Z_{inc}$  is the particle charge in elemental charges  
 $L/L_R$  is the thickness in radiation lengths of the scattering medium

$$\text{and } \theta_0 = \theta_{\text{plane}}^{\text{rms}} = \frac{1}{\sqrt{2}} \theta_{\text{space}}^{\text{rms}}$$

The function which determines if the positron is inside or outside of a given element is named INSIDE. By running the program DESCRIMIW and answering the questions, a file is generated describing the shape, size, material, and position of each element. These points are stored in the array "extent(MIW\_el,i,j)", where MIW\_el is the number of the

element,  $i$  is the number of the point, and  $j$  is 1, 2, or 3 for the  $x$ ,  $y$ , or  $z$  coordinate.

First, the function INSIDE finds out if the positron is within the  $z$  axis extent of the element. If it is, the direction from the center of the element to the positron is found, and the two points describing the edge of the element on either side of the line connecting the center and the positron are found. They are used to produce a line connecting them, and the intersection of the line defining the edge and the line connecting the positron and the center is found. If this intersection is farther from the center than the positron, the positron is within the element and `INSIDE = .TRUE.`, otherwise `INSIDE = .FALSE.`

The code SCATTER was run using the configuration of the run (Figure 3.3). All positrons are presumed to penetrate the MIW chamber, and scattering takes place in the scintillator (E), the first Cherenkov counter ( $\hat{C}_1$ ), and the second Cherenkov counter ( $\hat{C}_2$ ). The tables generated show the number of positrons which started in one of six bins, and the number depositing at least 1 MeV in each element. The settings of the spectrograph magnet used in the calculation were those used in the experiment. Figure 4.6 shows the probability of an electron depositing at least 1 MeV in the E and  $\hat{C}_1$  elements and of depositing at least 1

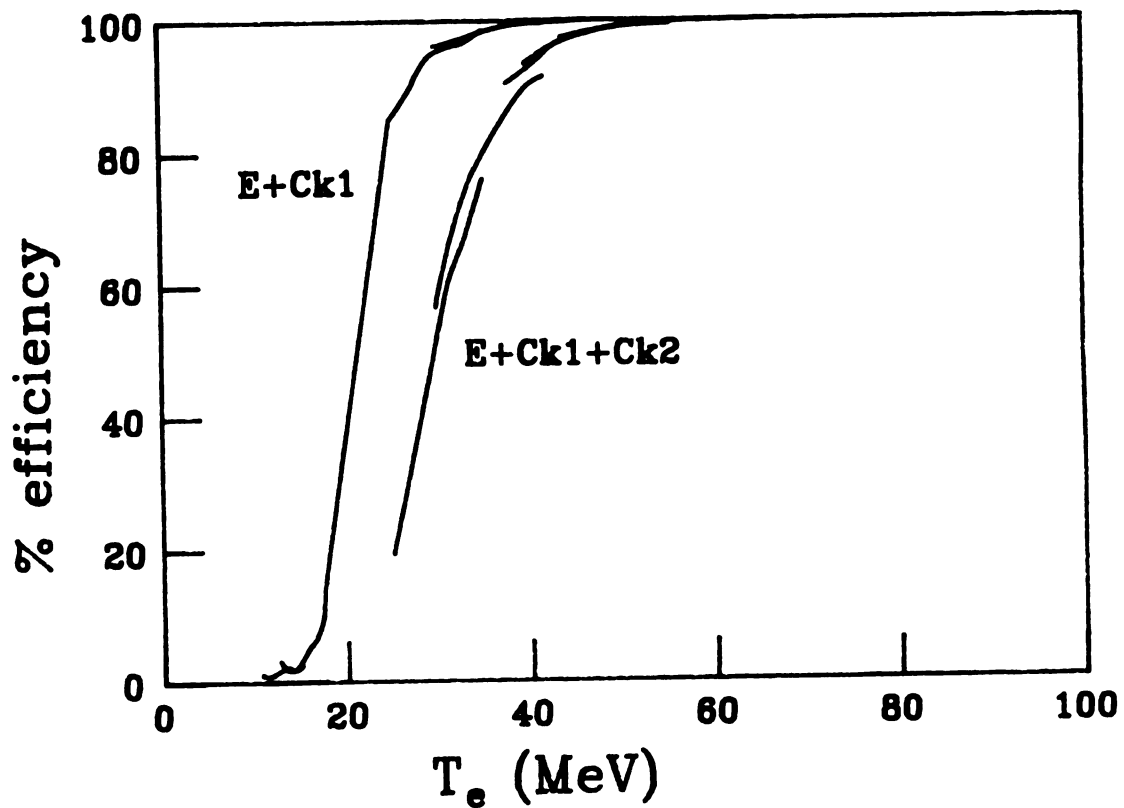


Figure 4.6. Calculated efficiency of the detector for electrons penetrating the scintillator and the first Cherenkov counter, and for electrons then penetrating the second Cherenkov counter.

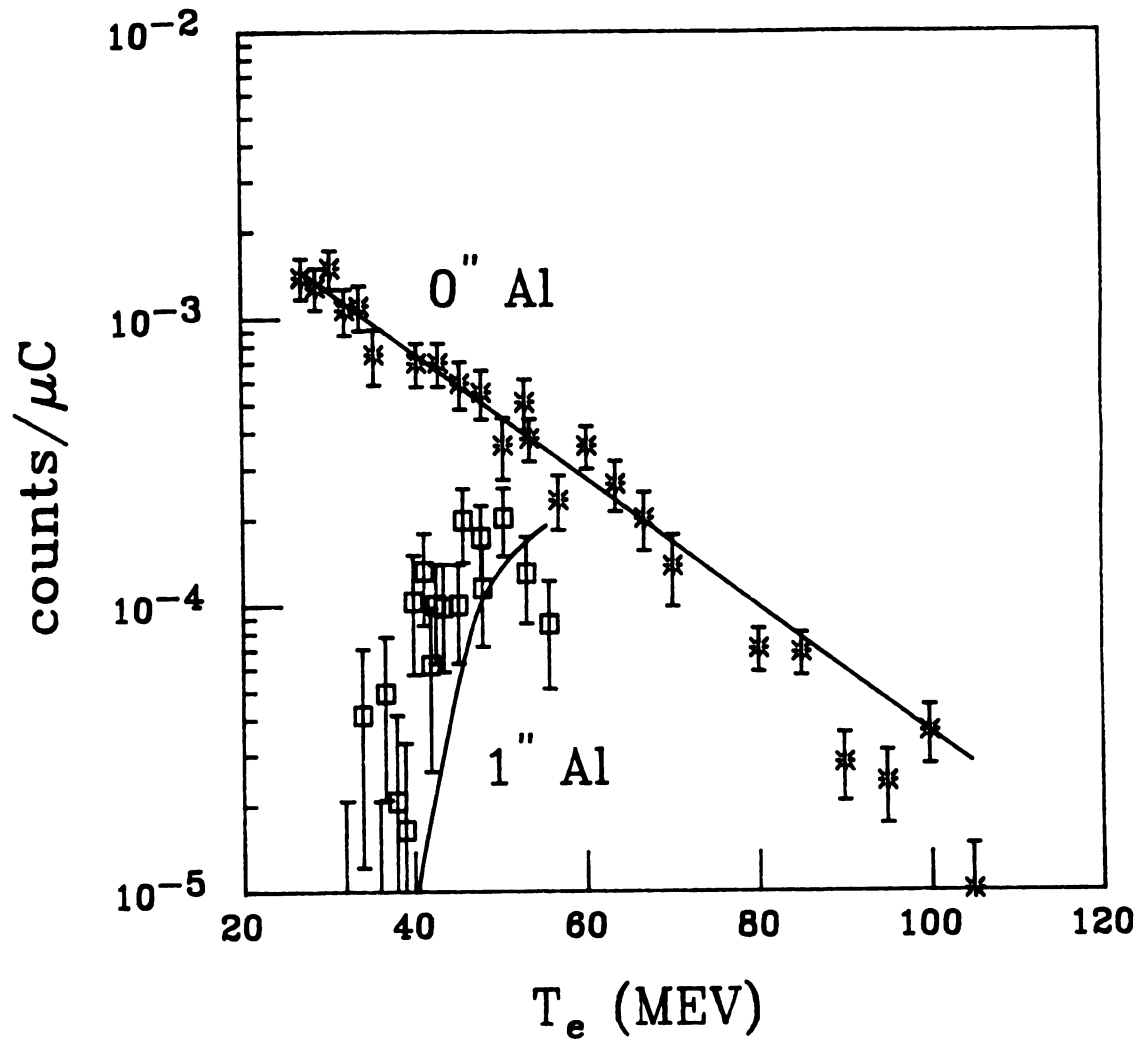


Figure 4.7. The calculated and measured effect of inserting a 1" aluminum plate between the Cherenkov counters.

Ma

en

th

o

r

e

m

e

t

l

c

MeV in the  $E$ ,  $\hat{C}_1$ , and  $\hat{C}_2$  elements as a function of electron energy. The breaks in the line are due to edge effects in the detector; the detector is more efficient for an electron of given energy at the low radius end than at the high radius end. An important feature to note is that the efficiency reaches about 100% by a positron energy of 25 MeV.

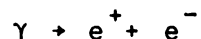
The program EFFTAB produces a smooth description of efficiency as a function of positron energy from the tabulated results.

#### 4.2.1 Verification Tests

To check experimentally the validity of this calculation, extra elements were inserted into the detector during the experiment. First a 1 inch, then a 2 inch thick aluminum plate was placed between the first and second Cherenkov detectors and the measurement repeated. Figure 4.7 shows the measurement with no aluminum plate and a 1" aluminum plate. Superimposed are solid lines representing the calculations, and the dashed line is the fit to the original positron spectra without the aluminum plate.

#### 4.3 The Pair Production Cross Section

The technique used to detect high energy photons in this experiment is based on the reaction:



which occurs in the strong electric field of a nucleus or electron. The difference in the momentum and energy of the pair and the photon is transferred as recoil to the nucleus or electron. If the particle is heavy, like a nucleus, virtually all the energy of the photon appears in the electron-positron pair, and the process is called pair production. If the particle is an electron, the momentum and energy is distributed over a positron and two indistinguishable electrons, and is called trident production. For high energy gamma rays, pair production is the dominant mode of conversion.

While measurement of both members of the pair gives the photon's energy, measurement of one member provides only a lower limit on the photon's energy. This experiment was limited to detection of only one half of the pair at a time, requiring a calculation based on the measurement of many positrons to determine the original photon distribution.

The differential cross section for a photon producing a positron of energy  $E_+$  is known and can be used to determine the approximate original photon spectrum given the cross section for positron production. Information about details in the photon spectrum is lost, but the magnitude and trend of the spectrum can be determined using a Monte-Carlo simulation of the experiment.

Due to the high momentum of the photon, the electron-positron pair created through interaction with the nucleus has a large momentum in the direction of the photon. The

angle between the original photon and the positron is about  $m_e c^2/E_\gamma$  radians [Ma69], but the kinetic energy of the positron may have any value between 0 and  $(E_\gamma - 2 m_e c^2)$ . The differential cross section for a given photon energy has been calculated, and a simple form good to about 10% is formula 3D-1003 of reference [Mo69], used in the earlier work of Budiansky [Bu81].

The formula for differential cross section for pair conversion is found by taking:

if  $\gamma < 2$  then

$$\frac{d\sigma}{dE_+} = \frac{\alpha Z^2 r_0^2}{k^3} \left\{ (E_+^2 + E_-^2) \left[ \phi_1(\gamma) - \frac{4}{3} \ln Z \right] + \frac{2}{3} E_+ E_- \left[ \phi_2(\gamma) - \frac{4}{3} \ln Z \right] \right\}$$

and if  $2 \leq \gamma \leq 15$

$$\frac{d\sigma}{dE_+} = \frac{4\alpha Z^2 r_0^2}{k^3} (E_+^2 + E_-^2 + \frac{2}{3} E_+ E_-) \left[ \ln\left(\frac{2E_+ E_-}{k}\right) - \frac{1}{2} - C(\gamma) \right]$$

where  $k = E_\gamma / m_e c^2$

$$E_+ = (T(e^+) + m_e c^2) / m_e c^2$$

$$E_- = (T(e^-) + m_e c^2) / m_e c^2$$

$$\gamma = 100 k / (E_+ E_- Z^{1/3})$$

$$G = 1.36 \gamma$$

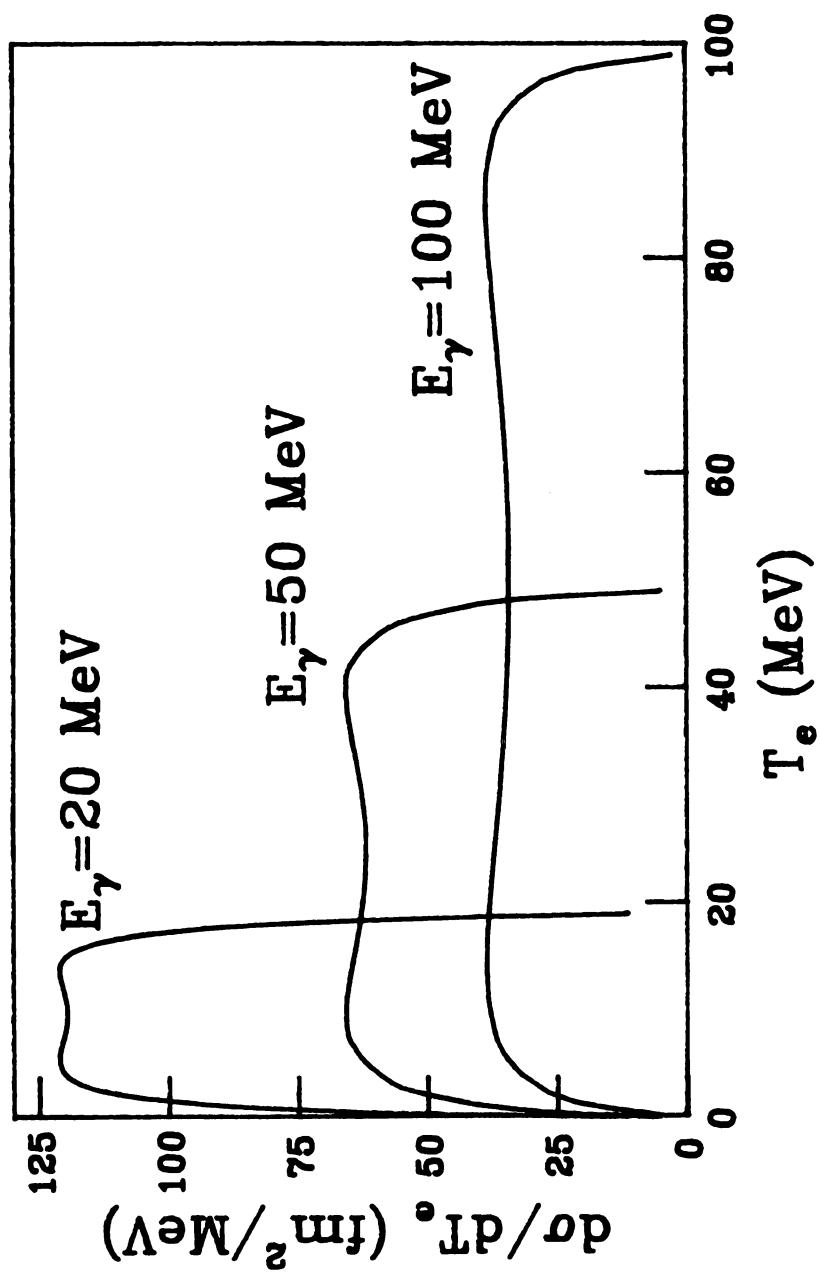


Figure 4.8. Differential pair production cross section in Pb for 20, 50, and 100 MeV photons.

The  $T(e^\pm)$  denotes the kinetic energy of the  $e^\pm$ . For all practical purposes  $k = E_+ + E_-$ .

Fitting a curve in reference[Mo69]:

$$C(\gamma) = .5249857 e^{-0.4980655 \gamma} + 0.01528705$$

if  $G \leq 1$ , then

$$\phi_1(\gamma) = 20.868 - 3.242 G + 0.625 G^2$$

$$\phi_2(\gamma) = 20.209 - 1.930 G + 0.086 G^2$$

if  $G > 1$  then

$$\phi_1(\gamma) = \phi_2(\gamma) = 21.12 - 4.186 \ln(G + 0.952)$$

The FORTRAN function SIG(x) calculates the differential cross section in units of  $\text{fm}^2/\text{MeV}$  for  $x = E_+/(E_\gamma - 2m_e c^2)$ . A plot of the differential cross section for Pb and  $E_\gamma = 20, 50, \text{ and } 100 \text{ MeV}$  is shown in Figure 4.8.

The region  $\gamma > 15$  represents positrons with momentum either close to zero or near the momentum of the original photon. In particular, if  $\gamma > 15, Z=4, k=100$  ( $\sim 50 \text{ MeV } \gamma$ ) the positron has either less than 4% or more than 96% of the photon's energy. For the purposes of the calculation, the above form was also assumed to be valid for  $\gamma > 15$ . The error introduced is less than the fraction of the positrons whose energy range is outside the region  $\gamma > 15$  for all photon

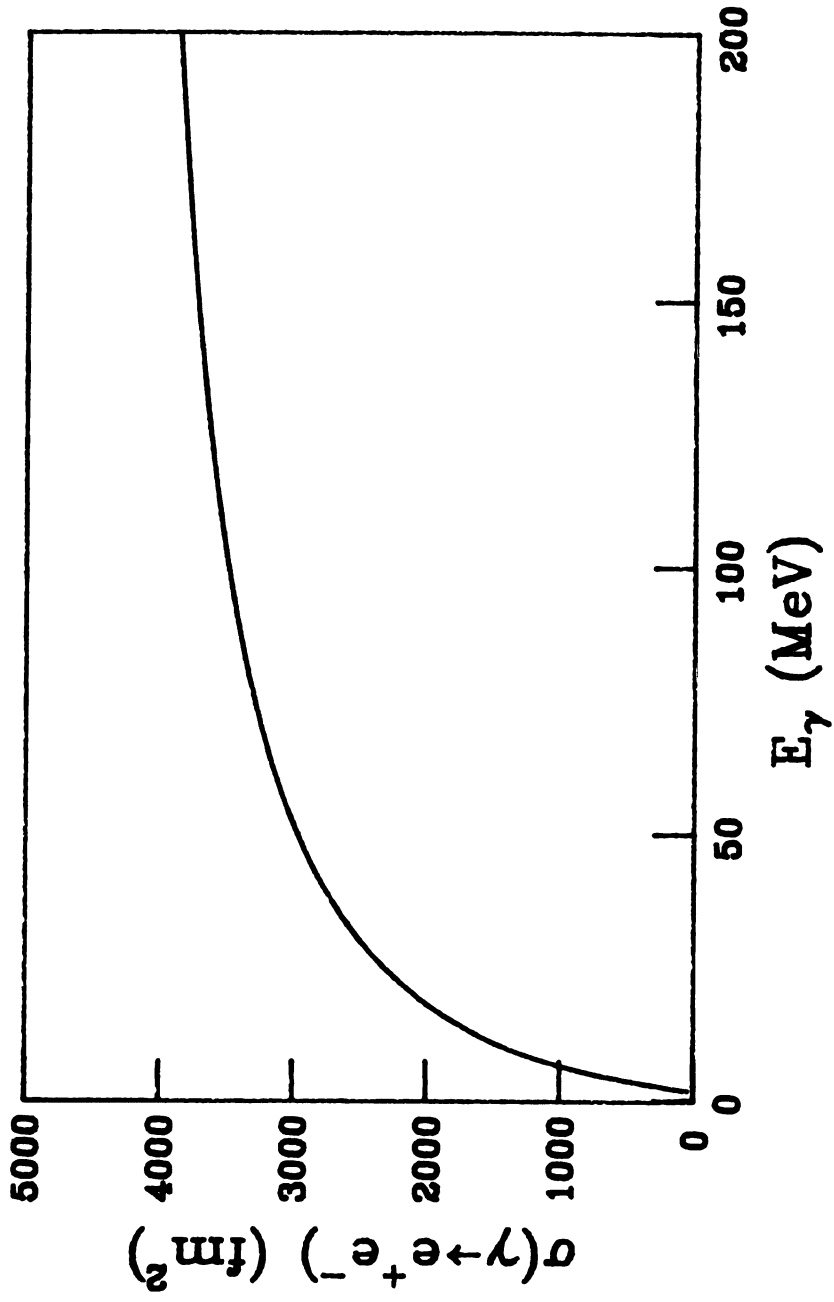


Figure 4.9. Total pair production cross section in Pb as a function of photon energy.

energ

array

for ph

fracti

of en

of the

energy

T

(lowe

positr

remove

in th

spectr

T

integ

cross

Figure

4.4 0

L

only c

number

gives

have

spect

addit

energies of interest. Subroutine ISIG generates with the array "sigT( $E_\gamma$ )"; the total pair production cross section for photons of energy  $E_\gamma$ , the array "Fze( $E_\gamma, E_+/E_\gamma$ )"; the fraction of the cross section for production of a positron of energy  $E_+$ , and the array XintFze( $E_\gamma, E_+/E_\gamma$ ); the fraction of the cross section for the production of positrons of energy equal to or less than  $E_+$ .

The output consists of a table of the positron energy (lower edge of a positron energy bin) and the number of positrons in the bin per  $10^6$  photons. The normalization removes the tables' dependence on the number of photons used in the calculation, which was typically  $10^7$  for each spectrograph setting.

The total cross section is found by numerical integration of the differential cross section. The total cross section as a function of energy for Pb is plotted in Figure 4.9.

#### 4.4 Other Processes

Both trident production and Compton scattering depends only on the electrons in a material. Both contribute to the number of high energy electrons, but only trident production gives rise to positrons. Positrons from trident production have lower energy and a more rapidly decreasing energy spectrum than positrons created by pair production. In addition, the cross section for pair production goes as  $Z^2$ ,

Yield (cts/nC--MeV)

Figure  
the p  
0°, 17  
spect  
positr

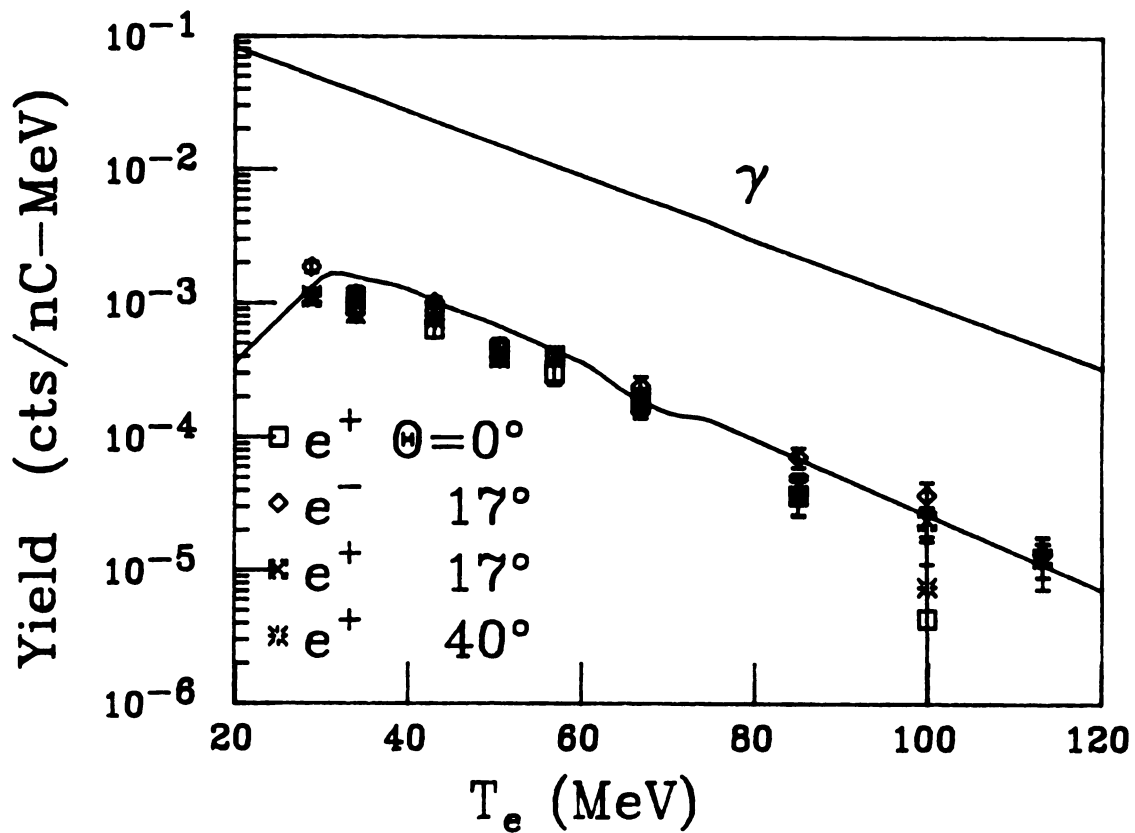


Figure 4.10. Superposition of the difference in yield from the Pb and Be converter for electrons at  $17^\circ$ , positrons at  $0^\circ$ ,  $17^\circ$ , and  $40^\circ$ . The solid lines are an assumed gamma-ray spectrum with a slope parameter of 18 MeV and the resulting positron spectrum from the calculation.

and s  
nucle  
of Z n  
electr  
all th  
and th  
pair pr  
positr  
procedu  
results

#### 4.5 Mod

It  
distri  
distri  
with th

in whic  
distri

where  
the co

and since there are Z times as many atomic electrons as nuclei, trident production is suppressed by about a factor of Z relative to pair production. Since the number of electrons in the converters is approximately constant for all three converters, taking the difference between the lead and the beryllium converters' yield reflects the nuclear pair production contribution. The ratio of the electron to positron yield in the data is about 3:2. Using the above procedure, the electron and positron data give very similar results (Figure 4.10).

#### 4.5 Modeling of the Target and Converter

It is necessary to assume some form of the  $\gamma$  ray energy distribution in order to run a simulation. Two simple distributions were chosen. The exponential distribution with the form:

$$\frac{dN}{dE} = K e^{-E/T}$$

in which T is called the slope parameter, and the Planck distribution used to describe black body radiation:

$$\frac{dN}{dE} = \frac{K E^2}{e^{E/T} - 1}$$

where T is the temperature. The exponential form used in the code GAMMAEE is particularly easy to use to produce an

appropriate random number generator, and is widely used to characterize distributions of fragments in heavy ion collisions [Be84]. The Planck form used in the similar code GAMMATEE would yield the temperature if the source were thermal, but requires numeric integrations to be performed to generate the random photon distribution using the subroutine PLANKGEN.

The photon energy is chosen using a random number generator according to the appropriate distribution. The full thickness of the copper target was assumed to be available for conversion. The photon interaction depth in the target is chosen such that the probability of the photon converting at a depth less than  $x$  is:

$$P(<X) = 1 - e^{-\lambda x}$$

where  $\lambda$  is determined using the integrated pair production cross section. If the depth chosen is less than the actual thickness of the target, the photon is converted, otherwise it passes into the converter, where the process is repeated. If a conversion has taken place, the energy of the positron is assigned using function XEFF, in accordance with the differential cross section's probability distribution. Energy is deducted for passing through the remaining converter or converter and target, and the information tabulated.

ignor

distr

conver

Since

target

B

these

or slo

material

name of

Afterwa

effect

Th

DIFFPB

lead an

similar

Pb-Be c

differ

of the

done b

only t

against

genera

value

Multiple scattering in the target and converter is ignored; its magnitude is discussed with the angular distribution in the previous chapter. The target and converter were kept normal to the spectrograph at all times. Since the target was stopping the beam, rotation of the target had no effect on the effective target thickness.

Both codes receive their instructions from a file; these include the number of photons to use, the temperature or slope parameter  $T$  for the trial photon distribution, the material and thickness of the target and converter, and the name of the output file. The code runs for many hours. Afterward, another program called EFOLDALL folds in the effect of the detector efficiency.

The resulting files are then read by another program, DIFFPBBE, which takes the difference in the yield for the lead and the beryllium converter and generates a file. A similar program, DIFFDATA, does the same for the data. The Pb-Be difference taken from the data is fit to the Pb-Be difference taken from the calculation for different values of the effective temperature or slope parameter  $T$ . This is done by the program DIFFIT, which fits the two by allowing only the overall scale to vary. A plot of the  $\chi^2$  of the fit against the effective temperature or slope parameter  $T$  is generated, and a quadratic fit is done to determine the value and uncertainty of  $T$  (Figure 4.11). Statistical

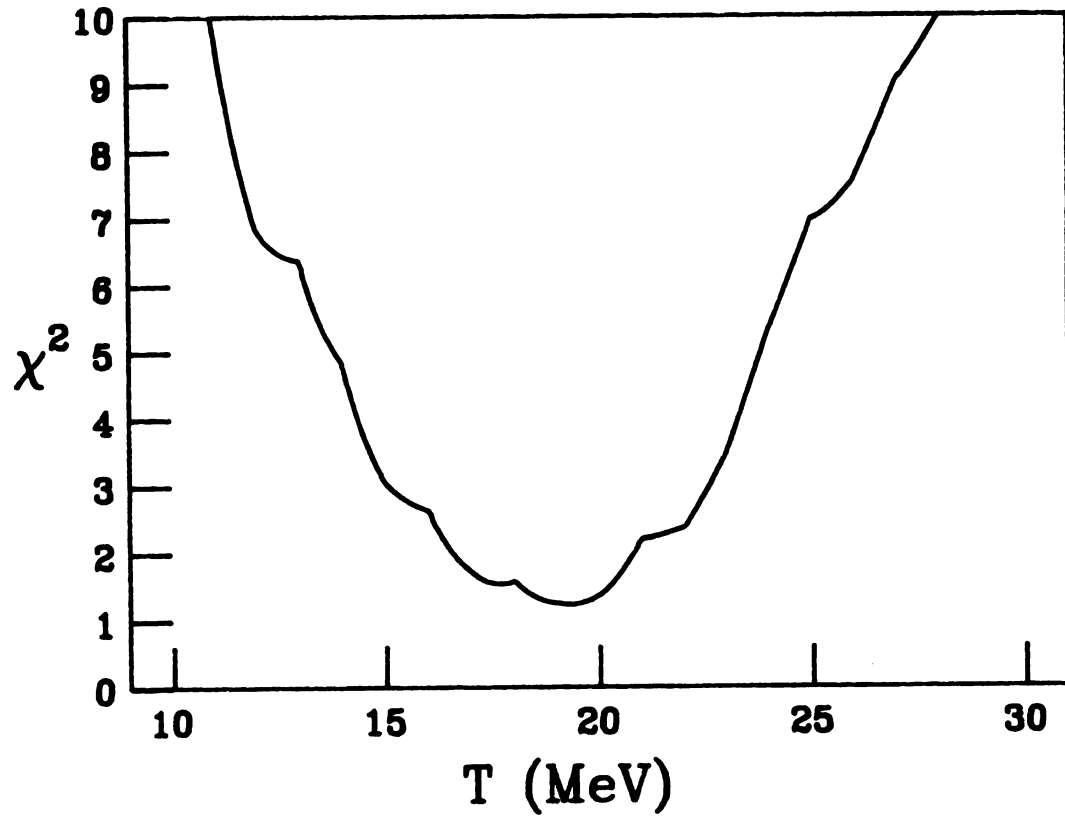


Figure 4.11. Typical plot of  $\chi^2$  vs. slope parameter.

YIELD ( $e^+$ /BEAM PARTICLE  $\cdot$  MeV  $\cdot$  sr)

$10^{-1}$   
 $10^{-2}$   
 $10^{-3}$   
 $10^{-4}$   
 $10^{-5}$   
 $10^{-6}$   
 $10^{-7}$   
 $10^{-8}$   
 $10^{-9}$   
 $10^{-10}$

Figure  
functi  
differ  
assumed  
solid c  
the con

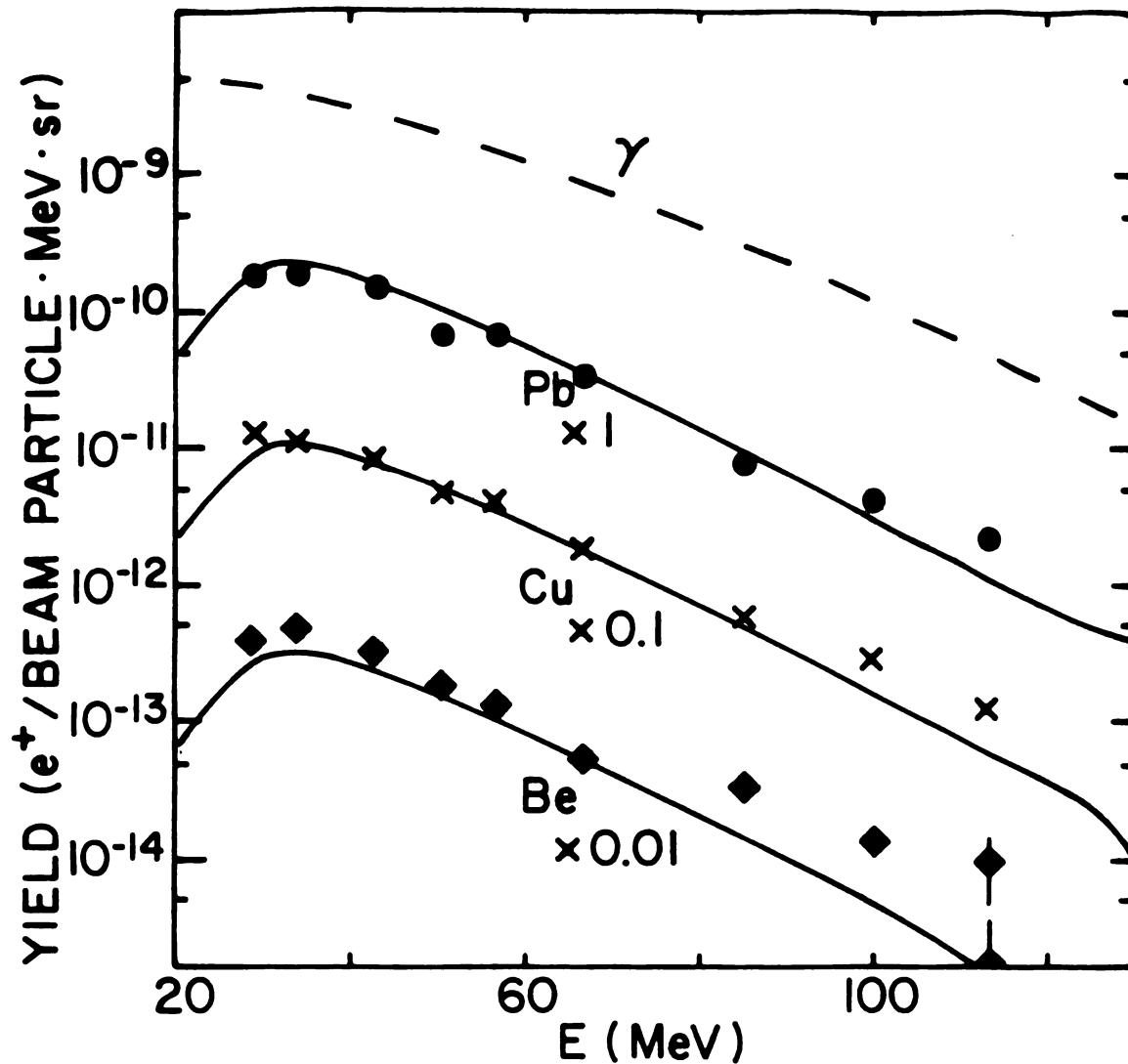


Figure 4.12. The data points give the  $e^+$  yield as a function of energy for  $^{14}\text{N} + \text{Cu}$  at  $E/A=40$  MeV for three different converters at  $\theta_L = 17^\circ$ . The dashed curve shows an assumed gamma-ray yield based upon a thermal source and the solid curves show results of the Monte Carlo calculation for the conversion positrons.

Table  
differ  
conver

a

1

4

Table 4.3. Parameter T values taken from a fit to the difference in positron results between the Pb and Be converters.

<u>angle</u>	<u>effective temperature</u> (MeV)	<u>slope parameter</u> (MeV)
0°	12.1 ± 2	17.2 ± 2.7
17°	12.2 ± 0.8	18.8 ± 1.8
40°	10.7 ± 1.4	15.8 ± 2.1

fluct

$\chi^2$  pla

in Tab

are s

distr

conver

done d

There

exponer

All

measur

produce

result

pair pr

Compto

only a

photon

on the

was se

the ber

fluctuations in both the calculations and the data make the  $\chi^2$  plot slightly erratic. The results of the fits are shown in Table 4.3.

The best fit calculation and the positron data for  $17^\circ$  are superimposed in Figure 4.12 using the Planck distribution. The calculation and data for the copper converter are also shown, and acts as a check on the fit done on the difference between the Pb and Be converter. There is little difference between the Planck and exponential photon spectra for the region of interest.

Although the original purpose of the experiment was to measure the positrons from pair production and those produced directly by the collision, it is clear from the results that the great majority of the positrons come from pair production, and the electrons from pair production and Compton scattering. Since only one beam energy was used, only a thick target yield was found; i.e.  $1.8 \pm 0.6 \times 10^{-6}$  photons with  $E_\gamma > 25$  MeV per beam particle. An upper limit on the number of direct positrons of 2% of the photon yields was set by estimating it to be less than  $1/2$  the yield with the beryllium converter.

## Chapter 5

## Gamma Ray Telescope Experiment

## 5.1 Introduction

The previous experiment demonstrated the existence of a relatively large cross section for the production of high energy gamma rays from heavy ion collisions. That experiment also showed that the yield was approximately the constant from 0 to  $40^\circ$ . It did not determine the beam energy dependence or a thin target cross section.

While another run at a different beam energy would have allowed a determination of the thin target cross section, the promise of these results led to the decision to build an entirely new detector to determine the beam energy and target mass dependence of this phenomenon. This detector would not use the spectrograph. In addition, this new detector, using thin targets, could be used at larger angles.

A new collaborator, Dr. J. Stevenson, formerly of Berkeley, developed the concept of the gamma ray telescope. Basically, the telescope consists of a converter backed by a stack of plastic Cherenkov counters (Figure 5.1). A high

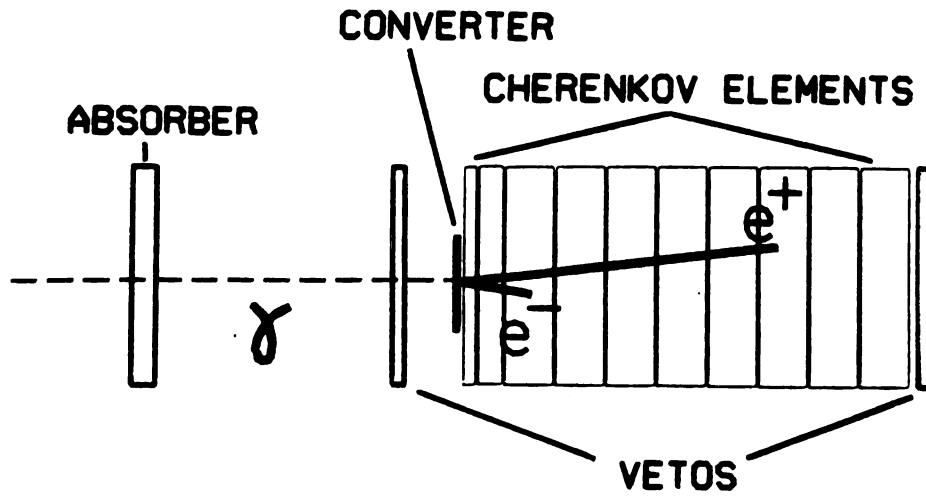


Figure 5.1. Concept of the High Energy Gamma-Ray Telescope.

energy photon is converted in the converter, and the electron and positron travel through and stop in the stack. The energy of the original photon is essentially the same as the energy of the electron-positron pair, which is determined by the range of the electron and positron in the telescope.

## 5.2 The Design of the High Energy Gamma Ray Telescope

Previous high energy gamma ray experiments have used lead glass shower detectors[Bu82],[No85],[He84]. These detectors use a single piece of leaded glass to convert the photon in an electron-positron pair. The pair in turn forms a shower of electrons, positrons, and photons. These electrons and positrons produce Cherenkov light which is measured. These devices require extensive Monte-Carlo simulations to determine their efficiency and are sensitive to pileup and cosmic rays[He84]. The resolution of shower detectors decreases rapidly with decreasing photon energy; for photons of 50 MeV the resolution of a lead glass shower detector is roughly 45%[Ag82]

The gamma ray telescope also converts the photon into a electron-positron pair, but because of its low atomic number does not form a shower. The members of the single pair slow and stop in the Cherenkov plastic. Unlike the lead-glass detectors, however, the light in each element is not summed to determine the energy loss of the pair. The light is used to determine the range of each member of the pair, from

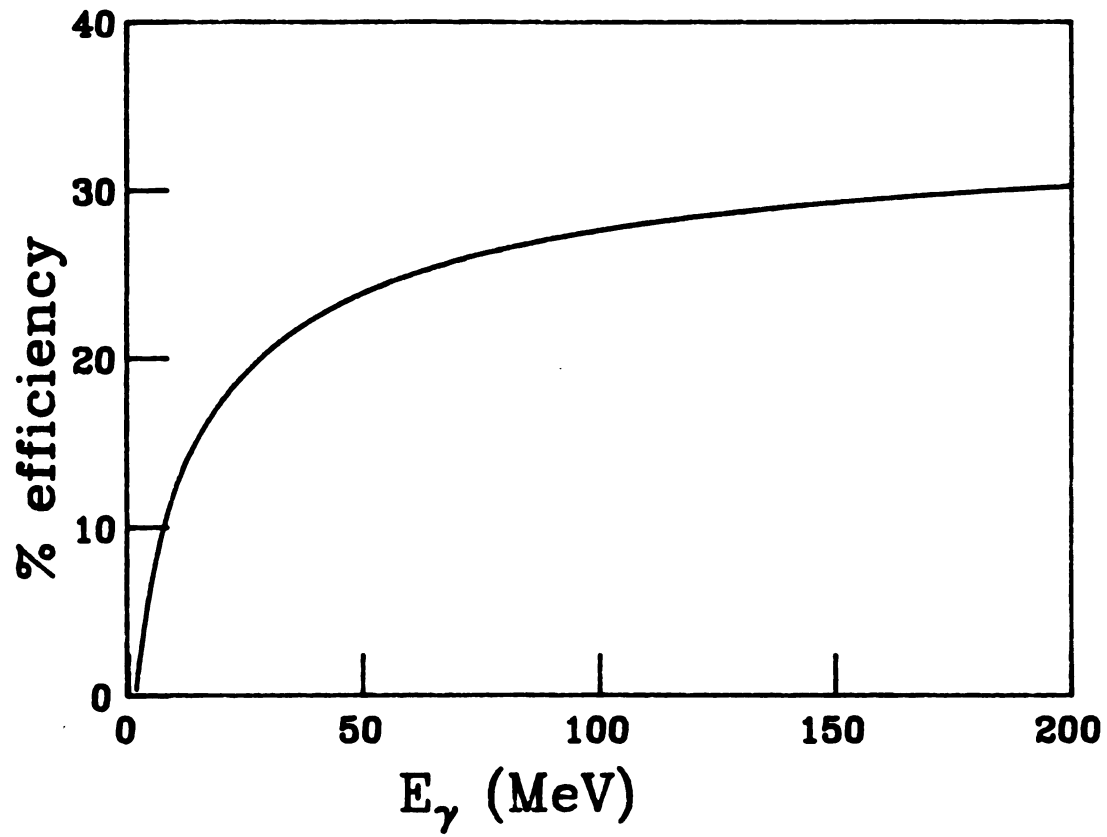


Figure 5.2. Efficiency of the CsI converter as a function of gamma-ray energy.

which the original energy of each member can be determined, and summed to give the original photon's energy.

The active converter is made of a high atomic number material, so that the probability of photon conversion is high. An inorganic scintillator, CsI, was chosen for high light output and high atomic number. Due to the poor quality of the surface of the 4"x4"x.1" crystal, the idea of total internal reflection for light collection from the crystal was discarded in favor of a light box. The light box is a low mass box of aluminum and cardboard, painted flat white inside except for the crystal making up the back wall. Two phototubes were used on the box. The light from the crystal would typically undergo many reflections before reaching the phototubes, and hence the light output was insensitive to the location of the conversion. The conversion efficiency of the crystal varied as a function of photon energy; a plot of efficiency against photon energy is shown in Figure 5.2, as calculated by using the techniques described in Chapter 4. The major limit on resolution in the gamma ray telescope is the uncertainty in the electron stopping position; this makes for a resolution of about 10% over the range of 10 to 200 MeV photons.

The stack of ten Cherenkov counters were made of low Z material, and the electron or positron was unlikely to lose energy except by scattering from the atomic electrons. The Cherenkov plastic re-emits the light isotropically and at a

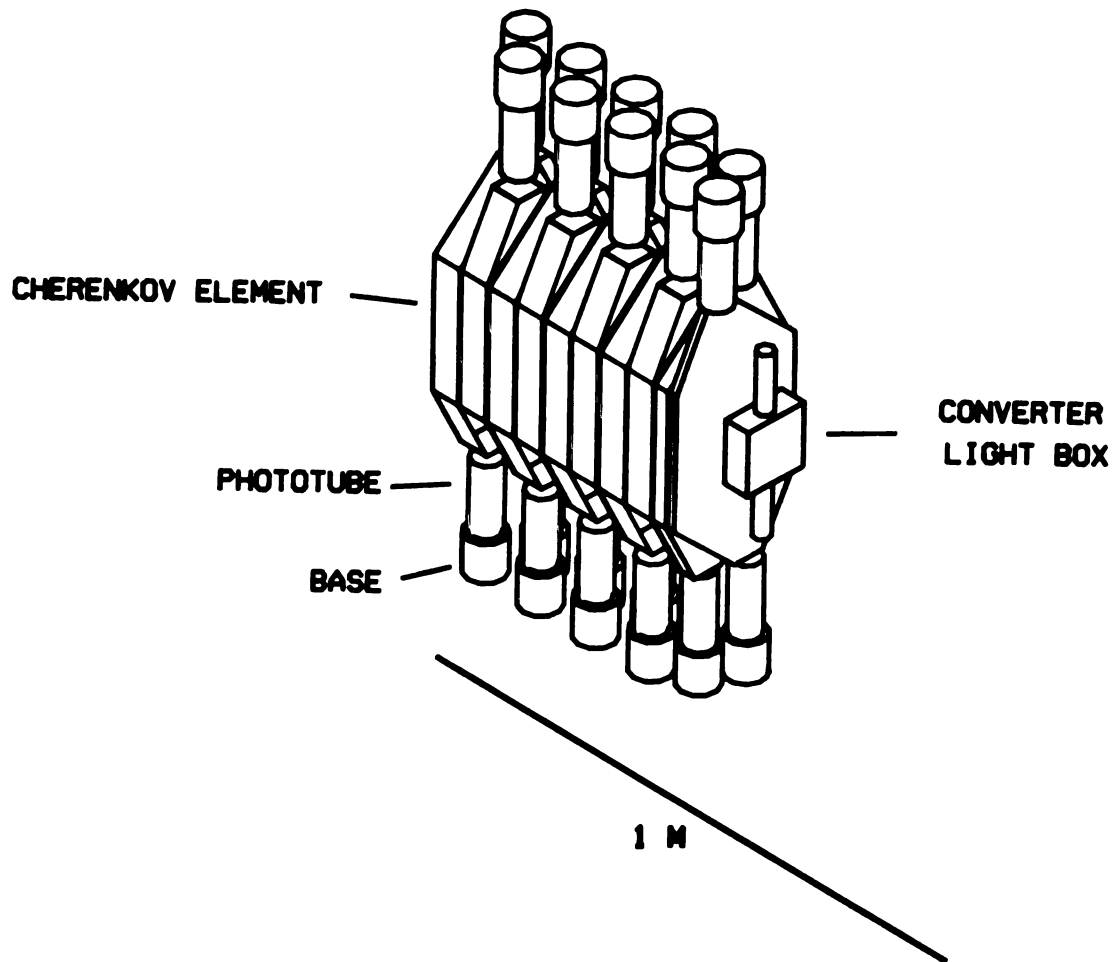


Figure 5.3. The High Energy Gamma-Ray Telescope.

longer wavelength, removing much of the position dependence of the signal.

While the area of each Cherenkov counter was the same (9"x9"), the first was .5", the second 1", and the rest 2" thick (Figure 5.3). This large area was required due to the multiple scattering of electrons and positrons, and the front elements were made thinner to allow better resolution of lower energy electrons and positrons.

To prevent electrons or positrons entering the front of the detector being counted as photons, a 0.5" scintillator veto was placed ahead of the converter. A second was placed behind the detector to detect electrons or positrons energetic enough to penetrate the Cherenkov stack. The high flux of charged particles coming from the target would saturate the veto, so a 1" carbon absorber was placed between the target and the veto scintillator.

### 5.3 The Experiment

In its first run, the gamma ray telescope was used on the neutron beam line where there was enough space to swing the detector from 30° to 120°. The neutron chamber was replaced with a very small chamber, and the Faraday cup was well shielded[Re83].

The pulse heights from the photomultiplier tubes were calibrated using cosmic ray muons traveling nearly horizontally through the detector. The electronics recorded the pulse height and time of the pulse from each phototube;

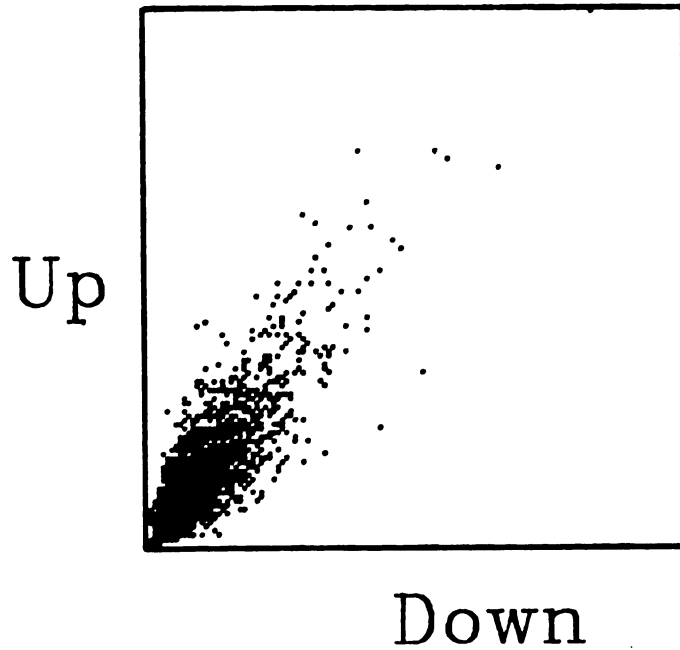


Figure 5.4. Output of the top phototube vs. output of the bottom phototube for a single element.

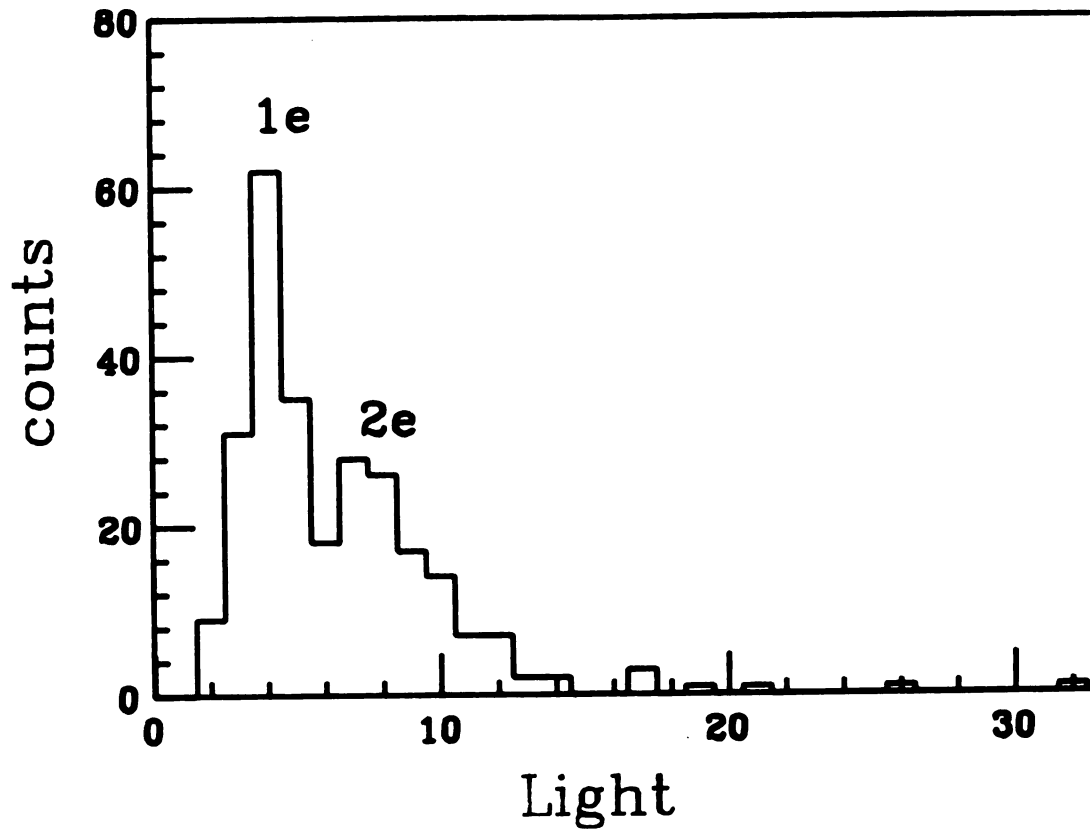


Figure 5.5. Output of one element gated by a higher element.

an event required the four phototubes of the first two Cherenkov elements to fire together. The fitting of each event to get the energy of the electron and positron for each pair was done offline.

The targets chosen were natural C, Ni, and Pb to span the mass range, similar to those used for subthreshold pion experiments. They were .006" (.152 mm), .002" (.051 mm), and .002" (.051 mm) thick respectively, corresponding to an energy loss of about 1.4 MeV/u when they were rotated to 30° to normal with respect to the beam [Li80]. The beam of  $^{14}\text{N}$  was selected since it had been used for both the previous measurement and subthreshold  $\pi^0$  experiments. It was also one of the highest current and energy beams available from the K500 cyclotron. The yield at 30°, 90°, and 120° in the laboratory was measured for each target at a beam energy of 40 MeV/u and for the Pb target at 30 MeV/u.

#### 5.4 The Results

Typical histograms from the experiment, showing the light output measured by the top phototube vs. light output measured by the bottom phototube in a single element is shown in Figure 5.4. Light in one element when gated by an event in the next higher element is shown in Figure 5.5.

The detector's efficiency as a function of photon energy was determined by the efficiency of the converter, the online requirement that the first two elements fire, the thickness of the detector, and the production of

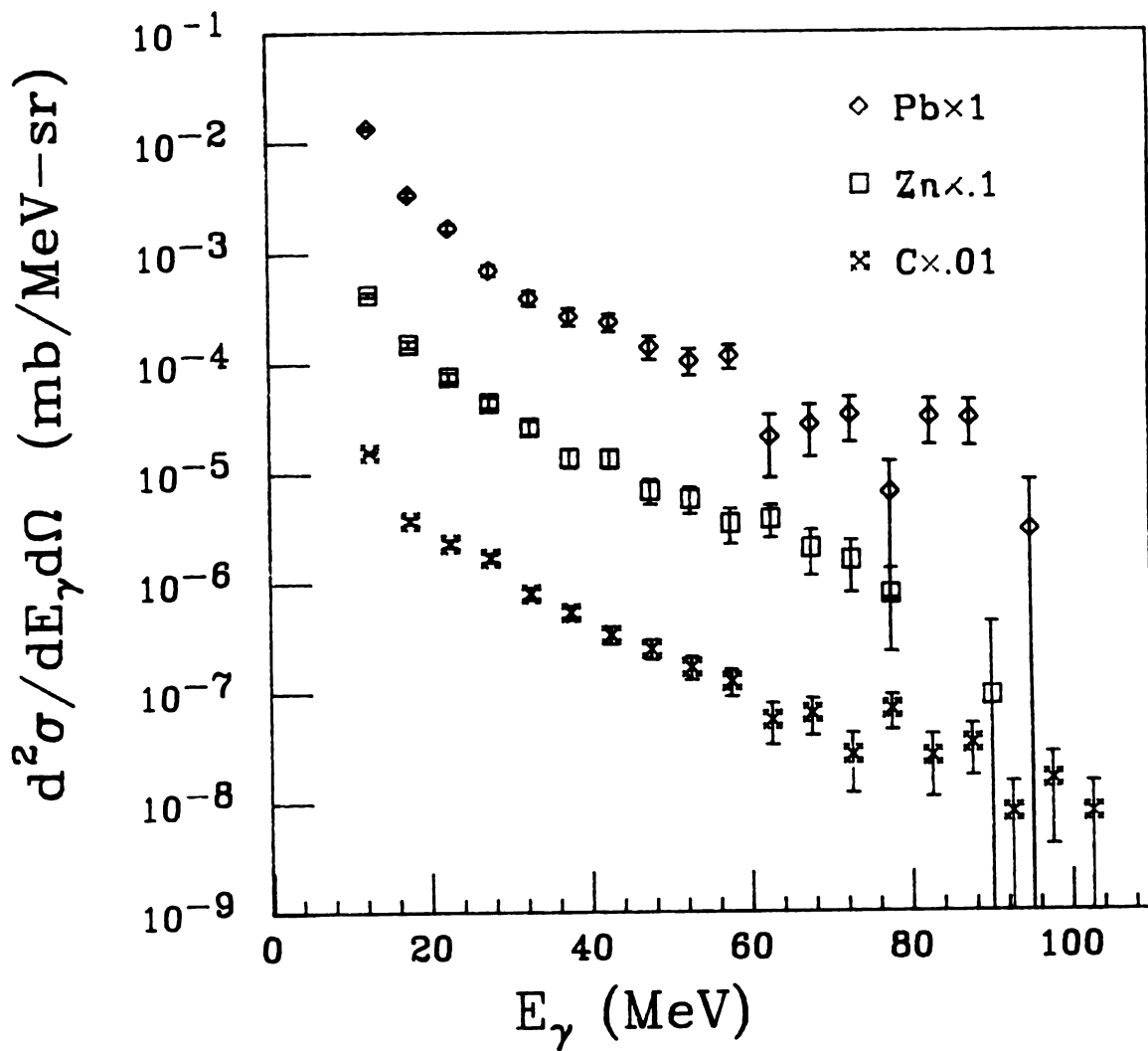


Figure 5.6. Gamma-ray cross section as a function of gamma-ray energy at  $\theta_{\text{Lab}} = 90^\circ$  for  $^{14}\text{N}$  on Pb, Zn, and C at 40 MeV/u.

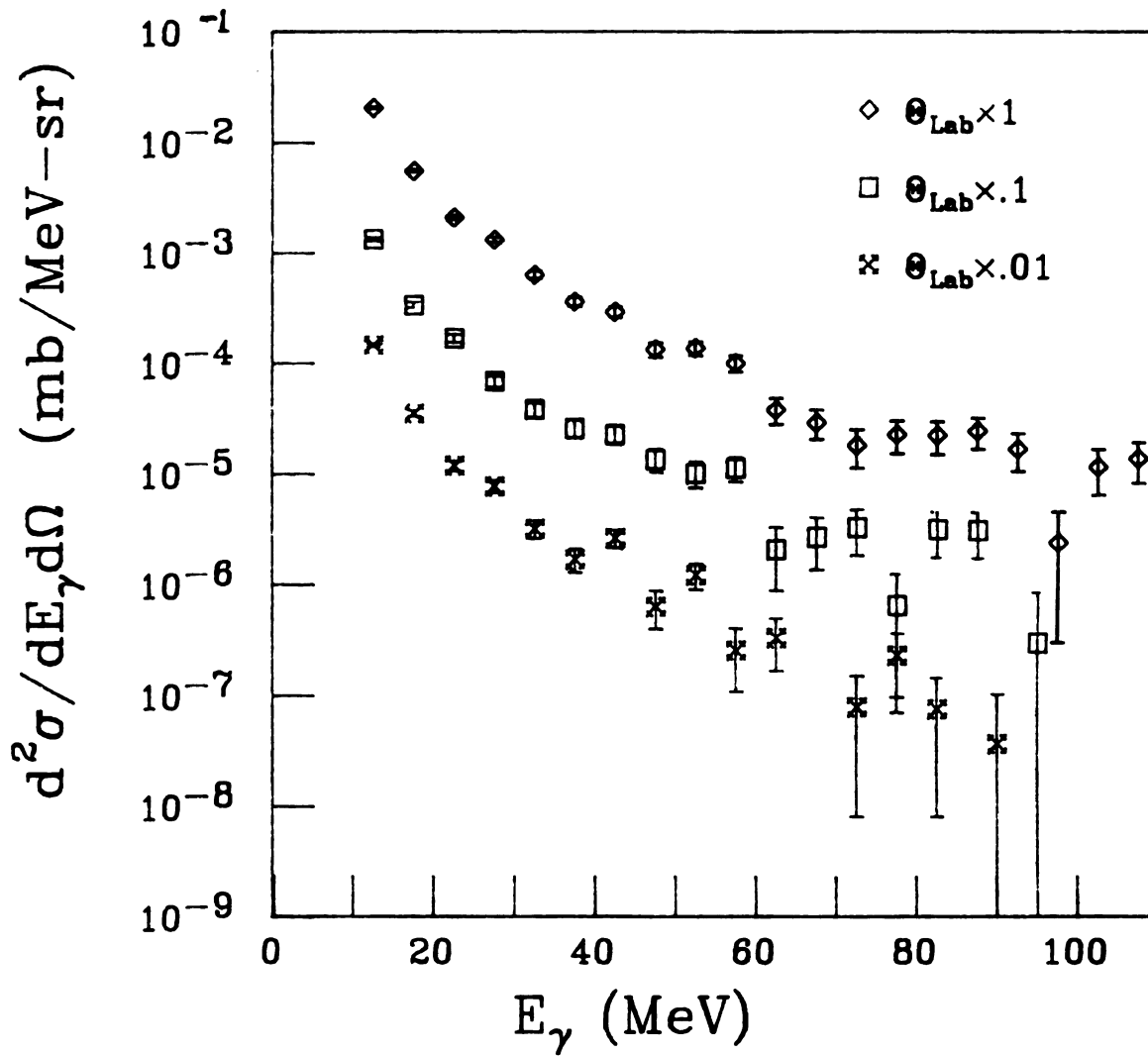


Figure 5.7. Gamma-ray cross section as a function of gamma-ray energy for  $^{14}\text{N}+\text{Pb}$  at 40 MeV/u at  $\theta_{\text{Lab}} = 30^\circ, 90^\circ,$  and  $150^\circ$ .

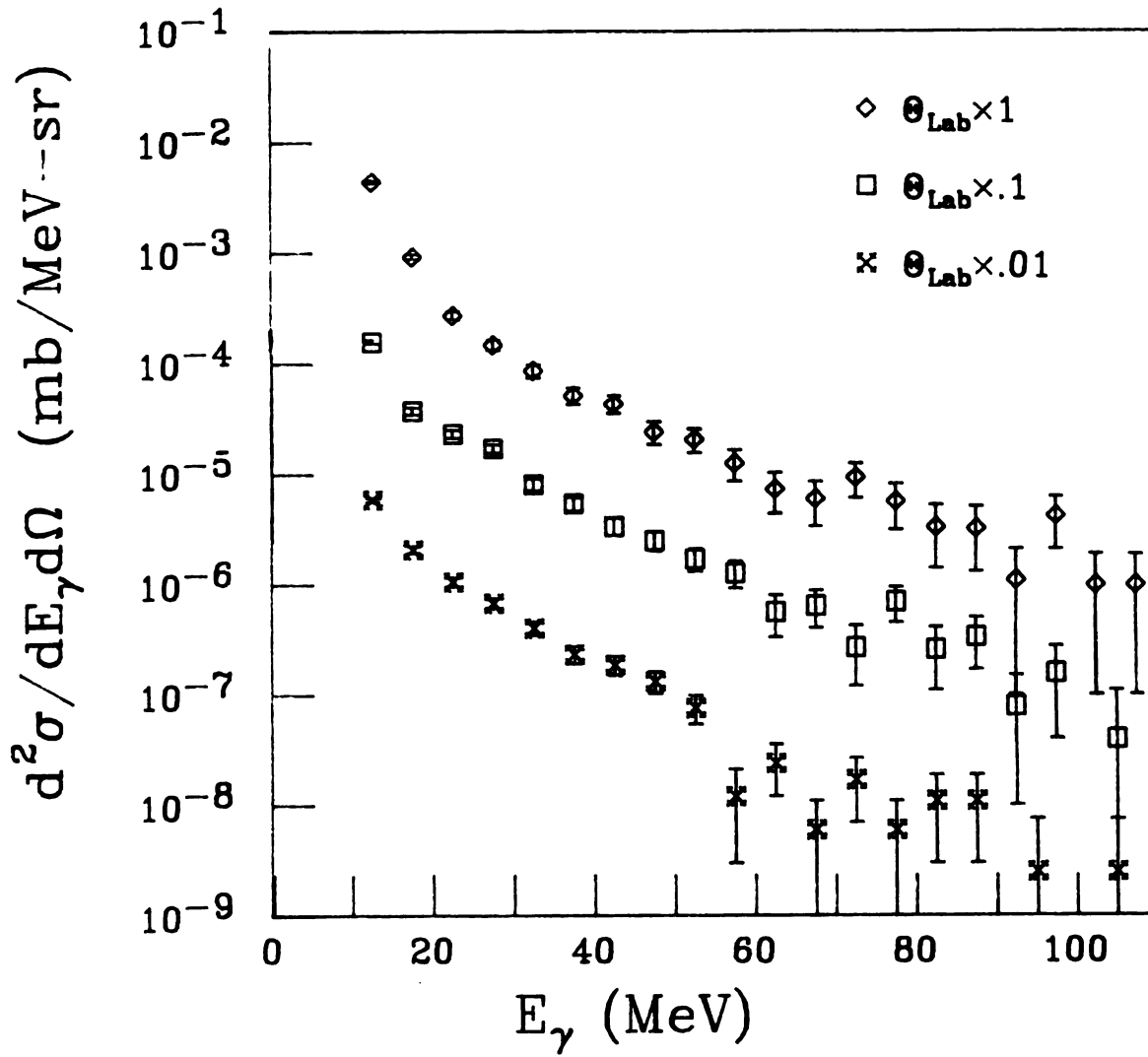


Figure 5.8. Gamma-ray cross section as a function of gamma-ray energy for  $^{14}\text{N}+\text{C}$  at 40 MeV/u at  $\theta_{\text{Lab}} = 30^\circ, 90^\circ,$  and  $150^\circ$ .

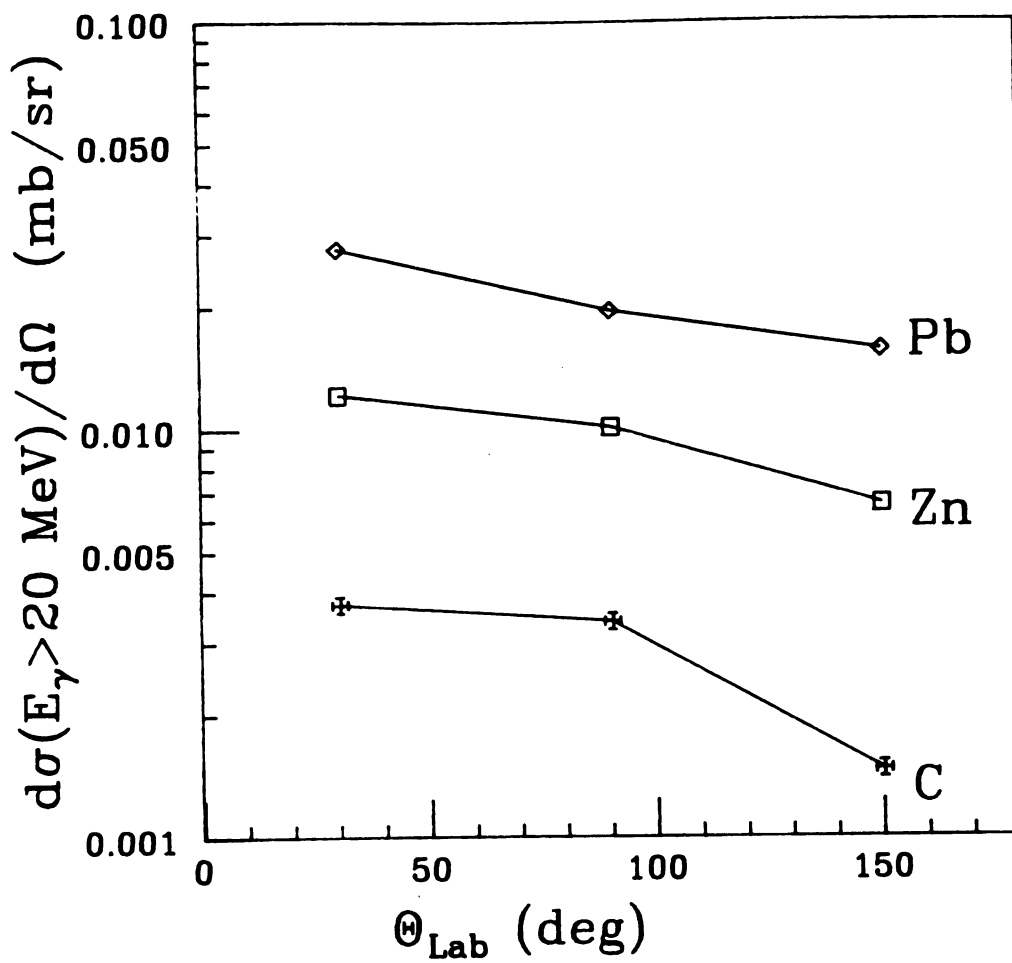


Figure 5.9. Integrated gamma-ray cross section for  $E_\gamma > 20 \text{ MeV}$  as a function of angle for  $^{14}\text{N}+\text{C}$ , Zn, and Pb at  $40 \text{ MeV/u}$ .

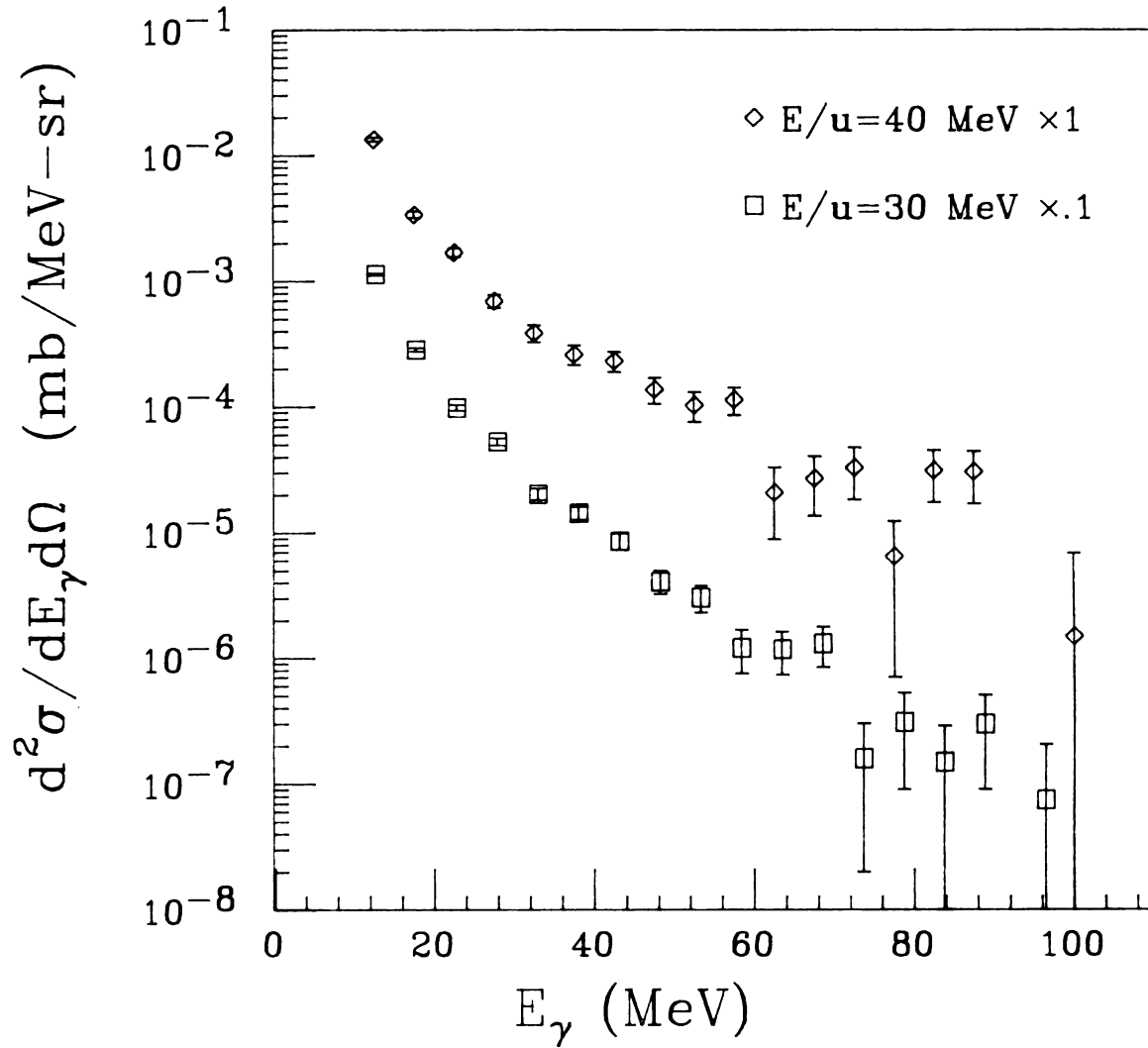


Figure 5.10. Gamma-ray cross section as a function of gamma-ray energy for  $^{14}\text{N}+\text{Pb}$  at 40 and 30 MeV/u at  $\theta_{\text{Lab}} = 90^\circ$ .

electromagnetic showers. The energy of the photons was extracted from the ranges of the electron and positron in the telescope. Figure 5.6 shows the photon cross sections at  $90^\circ$  for three targets, C, Zn and Pb, and Figures 5.7, 5.8, and 5.9 show the effect of laboratory angle for three targets. The yield is nearly independent of angle for the heavier targets, but the decrease in the yield with lab angle is most pronounced for the lightest target.

Figure 5.10 shows the photon data on the Pb target at 40 MeV/u and at 30 MeV/u. While the spectra for photons below 20 MeV are very similar, the spectra above that energy show quite different slopes.

## Chapter 6

## Theoretical Models

## 6.1 Comparison of Photons and Pions

Subthreshold pion production has been used for years as a probe in nucleus-nucleus collisions. Since pions are the lowest mass strongly interacting particle not originally present at the start of the collision, they are an important probe of the collision. Numerous theories have been advanced to explain the production of these pions far below the free nucleon-nucleon limit.

A natural comparison to make is between the pion cross section and the photon cross section. Figure 6.1 compares the photon cross section for  $^{14}\text{N}$  on Pb at 40 MeV/u and the  $\pi^0$  cross section for the same system at 35 MeV/u [Br84] times the ratio of phase space for  $\pi^0$ 's and  $\gamma$ 's. The ratio of the phase space can be found by:

$$\frac{V_{\gamma}}{V_{\pi^0}} = \frac{4\pi p_{\gamma}^2 dp_{\gamma}}{\frac{1}{3} \times 4\pi p_{\pi}^2 dp_{\pi}} = \frac{3E_T^2 dE_T}{p_{\pi}^2 \frac{E_T}{p_{\pi}} dE_T} = \frac{E_T}{3\sqrt{(E_T^2 - m_{\pi}^2)}}$$

The slope of the cross sections and the extrapolated overlap

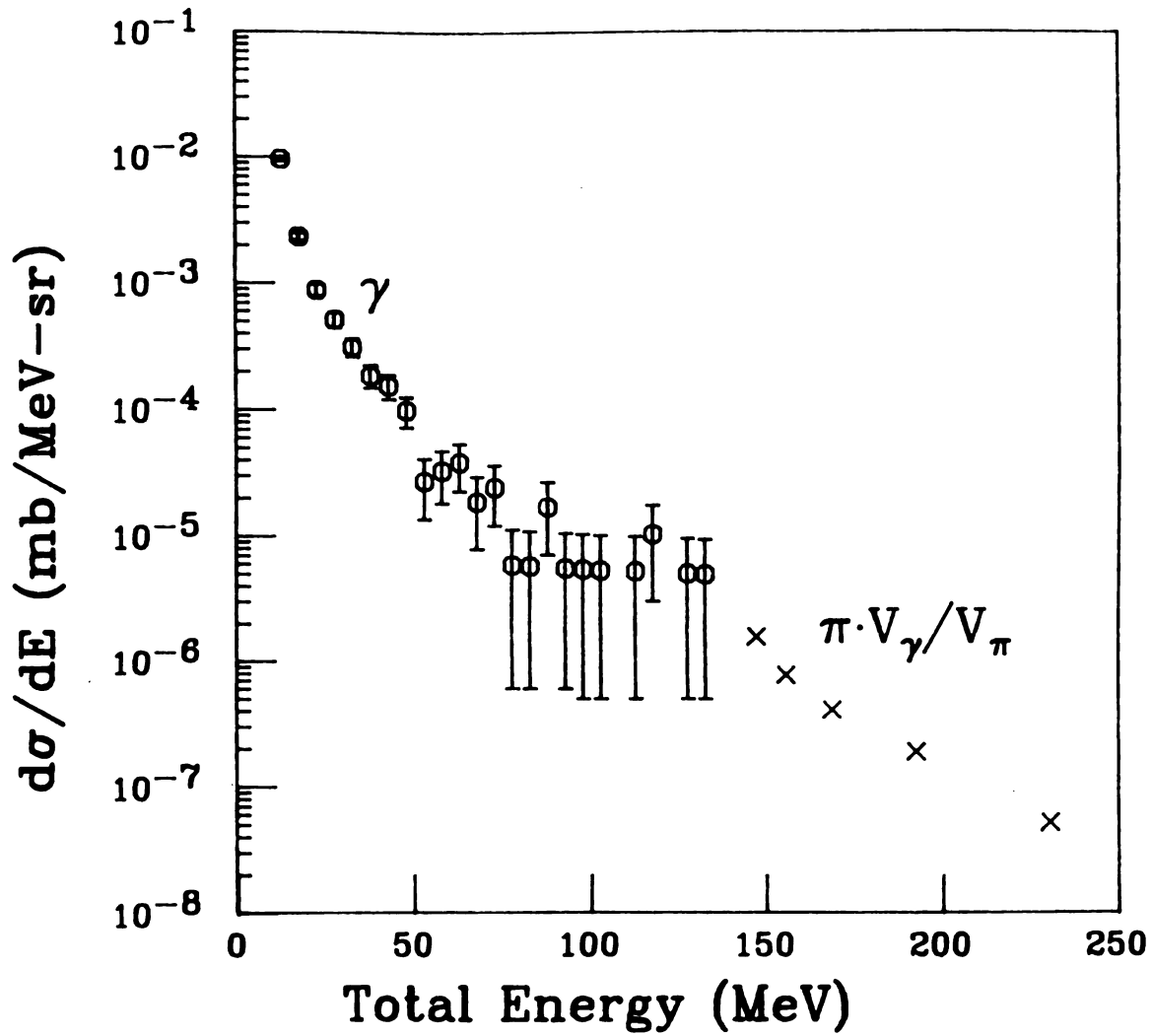


Figure 6.1. Comparison of the high energy gamma-ray cross section and the neutral pion cross section multiplied by the relative phase space as a function of the total energy of the photon or pion.

for the same total energy of photons and pions appears to be very similar.

This would suggest that the pions and photons are due to nearly identical processes, thus the measurements of photons would yield similar information to difficult subthreshold pion measurements at low beam energies.

Another piece of evidence linking the high energy photons and pions is the similarity of their angular distributions. Both are nearly isotropic, the pions having been measured by Braun-Munzinger et al [Br84] from 0 to 180°, and photons from 0 to 40° in the first experiment with  $^{14}\text{N} + \text{Cu}$ , and from 30° to 150° with  $^{14}\text{N} + \text{Pb}$ ,  $\text{Zn}$ , and  $\text{C}$  in the second experiment. The departure from isotropy in the  $^{14}\text{N} + \text{C}$  data can be explained as an isotropic distribution in the center-of-mass frame distorted by the large velocity of the center of mass for the light system.

When the high energy photons were found, several pion theories were quickly extended to include photons. The first of these was the pionic bremsstrahlung model of W.Greiner [Va84]. Since the pionic bremsstrahlung was the analog to classical bremsstrahlung, it seemed an ideal test of the model. H.Stöcker and D.Hahn produced a modified form of their hydrodynamic model [Ha85a, Ha85b], and shortly later J.Aichlein and G.Bertsch produced a calculation [Ai85].

The cascade models, which describe nucleus-nucleus collisions in terms of the sum of the individual nucleon-nucleon collisions, have been successful in describing

particle production at higher energies. Richman[Ri50] suggested using the pion yield to determine the number of nucleon-nucleon pairs having sufficient energy to create a pion, and hence the Fermi distribution of the original nucleus. As the beam energy is decreased, the cascade model predicts a pion yield that is too small. Pion production has been measured as low as 25 MeV/u[St85a]. A new microscopic approach by W.Bauer using a large time dependent Hartree-Fock model corrects some of the deficiencies, but has not yet been calculated for the systems studied here[Ba86].

The thermal models also have problems at the low beam energies with the pion cross section; the pion represents a large share of the available energy in the collision, but why this energy is not rapidly dissipated among the nucleons is difficult to explain.

These problems led to a third class of theories, all using the concept of bremsstrahlung. Electromagnetic bremsstrahlung is a well understood classical phenomenon; Greiner et al.[Va84] introduced pionic bremsstrahlung, where the virtual photons of the electromagnetic field are replaced by the virtual pions of the strong nuclear field. The important free parameter in this theory is the stopping time of the nucleus in the collision.

If pionic bremsstrahlung occurs, then electromagnetic bremsstrahlung should also occur. Experiments have been done at higher energies[Bu82] to look for this, but nothing

had been published for searches in the intermediate energy range. The observation that high energy  $e^+$  and  $e^-$  were being detected, discussed in Chapter 2, strongly suggested that electromagnetic bremsstrahlung was indeed taking place. If this were the case two entirely different probes, pions and photons, should yield the same stopping time.

Ko suggested that electromagnetic bremsstrahlung may be observed, and have two components; a coherent part due to the net motion of the nuclei, and an incoherent part due to nucleon-nucleon collisions[Ko85].

## 6.2 Coherent Bremsstrahlung

The uncertainties in the calculation of bremsstrahlung from the nucleus-nucleus collision lie entirely with the collision process itself; electromagnetic bremsstrahlung is well described. A question remains, however, whether the photons add coherently or incoherently. The photons of interest are from 20-100 MeV, with a wavelength of about 62-12 fm. The radius of the  $^{14}\text{N}$  nucleus is about 2.9 fm, using the relation [Pr75]

$$R = r_0 A^{1/3} \quad r_0 = 1.2 \text{ fm}$$

so the wavelength of the photons is larger than the size of the interacting region, suggesting that coherent emission is likely.

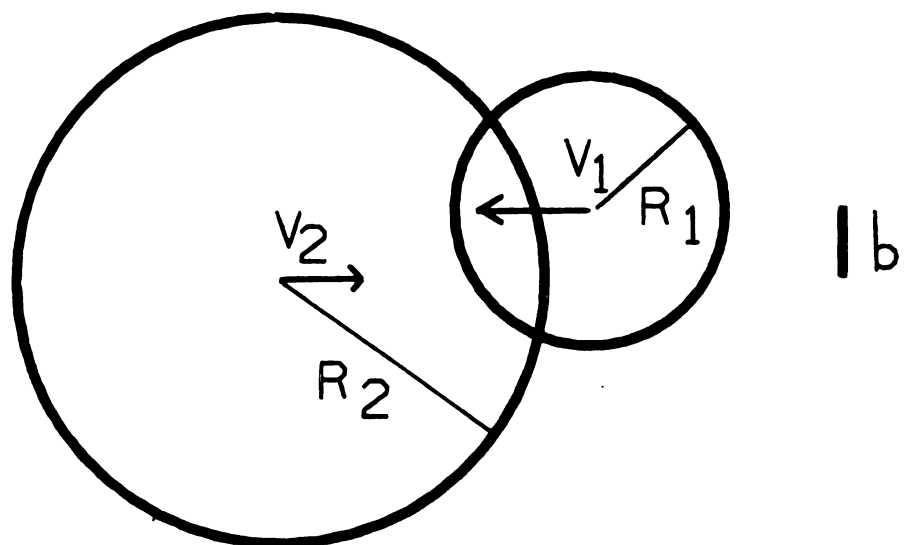


Figure 6.2. System used in the coherent bremsstrahlung calculation.

A simple model of coherent bremsstrahlung was made using a classical model by Budiansky[Bu82]. Starting with the familiar equation from Jackson [Ja75], the intensity of radiation emitted during the collision can be expressed (in esu units) as:

$$\frac{d^2 I}{d\omega d\Omega} = \frac{\omega^2}{4\pi^2 c^3} \left| \int dt \int d^3x \mathbf{n} \times [\mathbf{n} \times \mathbf{J}(\mathbf{x}, t)] e^{i\omega(t - \mathbf{n} \cdot \mathbf{x}/c)} \right|^2$$

To convert this expression into a form expressing the number of photons  $N_\gamma$  per photon energy interval  $E_\gamma$  per solid angle just divide by  $\hbar^2 \omega$ .

$$\frac{dN_\gamma^2}{dE_\gamma d\Omega} = \frac{1}{\hbar^2 \omega} \frac{d^2 I}{d\omega d\Omega}$$

The collision can be modeled as two spheres of uniform charge colliding along the  $\hat{z}$  axis. The spheres interpenetrate without distortion, exponentially slowing to a stop. This model is described in detail in [Bu82], but is restricted to impact parameter  $b=0$ .

A straight forward extension is to consider  $b \neq 0$  (Figure 6.2), which is calculated by the program BREMIW and its subroutines. The details of the calculation appear in Appendix A. The results of the code BREMIW for  $^{14}\text{N} + \text{Pb}$  are shown in Figures 6.3 and 6.4.

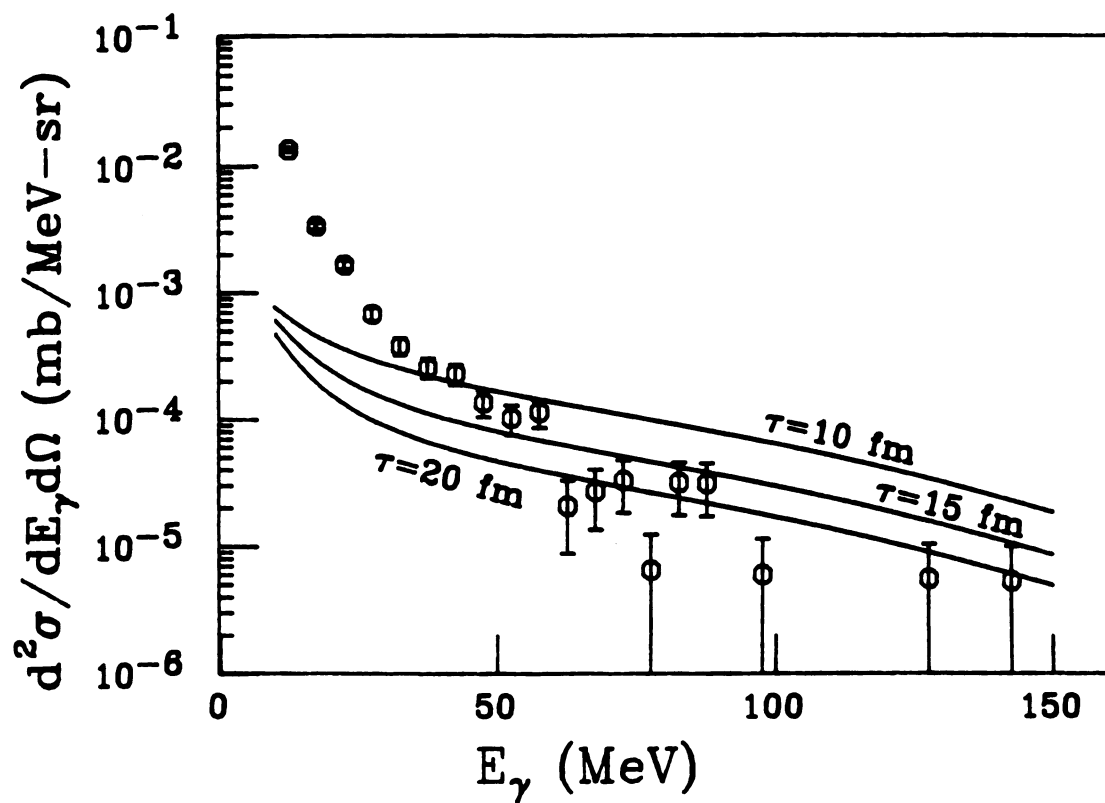


Figure 6.3. Cross section for the coherent bremsstrahlung model as a function of gamma-ray energy for  $^{14}\text{N}+\text{Pb}$  at 40 MeV/u and  $\theta_{\text{Lab}} = 90^\circ$  with stopping times of 10, 15, and 20 fm/c.

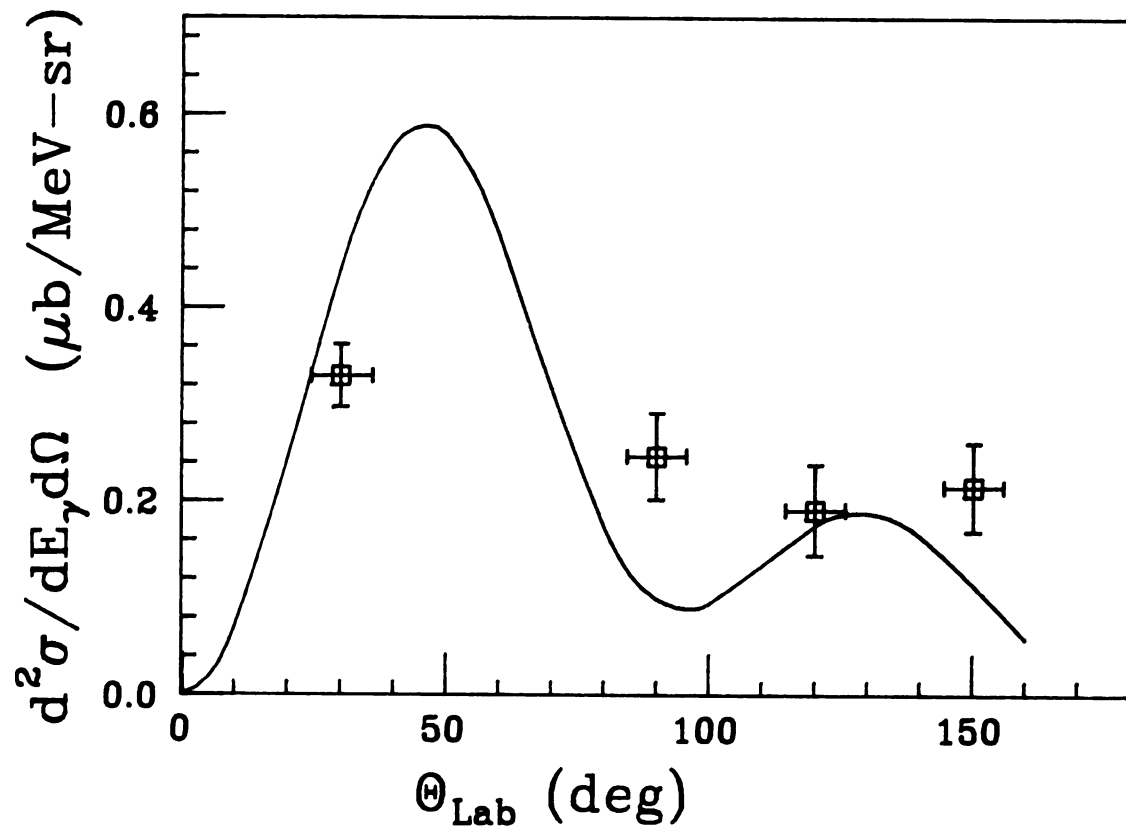


Figure 6.4. Cross section for  $^{14}\text{N}+\text{Pb}$  at 40 MeV/u as a function of lab angle for  $E_\gamma = 40$  MeV using the coherent bremsstrahlung model with  $\tau=15$  fm/c.

Table 6.1. The angle between the original direction and the direction at impact for two nuclei just touching.

<u>system</u>	<u>lab deflection angle</u>
40 MeV/u $^{14}\text{N} + \text{Pb}$	3.87°
40 MeV/u $^{14}\text{N} + \text{C}$	0.52°
30 MeV/u $^{14}\text{N} + \text{Pb}$	5.29°

The Coulomb force deflects the trajectory of the two nuclei, so that for impact parameters not equal to zero, the axis of motion is rotated. The maximum amount of the rotation occurs when the two nuclei just touch, and is about one half the grazing angle[NØ76]. For the systems under consideration, this rotation is insignificant (Table 6.1).

### 6.3 Hard Sphere Bremsstrahlung

Another estimate of the coherent bremsstrahlung, suggested by Stevenson [St85a], is to use a model of two hard spheres bouncing off each other to model the collision. The center-of-mass scattering angle of the nuclei is entirely dependent on the impact parameter  $b$ .

The size of the maximum impact parameter taken has an effect on the shape of the angular distribution. Taking the maximum impact parameter to be that of a glancing collision,  $b=R_1+R_2$ , completely removes the minimum near  $90^\circ$  (Figure 6.5 and 6.6).

Although this is not a very realistic model of the collision and greatly overpredicts the photon yield, it represents the other extreme to the interpenetrating spheres model.

### 6.4 Fireball

A successful model used to explain the particle spectra observed in intermediate energy nucleus-nucleus collisions is the fireball model or hotspot[Go77]. In this model, the

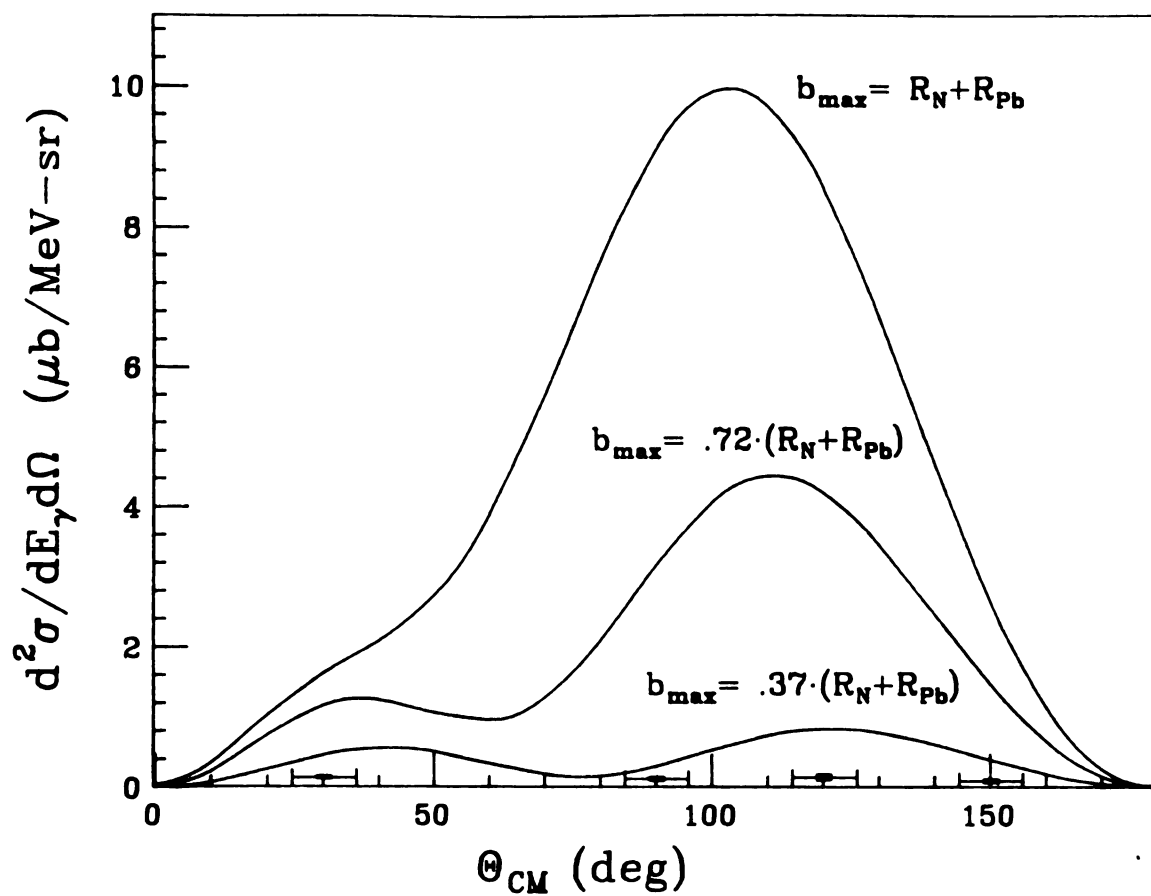


Figure 6.5. Cross section for  $^{14}\text{N}+\text{Pb}$  at 40 MeV/u and  $E_\gamma = 50$  MeV using the hard sphere bremsstrahlung model for various maximum impact parameters.

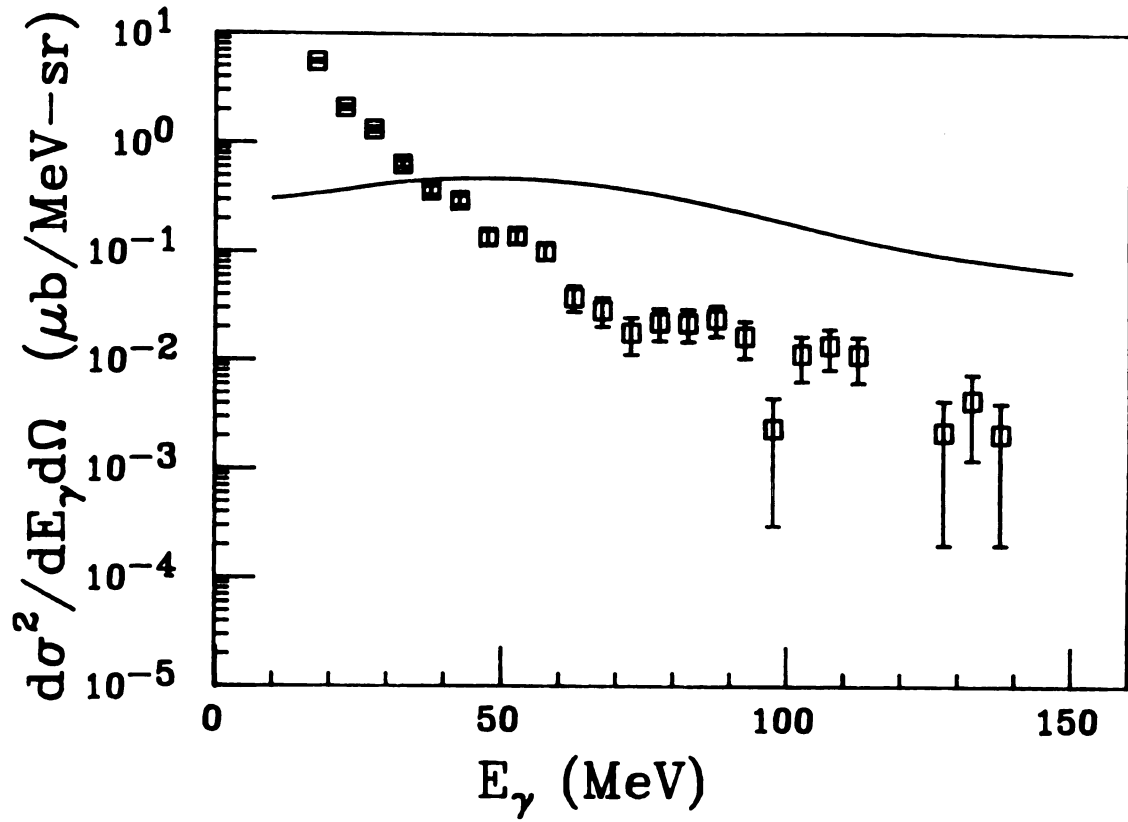


Figure 6.6. Cross section for  $^{14}\text{N}+\text{Pb}$  at 40 MeV/u and  $\theta_{\text{lab}} = 30^\circ$  using the hard sphere bremsstrahlung model with the maximum impact parameter 37% of the radii.

overlapping region of the colliding nuclei forms a hot region which evaporates particles. By applying the black body equation to the hot spot and knowing the size and temperature of the hot spot, the approximate photon yield can be calculated.

As a simple model of a fireball (function FIREBALL), the number of participant nucleons and the volume of the hot region is set equal to the overlap of the two spherical nuclei passing through each other. The volume swept out is calculated in Appendix A.

The temperature is found by assuming all the thermal energy comes from the kinetic energy per nucleon of the participants in the center-of-mass frame of the fireball. Calculated size and temperature of the fireball as a function of impact parameter for  $^{14}\text{N} + \text{Pb}$  is shown in Table 6.2.

In a black body of temperature  $T$ , the energy density with angular frequency  $\omega$  is [Be70]:

$$u(\omega) = \frac{1}{\pi^2 c^3} \frac{\hbar \omega^3}{e^{\hbar \omega / T} - 1} d\omega$$

So the number of photons in volume  $V$  is

$$dN = \frac{u(\omega)}{\hbar \omega} \cdot V_0 = \left[ \frac{\hbar \omega}{\hbar c} \right]^2 \frac{1}{\pi^2 \hbar c} \frac{V}{e^{\hbar \omega / T} - 1} d(\hbar \omega)$$

The hotspot is taken to be normal nuclear density containing

Table 6.2. Fireball parameters for  $^{14}\text{N}+\text{Pb}$  at 40 MeV/u.

<u>b (fm)</u>	<u>A<sub>1HS</sub></u>	<u>A<sub>2HS</sub></u>	<u>T (MeV)</u>
0.00	14.01	49.45	4.57
1.20	14.01	48.63	4.61
2.40	14.01	46.09	4.74
3.60	14.01	41.36	5.01
4.80	13.51	32.61	5.49
6.00	10.39	21.35	5.84
7.20	6.142	11.31	6.05
8.40	2.321	3.944	6.18
9.60	0.163	0.261	6.28

A nucleons, so

$$V = \frac{4}{3}\pi R^3, \quad R = r_0^3 \cdot A^{1/3} \quad r_0 = 1.2 \text{ fm}$$

Allowing all the photons to leave isotropically,

$$\frac{dN}{dE_\gamma d\Omega} = \frac{1}{3\pi^2 \hbar c} \left[ \frac{\hbar \omega}{\hbar c} \right] \frac{r_0^3 A}{e^{\hbar \omega / T} - 1}$$

When an impact averaging is done (program BLACKBODY), using this simple fireball model to find the number of participant nucleons and the temperature T, the results are shown in Figure 6.7. While this model predicts the observed (nearly) isotropic angular distribution (Figure 6.8) and the slope of low energy component, it greatly underpredicts the high energy component.

A serious objection to this model can be made; the assumption that the black body is much larger than the wavelength of the photons involved is no longer true. For example, consider a hotspot of 28 nucleons (twice the mass of the  $^{14}\text{N}$  beam used for these experiments). The diameter of a sphere of normal nuclear density is

$$d = 2(1.2 \cdot A^{1/3}) = 7.3 \text{ fm}$$

The lowest mode possible a cube of dimension d is

$$\frac{\omega}{c} = \frac{\pi}{d}, \quad \hbar \omega = \hbar c \cdot \frac{\pi}{d} = 85 \text{ MeV}$$

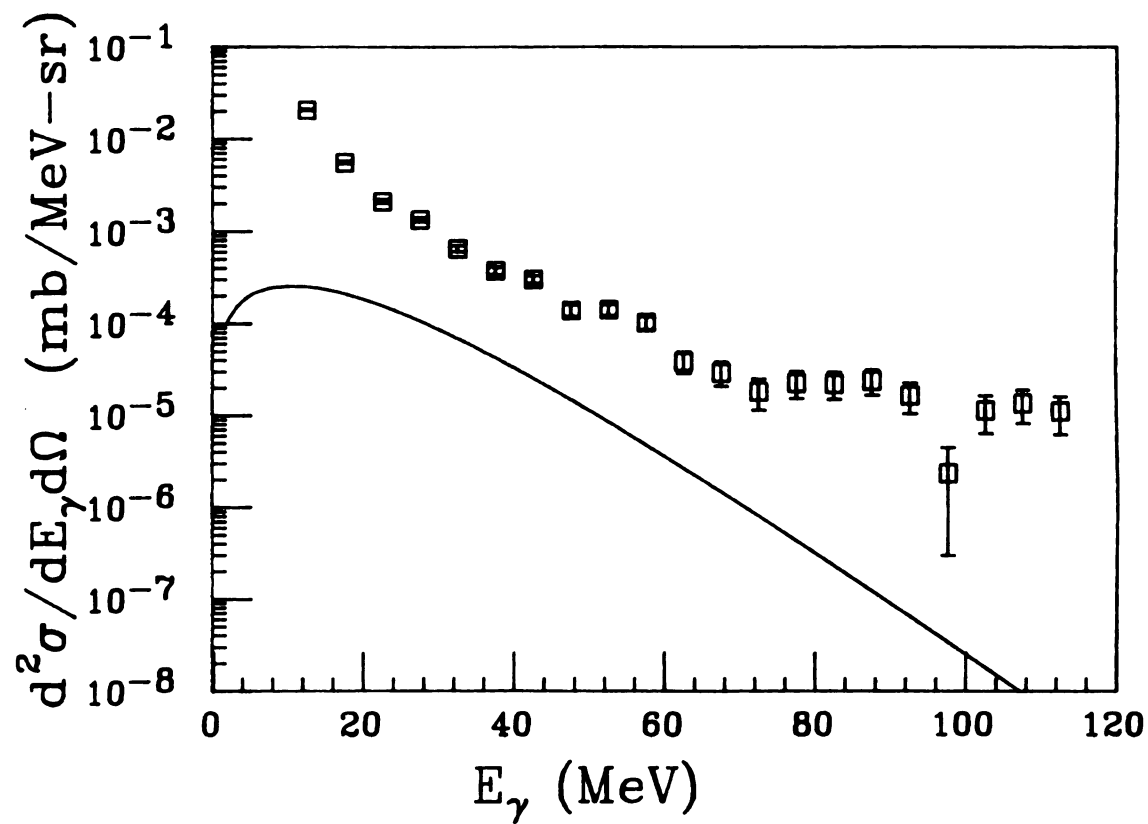


Figure 6.7. Cross section for  $^{14}\text{N}+\text{Pb}$  at 40 MeV/u and  $\theta_{\text{Lab}} = 30^\circ$  using the fireball model.

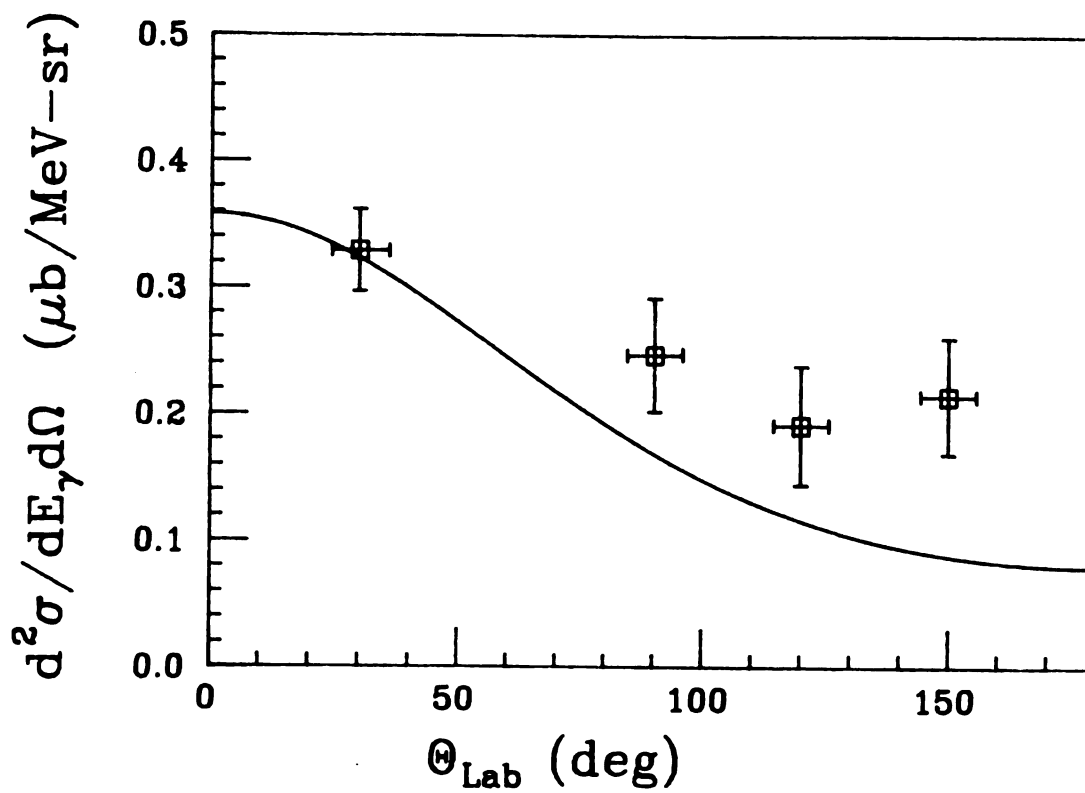


Figure 6.8. Cross section for  $^{14}\text{N}+\text{Pb}$  at 40 MeV/u and  $E_\gamma = 40$  MeV using the fireball model.

sug

be

6.5

ca

fi

in

th

co

an

ph

a.

c

a

p

p

c

a

n

(

suggesting that no photons of energy less than 85 MeV could be due to black body radiation.

### 6.5 Incoherent Bremsstrahlung From the Fireball

Black body radiation is not the only way the fireball can make gamma rays. Nucleon-nucleon collisions within the fireball produce bremsstrahlung. This model of the incoherent bremsstrahlung is significantly different from that done by Ko[Ko85]. In that model, the nucleon-nucleon collisions occurred between target and projectile nucleons and produced a  $1/\omega$  dependence of the photon cross section on photon energy and an anisotropic angular distribution.

The energies of the nucleons in the fireball are assumed to have a Boltzmann velocity distribution. For a collision between two nucleons, the scattering can be approximated as being isotropic scattering of point like particles since the nucleons are much smaller than the photon wavelengths of interest. To order  $\beta^2$ , only p-n collisions contribute to bremsstrahlung. The scattering angle and emission angle averaged photon production from an n-p collision is weighted by all collisions of energy  $\epsilon \geq M\omega$  (Appendix A) is:

Table 6.3 Temperature of the fireball used in the incoherent bremsstrahlung model.

<u>T<sub>lab</sub></u> (MeV/u)	<u>T</u> (MeV)
40	12
30	10
20	8

$$\frac{d^2N}{dE_\gamma d\Omega}(\bar{\epsilon}) = \frac{e^2 T}{3\pi^2 \hbar c E_\gamma m c^2} \left[ \frac{1}{\sqrt{3} - 1} \right]$$

$$\cdot \left\{ \left( \frac{1}{\sqrt{\pi}} - \frac{1}{4} \right) + \left( \frac{2}{\sqrt{\pi}} - \frac{1}{2} \right) \left[ \frac{E_\gamma}{T} \right] + \left( \frac{1}{\sqrt{\pi}} \right) \left[ \frac{E_\gamma}{T} \right]^2 \right\} e^{-2E_\gamma/T}$$

About 1/4 of the nucleon-nucleon collisions are p-n. The mean distance out of a sphere along any straight path is 1.177R, where R is the radius. The mean free path is

$$\lambda = \frac{3/\sqrt{V_0}}{\sqrt{A}} = 1.2 \sqrt{\frac{3}{4\pi}}$$

so the probability of an n-p collision per nucleon is

$$p_c = \frac{1}{4} \frac{1.177(1.2A^{1/3})}{\lambda}$$

and for the fireball

$$\frac{d^2N}{dE_\gamma d\Omega}(A, T) = A \cdot p_c \cdot \frac{d^2N}{dE_\gamma d\Omega}(\bar{\Omega}_S, \bar{\Omega})$$

The T is estimated from fits done to proton data[Ha85c], and is approximated as shown in Table 6.3.

The code HOTSPOT calculates the high energy gamma cross section using these temperatures and an impact parameter

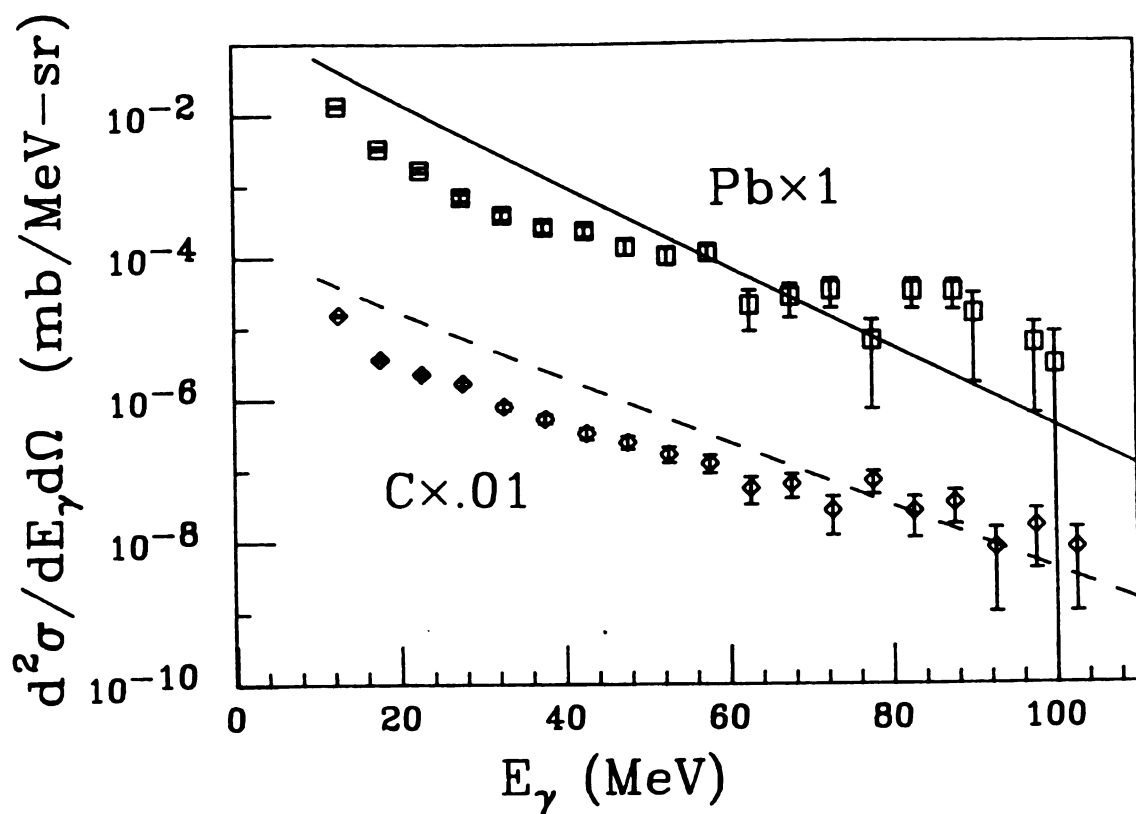


Figure 6.9. Cross section for  $^{14}\text{N}+\text{C}$ , Pb at  $\theta_{\text{Lab}} = 90^\circ$  using the incoherent bremsstrahlung model.

$$d^2\sigma / dE_\gamma d\Omega \quad (\text{mb} / \text{MeV} \text{--sr})$$

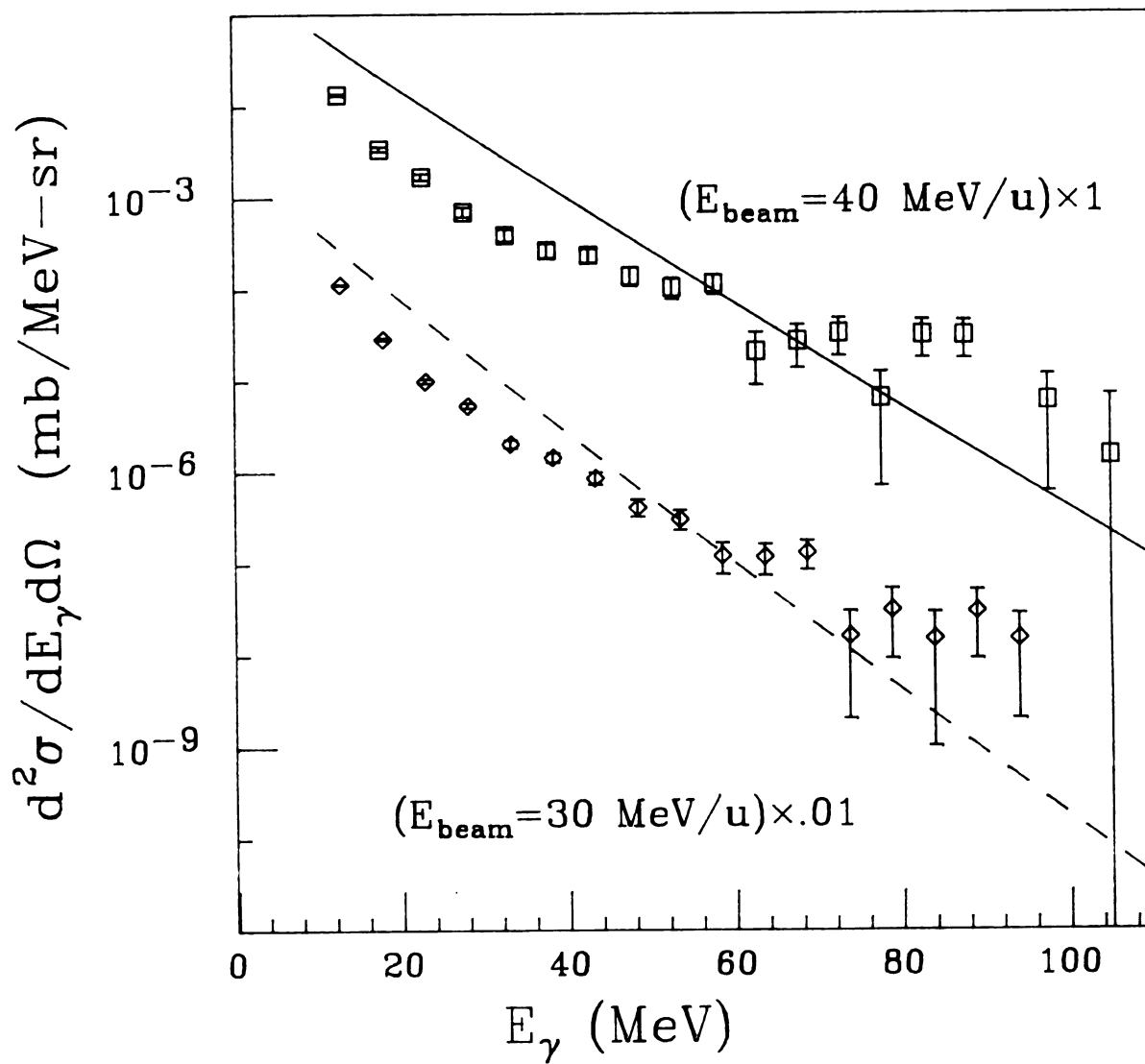


Figure 6.10. Cross section for  $^{14}\text{N}+\text{Pb}$  at 40, 30 MeV/u using the incoherent bremsstrahlung model.

weighted fireball. The results of the calculation and the data are shown in Figure 6.9. The general trend of the high energy component of the data is reproduced, as is the angular distribution, the beam energy dependence, and the target dependence (Figure 6.10).

Similar calculations have been done by Nifenecker and Bondorf[Ni85], where both the coherent part and the incoherent part of the bremsstrahlung are calculated analytically.



## Chapter 7

## Conclusions

The high energy gamma rays discussed in the preceding chapters are an active area of research. Many groups have become involved in measurements and models, and new data and calculations are continually being published.

The first experiment demonstrated the existence of gamma rays of up to 100 MeV in  $^{14}\text{N}+\text{Cu}$  at 40 MeV/u using pair production and a magnetic spectrograph. The second used an entirely different technique, a Cherenkov telescope, and studied three targets, one at two beam energies. Subsequent experiments with other systems and beam energies, indicate that these high energy gamma rays may prove a powerful tool in probing heavy ion collisions, especially at decreasing beam energies where  $\pi^0$  experiments prove very difficult.

Simple calculations, as in the previous chapter, have been used to try to understand this phenomenon. Coherent bremsstrahlung, where the current is provided by the net nuclear motion, fails to produce the nearly isotropic angular distribution measured, but provides roughly the correct photon energy dependence. The thermal model, where the photons are emitted as black body radiation from the

nu

bu

br

ho

an

e:

H

c

r

w

o

e

r

nuclear fireball, provides the isotropic angular dependence, but fails to predict the photon energy dependences.

The incoherent fireball model, in which the photons are bremsstrahlung from nucleus-nucleus collisions within the hot fireball produced in the collisions, gives roughly the angular, beam energy, and photon energy dependence.

This is a region of current interest in intermediate energy heavy ion physics. Theorists W.Bauer, D.Hahn, H.Stöcker, G.Bertsch, J.Aichelin, and W.Greiner are currently working on this problem. R.Shyam and J.Knoll have recently published a paper on the co-operative model, in which both pion and photon production is due to virtual clusters of nucleons pooling their energy[Sh86]. Similar experimental work using a different techniques is in progress at GSI[He84, No85].

In summary, these high energy gamma rays are of great interest in heavy ion reactions, may be closely related to the pions which have been the subject of experiments in recent years, and may prove a valuable probe in intermediate energy collisions.

## Appendix A

## Theoretical Calculations

## A.1 Bremsstrahlung

The current  $\mathbf{J}$  is written as:

$$\mathbf{J}(\mathbf{x}, t) = \beta_1(t)\rho_1(\mathbf{x}, t)c\mathbf{e}_1 - \beta_2(t)\rho_2(\mathbf{x}, t)c\mathbf{e}_2$$

and since  $\mathbf{J} = J\mathbf{e}$ :

$$|\mathbf{n} \times [\mathbf{n} \times \mathbf{J}]| = J \sin\theta_{cm}$$

so the integral becomes:

$$\frac{d^2N}{dE_\gamma d\Omega} = \frac{E_\gamma}{4\pi^2\hbar^3c^3} \left| \int dt \int d^3x [\beta_1\rho_1c - \beta_2\rho_2c] \cdot \right.$$

$$\left. \sin\theta e^{i\omega(t-\mathbf{n}\cdot\mathbf{x}/c)} \right|^2$$

$$\frac{d^2N}{dE_\gamma d\Omega} = \frac{E_\gamma}{4\pi^2\hbar^3c^3} \left| I_1 - I_2 \right|^2 \sin^2\theta_{cm}$$

where

$I_1 =$

and

$I_2 =$

and i

at  $X_2$

so

$I_1 =$

rearr

shape

$I_1 =$

$I_1 =$

The ti

around

is pac

$$I_1 = \int dt \int d^3x c\beta_1(t)\rho_1(\mathbf{x},t) e^{i\omega(t-\mathbf{n}\cdot\mathbf{x}/c)}$$

and

$$I_2 = \int dt \int d^3x c\beta_2(t)\rho_2(\mathbf{x},t) e^{i\omega(t-\mathbf{n}\cdot\mathbf{x}/c)}$$

and if the center of the first nucleus is at  $\mathbf{X}_1$ , the second at  $\mathbf{X}_2$ , then:

$$\mathbf{x} = \mathbf{X}_1(t) + \mathbf{r}_1 = \mathbf{X}_2(t) + \mathbf{r}_2$$

so

$$I_1 = \int dt c\beta_1(t) e^{i\omega t} \\ \times \int d^3x_1 e^{-\mathbf{n}\cdot\mathbf{X}_1(t)/c} \rho_1(\mathbf{X}_1(t)+\mathbf{r}_1) e^{-\mathbf{n}\cdot\mathbf{r}_1/c}$$

rearranging, and assuming that the nucleus does not change shape during the collision:

$$I_1 = \int dt c\beta_1(t) e^{i\omega t} e^{-\mathbf{n}\cdot\mathbf{X}_1(t)} \int d^3x \rho_1(\mathbf{r}_1) e^{-i\omega\mathbf{n}\cdot\mathbf{r}/c}$$

$$I_1 = I_{1\text{time}} \times I_{1\text{space}}$$

The time independent part is the integral over the space around the nucleus:

$$I_{1\text{space}} = \int 2\pi r^2 dr \int d(\cos\theta) \rho_1(r) e^{-i\frac{\omega}{c}r \cos\theta}$$

th

so

I,

Th

ti

no

**X**

I

I

S

I

the charge density is taken to be a uniform sphere:

$$\rho_1(\mathbf{r}) = \frac{Ze}{\frac{4}{3}\pi R_1^3} \quad r < R_1$$

so

$$I_{1\text{space}} = \frac{3Zec^3}{\omega^3 R_1^3} \left\{ \sin \frac{\omega R_1}{c} - \frac{\omega R_1}{c} \cos \frac{\omega R_1}{c} \right\}$$

This result is different by a factor of  $2\pi$  from [Bu82]. The time integral uses the same steps as [Bu82] except allows a nonzero impact parameter  $b$ :

$$\mathbf{x}_1(t) = \frac{b}{2}\hat{x} + Z_1(t)\hat{z}, \quad \mathbf{x}_2(t) = -\frac{b}{2}\hat{x} + Z_2(t)\hat{z}$$

$$I_{1\text{time}} = \int_{-\infty}^{\infty} dt \, c\beta_1(t) e^{i\omega t} e^{-i\omega \mathbf{n} \cdot \mathbf{x}_1(t)/c}$$

$$I_{1\text{time}} = \int dt \, c\beta_1(t) e^{i\omega t} e^{-i\frac{\omega b}{2c} \sin\theta \cos\phi} e^{-i\frac{\omega}{c} Z_1(t) \cos\theta}$$

since the impact parameter does not depend on time,

$$I_{1\text{time}} = e^{-i\frac{\omega b}{2c} \sin\theta \cos\phi} I_{1\text{time}}(x=0)$$

a ti

cross

$\Delta d =$

$\Delta t =$

The c

and t

$\beta_1(t)$

$\beta_1(t)$

using

$Z_1(t)$

$Z_1(t)$

$Z_1(t)$

Breakin

$I_1 < \Delta t$

A point to consider is that the collision is delayed by a time  $\Delta t$  for impact parameter  $b \neq 0$ , since the nuclei must cross an additional distance  $\Delta d$

$$\Delta d = (R_1 + R_2) - \sqrt{(R_1 + R_2)^2 - b^2}$$

$$\Delta t = \frac{\Delta d}{(\beta_{o1} + \beta_{o2})c}$$

The case for impact parameter  $b=0$  is worked out in [Bu82], and the velocity  $\beta_1$  is described by:

$$\beta_1(t) = \beta_{o1} \quad \text{for } t < \Delta t$$

$$\beta_1(t) = \beta_{o1} e^{-(t-\Delta t)/\tau} \quad \text{for } t > \Delta t$$

using this to determine  $Z_1(t)$  and  $Z_2(t)$ :

$$Z_1(t) = -R_1 + \beta_{o1} ct \quad t < \Delta t$$

$$Z_1(t) = -R_1 + \beta_{o1} c \Delta t + \int_{\Delta t}^t \beta_{o1} c e^{-(t-\Delta t)/\tau} dt,$$

$$Z_1(t) = -R_1 + \beta_{o1} c \Delta t + \beta_{o1} c \tau (1 - e^{-(t-\Delta t)/\tau}) \quad t > \Delta t$$

Breaking the time integral into two pieces,

$$I_{\text{time}} = I_{t < \Delta t} + I_{t > \Delta t}$$

$$I_{t < \Delta t} (x=0) = \int_{-\infty}^{\Delta t} dt c \beta_{o1} e^{i\omega t} e^{-i\frac{\omega}{c}(-R_1 + \beta_{o1} ct)} \cos \theta$$

$I_{1t} < \Delta$

$I_{2t} < \Delta$

$I_{2t} < \Delta$

For  $t$

$I_{1t} > \Delta$

$I_{1t} > \Delta t$

$I_{1t} > \Delta t$

where

$x = (t -$

$$I_{1,t < \Delta t}(x=0) = \frac{c\beta_{01} e^{i\frac{\omega}{c}R_1 \cos\theta}}{i\omega(1-\beta_{01} \cos\theta)} e^{i\omega(1-\beta_{01} \cos\theta)\Delta t}$$

$$I_{2,t < \Delta t}(x=0) = \int_{-\infty}^{\Delta t} dt c\beta_{02} e^{i\omega t} e^{-i\frac{\omega}{c}(R_2 - \beta_{02} ct) \cos\theta}$$

$$I_{2,t < \Delta t}(x=0) = \frac{c\beta_{02} e^{-i\frac{\omega}{c}R_2 \cos\theta}}{i\omega(1+\beta_{02} \cos\theta)} e^{i\omega(1+\beta_{02} \cos\theta)\Delta t}$$

For times during the collision

$$I_{1,t > \Delta t}(x=0) = \int_{\Delta t}^{\infty} dt c\beta_{01} e^{-t/\tau} e^{i\omega t} \\ \times e^{-i\frac{\omega}{c}[-R_1 + \beta_{01} c\Delta t + \beta_{01} c\tau(1 - e^{-(t-\Delta t)/\tau})] \cos\theta}$$

$$I_{1,t > \Delta t}(x=0) = \beta_{01} c e^{i\frac{\omega}{c}(R_1 - c\beta_{01}\Delta t) \cos\theta} \\ \times \int_{\Delta t}^{\infty} dt e^{(i\omega\tau - 1)t/\tau} e^{-i\omega\beta_{01}\tau \cos\theta(1 - e^{-(t-\Delta t)/\tau})}$$

$$I_{1,t > \Delta t}(x=0) = \beta_{01} c \tau e^{i\frac{\omega}{c}(R_1 - c\beta_{01}\Delta t) \cos\theta} e^{-a\Delta t/\tau} \\ \times \int_0^{\infty} dx e^{-ax} e^{k(1 - e^{-x})}$$

Where

$$x = (t - \Delta t)/\tau \quad a = 1 - i\omega\tau \quad k = -i\omega\beta_{01}\tau \cos\theta$$

Replacing  $e^{-x}$  with  $v$ ,

$$I_{1t > \Delta t}(x=0) = \beta_{01} c \tau e^{i \frac{\omega}{c} (R_1 - c \beta_{01} \Delta t) \cos \theta} \\ \times e^{-a \Delta t / \tau} e^k \int_0^1 v^{a-1} e^{-k v} dv$$

The integral is the incomplete complex gamma function,

$$I_{1t > 0}(x=0) = \beta_{01} c \tau e^{i \frac{\omega}{c} (R_1 - c \beta_{01} \Delta t) \cos \theta} e^{-a \Delta t / \tau} k^{-a} e^k \Gamma(a, 1)$$

similarly,

$$I_{2t > \Delta t}(x=0) = \int_{\Delta t}^{\infty} dt c \beta_{02} e^{-t/\tau} e^{i \omega t} \\ \times e^{-i \frac{\omega}{c} [R_2 - c \beta_{02} \Delta t - \beta_{02} c \tau (1 - e^{-(t-\Delta t)/\tau})] \cos \theta}$$

$$I_{2t > \Delta t}(x=0) = \beta_{02} c \tau e^{-i \frac{\omega}{c} (R_2 - c \beta_{02} \Delta t) \cos \theta} e^{-a \Delta t / \tau} k^{-a} e^k \\ \times \Gamma(a, 1)$$

Where

$$a = 1 - i \omega \tau \quad k = i \omega \beta_{01} \tau \cos \theta$$

These calculations are found in subroutine BREMANYB, listed in Appendix D.

fram

angle

in th

where

the

foun

The

fram

so t

$\frac{d\sigma^2}{dE}$   
YL

The calculation of the cross section in the laboratory frame is straight forward (program BREMIW). First, the angle in the laboratory frame is transformed into an angle in the center-of-mass frame:

$$\tan\theta_{\text{cm}} = \frac{\sin\theta_L}{\gamma(\cos\theta_L - \beta)}$$

where  $\beta, \gamma$  refer to the nucleus-nucleus system relative to the laboratory frame. The ratio of the solid angles can be found:

$$d\theta_{\text{cm}} = \frac{(1 - \beta\cos\theta_L)}{\gamma(\cos\theta_L - \beta)^2} \cos^2\theta_{\text{cm}} d\theta_L$$

The relation between the photon energy in the laboratory frame and the center-of-mass frame is:

$$E_{\gamma\text{cm}} = E_{\gamma\text{L}} \gamma(1 - \beta\cos\theta_L)$$

so the cross section in the laboratory frame is just

$$\frac{d\sigma^2}{dE_{\gamma\text{L}} d\Omega_{\text{L}}} (E_{\gamma\text{L}}, \theta_{\text{L}}) = \int_0^{b_{\infty}} \int_0^{2\pi} b_{\infty} db_{\infty} \frac{d^2N}{dE_{\gamma\text{cm}} d\Omega_{\text{cm}}} (E_{\gamma\text{cm}}, \phi)$$

## A.2 Hard Sphere Bremsstrahlung

The center-of-mass scattering angle of the nuclei is related to the impact parameter  $b$  by:

$$\theta_s = \pi - 2 \operatorname{Asin}\left[\frac{b}{R_1 + R_2}\right]$$

where  $R_1$  and  $R_2$  are the radii of the nuclei.

The only change in the evaluation of the previous calculation is a change in the time integral after the collision, and in the value of the quantity  $[\mathbf{n} \times (\mathbf{n} \times \mathbf{J})]$  which becomes:

$$|[\mathbf{n} \times (\mathbf{n} \times \mathbf{J})]|^2 = \sin^2(\theta - \theta_s) + \sin^2\theta \sin^2\theta_s \sin^2\phi + \\ 2(1 - \cos\phi) \sin\theta \cos\theta \sin\theta_s \cos\theta_s$$

After the collision, the position becomes

$$\mathbf{x}_1(t) = \mathbf{x}\left[\frac{b}{2} + c\beta_1 \sin\theta_s\right] + \mathbf{z}\left[-R_1 + c\beta_1 \Delta t + c\beta_1 \cos\theta_s (t - \Delta t)\right]$$

the time integral becomes:

$$I_{\text{time}} = \frac{-\beta_1}{i\omega(1-\beta_1 q)} e^{-i\omega g_1} e^{i\frac{\omega}{c}(1-\beta_1 q)\Delta t}$$

with

$$g_1 = \frac{b}{2} \sin\theta_s \cos\phi + \cos\theta (-R_1 + c\beta_1(1 - \cos\theta_s)\Delta t)$$

and

$$q = \sin\theta \cos\phi \sin\theta_s + \cos\theta \cos\theta_s$$

and

$$I_{2\text{time}} = \frac{-\beta_2}{i\omega(1+\beta_2q)} e^{-i\omega g_2} e^{i\omega(1+\beta_2q)\Delta t}$$

with

$$g_2 = -\frac{b}{2} \sin\theta \cos\phi + \cos\theta (R_2 - \beta_2 (1 - \cos\theta_s)) \Delta t$$

A.3

ea

of

co

R<sub>1</sub>

vo

a

r

d

v

### A.3 Fireball

The overlap of the two spherical nuclei passing through each other is equivalent to the intersection of a cylinder of radius  $R_2$ , intersecting a sphere of radius  $R_1$ , for the contribution of the first nucleus, and a cylinder of radius  $R_1$ , intersecting a sphere of radius  $R_2$ , for the second. The volume intersected is (function OVERLAP):

$$V_{HS} = \int_{-R_1}^{+R_1} \text{Area}(R_2, r_1) dz, \quad \text{where } r_1 = \sqrt{R_1^2 - z^2}$$

and  $\text{Area}(R_2, r_1, d)$  is the area of intersection of circular regions of radii  $R_2$  and  $r_1$ , whose centers are separated by distance (impact parameter)  $d$  (function AREA)

$$R_L = \text{larger of } R_2, r_1 \text{ and } R_S = \text{smaller of } R_2 \text{ and } r_1$$

$$w = \frac{R_S^2 + d^2 - R_L^2}{2R_S d}$$

$$\text{if } w \leq -1 \quad \text{Area} = 0$$

$$\text{if } w \geq +1 \quad \text{Area} = \pi R_S^2$$

$$\text{if } -1 \leq w \leq +1 \quad \theta = \text{Acos}(w)$$

$$\alpha = \text{Asin}\left[\frac{R_S \sin(\theta)}{R_L}\right]$$

The

The

co

par

(Ta

wi

So

Tn

A

$$\text{Area} = R_S^2 \left[ \theta - \frac{\sin(\theta)}{2} \right] + R_L^2 \left[ \alpha - \frac{\sin(\alpha)}{2} \right]$$

The number of nucleons from nucleus #1 is

$$A_{1HS} = \frac{V_{1HS}}{\frac{4}{3}\pi R_1^3} A_1$$

The temperature is found by assuming all the thermal energy comes from the kinetic energy per nucleon of the participants in the center-of-mass frame of the fireball (Table 6.2):

$$T = \frac{A_{1HS} \cdot T_{1cm} + A_{2HS} \cdot T_{2cm}}{A_{1HS} + A_{2HS}}$$

In a black body of temperature  $T$ , the energy density with angular frequency  $\omega$  is [Be70]:

$$u(\omega) = \frac{1}{\pi^2 c^3} \frac{\hbar \omega^3}{e^{\hbar \omega / T} - 1} d\omega$$

So the number of photons in volume  $V$  is

$$dN = \frac{u(\omega)}{\hbar \omega} \cdot V_0 = \left[ \frac{\hbar \omega}{\hbar c} \right]^2 \frac{1}{\pi^2 \hbar c} \frac{V}{e^{\hbar \omega / T} - 1} d(\hbar \omega)$$

The hotspot is taken to be normal nuclear density containing  $A$  nucleons, so

$$V = \frac{4}{3}\pi R^3, \quad R = r_0^3 \cdot A^{1/3}, \quad r_0 = 1.2 \text{ fm}$$

Allowing all the photons to leave isotropically,

$$\frac{d^2N}{dE_\gamma d\Omega} = \frac{1}{3\pi^2\hbar c} \left[ \frac{\hbar\omega}{\hbar c} \right] \frac{r_0^3 A}{e^{\hbar\omega/T} - 1}$$

#### A.4 Incoherent Fireball Bremsstrahlung

To estimate the yield of nucleon-nucleon bremsstrahlung within the fireball, consider a fireball of temperature  $T$  and  $A$  nucleons. Assuming the energies of the nucleons in the fireball to have a Boltzmann distribution of velocity  $u$ :

$$f(\mathbf{u})d^3\mathbf{u} = \left(\frac{m}{2\pi T}\right)^{3/2} e^{-\frac{m\mathbf{u}^2}{2T}} d^3\mathbf{u}$$

The energy of one nucleon in the center of mass of the nucleon-nucleon collision is:

$$\epsilon = \frac{m}{2} \left(\frac{\mathbf{u}_1 - \mathbf{u}_2}{2}\right)^2 = \frac{m}{8}(\mathbf{u}_1 - \mathbf{u}_2)^2$$

so

$$\mathbf{u}_1 = \mathbf{u}_2 + \sqrt{8\epsilon/m} \mathbf{n}$$

$$\begin{aligned} P(\epsilon) &= \left(\frac{m}{2\pi T}\right)^3 \int e^{-\frac{m\mathbf{u}^2}{2T}} e^{-\frac{m}{2T}(\mathbf{u} + \sqrt{8\epsilon/m} \mathbf{n})^2} d^3\mathbf{u} \\ &= \left(\frac{m}{2\pi T}\right)^3 2\pi \int e^{-\frac{m\mathbf{u}^2}{2T}} e^{-\frac{m\mathbf{u}^2}{2T}} e^{-\frac{4\epsilon}{T}} e^{-\frac{m\mathbf{u}\sqrt{8\epsilon/m}}{T}\cos\theta} u^2 du d\cos\theta \end{aligned}$$

$$= \left(\frac{m}{2\pi T}\right)^3 \frac{2\pi}{-\frac{m}{T} \sqrt{8\epsilon/m}} \int e^{-\frac{mu^2}{T}} e^{-\frac{4\epsilon}{T}} \cdot$$

$$\left[ e^{-\frac{mu}{2T} \sqrt{8\epsilon/m}} - e^{+\frac{mu}{2T} \sqrt{8\epsilon/m}} \right] u^2 du$$

$$= \left(\frac{m}{2\pi T}\right)^3 \frac{4\pi T}{\sqrt{8\epsilon m}} e^{-4\epsilon/T} \left\{ \int e^{-\frac{m}{T}(u^2 - u\sqrt{2\epsilon/m})} u^2 du - \right.$$

$$\left. \int e^{-\frac{m}{T}(u^2 + u\sqrt{2\epsilon/m})} u^2 du \right\}$$

completing the square in the exponent,

$$= \left(\frac{m}{2\pi T}\right)^3 \frac{4\pi T}{\sqrt{8\epsilon m}} e^{-4\epsilon/T} e^{+\frac{\epsilon}{2T}} \left\{ \int e^{-\frac{m}{T}(u^2 - \frac{1}{2}\sqrt{2\epsilon/m})^2} u^2 du - \right.$$

$$\left. \int e^{-\frac{m}{T}(u^2 + \frac{1}{2}\sqrt{2\epsilon/m})^2} u^2 du \right\}$$

Taking

$$\zeta = \sqrt{\epsilon/(2m)}$$

$$P(\epsilon) = \frac{m}{8\pi^2 T^2 \zeta} e^{-2\epsilon/T} \left\{ \int_{-\zeta}^{\infty} e^{-\frac{m}{T}y^2} (y+\zeta)^2 dy - \int_{\zeta}^{\infty} e^{-\frac{m}{T}y^2} (y-\zeta)^2 dy \right\}$$

$$= \frac{m}{8\pi^2 T^2 \zeta} e^{-2\epsilon/T} \left\{ \int_{-\zeta}^{\zeta} e^{-\frac{m}{T} y^2} y^2 dy - 2\zeta \int_{-\zeta}^{\zeta} e^{-\frac{m}{T} y^2} y dy \right. \\ \left. + \zeta^2 \int_{-\zeta}^{\zeta} e^{-\frac{m}{T} y^2} dy \right\}$$

the unnormalized distribution is

$$P(\epsilon) = \frac{m}{8\pi^2 T^2 \zeta} e^{-2\epsilon/T} \left\{ \left(\frac{T}{m}\right)^{3/2} \left[ \sqrt{\frac{2}{\pi}} \operatorname{erf}(\zeta) - \zeta e^{-\zeta^2} \right] \right. \\ \left. + \zeta^2 \left(\frac{T}{m}\right)^{1/2} \left[ \sqrt{\frac{4}{\pi}} \operatorname{erf}(\zeta) \right] \right\}$$

For the case of interest,  $\epsilon \ll m$ :

$$\zeta \ll 1, \operatorname{erf}(\zeta) = \zeta = \sqrt{\epsilon/(2m)}$$

and normalizing so that  $\int P(\epsilon) d\epsilon = 1$

$$P(\epsilon) = \frac{1}{2\left(\sqrt{\frac{3}{\pi}} - 1\right)T} e^{-2\epsilon/T} \left\{ \left[\sqrt{\frac{2}{\pi}} - 1\right] + \frac{\epsilon}{T} \left[\sqrt{\frac{2}{\pi}}\right] \right\}$$

hence

$$\langle \epsilon \rangle = \frac{\int \epsilon P(\epsilon) d\epsilon}{\int P(\epsilon) d\epsilon} = T/2$$

For a collision between two nucleons, the scattering can be approximated as being isotropic scattering of point like particles since the nucleons are much smaller than the wavelengths of interest.

The bremsstrahlung is given by

$$\frac{dN^2}{dE_\gamma d\Omega} = \frac{E_\gamma}{4\pi(\hbar c)^3} \left| \int dt \int d^3x \mathbf{n} \times [\mathbf{n} \times \mathbf{J}(\mathbf{x}, t)] e^{i\omega(t - \mathbf{n} \cdot \mathbf{x}/c)} \right|^2$$

For time less than 0,

$$J_1 = Z_1 \beta c z \quad J_2 = -Z_2 \beta c z$$

where

$$\beta = \frac{\sqrt{2m\epsilon + \epsilon^2}}{m + \epsilon}$$

and for time greater than 0,

$$J_1 = Z_1 \beta c (\sin\theta_s x + \cos\theta_s z) \quad J_2 = -Z_2 \beta c (\sin\theta_s x + \cos\theta_s z)$$

The integral over space becomes

$$I_{\text{space}} = \frac{3e}{\left(\frac{\omega R_\rho}{c}\right)^3} \left( \sin \frac{\omega R_\rho}{c} - \frac{\omega R_\rho}{c} \cos \frac{\omega R_\rho}{c} \right)$$

and for high photon energies  $\frac{\omega R_\rho}{c} < 1$

$$(I_{\text{space}})^2 \approx e^2$$

and the time integral becomes

$$I_{1\text{time}} = \mathbf{n} \times (\mathbf{n} \times \mathbf{z}) \beta c \left( \frac{Z_1}{i\omega - i\frac{\omega}{c} \beta \mathbf{n} \cdot \mathbf{z}} \right) - \mathbf{n} \times (\mathbf{n} \times \mathbf{s}) \beta c \left( \frac{Z_2}{i\omega - i\frac{\omega}{c} \beta \mathbf{n} \cdot \mathbf{s}} \right)$$

$$I_{2\text{time}} = -\mathbf{n} \times (\mathbf{n} \times \mathbf{z}) \beta c \left( \frac{Z_1}{i\omega + i\frac{\omega}{c} \beta \mathbf{n} \cdot \mathbf{z}} \right) + \mathbf{n} \times (\mathbf{n} \times \mathbf{s}) \beta c \left( \frac{Z_2}{i\omega + i\frac{\omega}{c} \beta \mathbf{n} \cdot \mathbf{s}} \right)$$

where  $\mathbf{s}$  is the direction of the scattered nucleon,

$$\mathbf{s} = \mathbf{x} \sin \theta_s + \mathbf{z} \cos \theta_s$$

Since  $\beta \ll 1$ , we drop the impact parameter term,

$$I_{\text{time}} = \frac{\beta c}{i\omega} [\mathbf{n} \times (\mathbf{n} \times \mathbf{z})] \left( \frac{Z_1 e}{1 - \beta \mathbf{n} \cdot \mathbf{z}} - \frac{Z_2 e}{1 - \beta \mathbf{n} \cdot \mathbf{z}} \right) \\ - \frac{\beta c}{i\omega} [\mathbf{n} \times (\mathbf{n} \times \mathbf{s})] \left( \frac{Z_1 e}{1 - \beta \mathbf{n} \cdot \mathbf{s}} - \frac{Z_2 e}{1 - \beta \mathbf{n} \cdot \mathbf{s}} \right)$$

And keeping only the lowest order terms in  $\beta$  since  $\beta \ll 1$ ,

$$I_{\text{time}} = \frac{\beta c}{i\omega} (Z_1 - Z_2) ([\mathbf{n} \times (\mathbf{n} \times \mathbf{z})] - [\mathbf{n} \times (\mathbf{n} \times \mathbf{s})])$$

$$\left| I_{\text{time}} \right|^2 = \frac{\beta^2 c^2 (Z_1 - Z_2)^2}{\omega^2} (|\mathbf{n} \times (\mathbf{n} \times \mathbf{z})|^2 + |\mathbf{n} \times (\mathbf{n} \times \mathbf{s})|^2 \\ - 2\mathbf{n} \times (\mathbf{n} \times \mathbf{z}) \cdot \mathbf{n} \times (\mathbf{n} \times \mathbf{s}))$$

Averaging over  $\Omega_s$  and  $\Omega$ ,

$$\left| I_{\text{time}} \right|^2 = \frac{\beta^2 c^2 (Z_1 - Z_2)^2}{\omega^2} \cdot \frac{4}{3} \frac{1}{4\pi}$$

To order  $\beta^2$ , only n-p collisions contribute to bremsstrahlung. The scattering angle and emission angle averaged photon production from an n-p collision of energy  $\epsilon$  is:

$$\frac{d^2 N}{dE_\gamma d\Omega} (\overline{\Omega_s, \Omega}) \approx \frac{E_\gamma}{4\pi(\hbar c)^3} e^2 \frac{4\beta^2 c^2}{3\pi\omega^2} = \frac{e^2 \epsilon}{3\pi^2(\hbar c)E_\gamma m c^2}$$

and averaging this yield for all collisions of energy  $\epsilon \geq \hbar\omega$

$$\frac{d^2 N}{dE_\gamma d\Omega} (\overline{\epsilon}) = \frac{e^2 T}{3\pi^2 \hbar c E_\gamma m c^2} \left[ \frac{1}{\sqrt{\pi} - 1} \right]$$

$$\cdot \left\{ \left( \frac{1}{\sqrt{\pi}} - \frac{1}{4} \right) + \left( \frac{2}{\sqrt{\pi}} - \frac{1}{2} \right) \left[ \frac{E_\gamma}{T} \right] + \left( \frac{1}{\sqrt{\pi}} \right) \left[ \frac{E_\gamma}{T} \right]^2 \right\} e^{-2E_\gamma/T}$$

## Appendix B

## Experimental Hardware

**B.1 The Enge Split-Pole Spectrograph**

The Enge split-pole magnetic spectrograph is a high resolution device designed to study discrete states in nuclear systems[Sp67]. At NSCL it is sometimes referred to as the S-120, since the maximum mass energy product ( $AE/q^2$ ) this spectrograph can measure is 120 MeV (Table B.1). It has a single field winding, two sets of pole tips, no quadrupoles, and accomplishes focusing by means of the edges of the two poles (Figure B.1). Kinematic corrections are made by moving the focal plane according to instructions from the code SPECKINEX[Be80].

**3.1.1 General Relationships**

Particle rigidity  $B\rho$  (in Kgauss-inches) is related to the momentum  $P$  (in MeV/c) by:

$$B\rho = \frac{1.3132465 P}{Q}$$

Table B.1 General Specifications of the Enge Spectrograph

radius of curvature $\rho$ :	$16.023 \leq \rho \leq 43.407$ inch
maximum magnetic field:	$B = 17.5$ Kgauss
Dispersion:	$1.8 \text{ cm}/1\% \left(\frac{\Delta P}{P}\right)$
horizontal magnification:	.34
vertical magnification:	3
solid angle:	4.8 msr

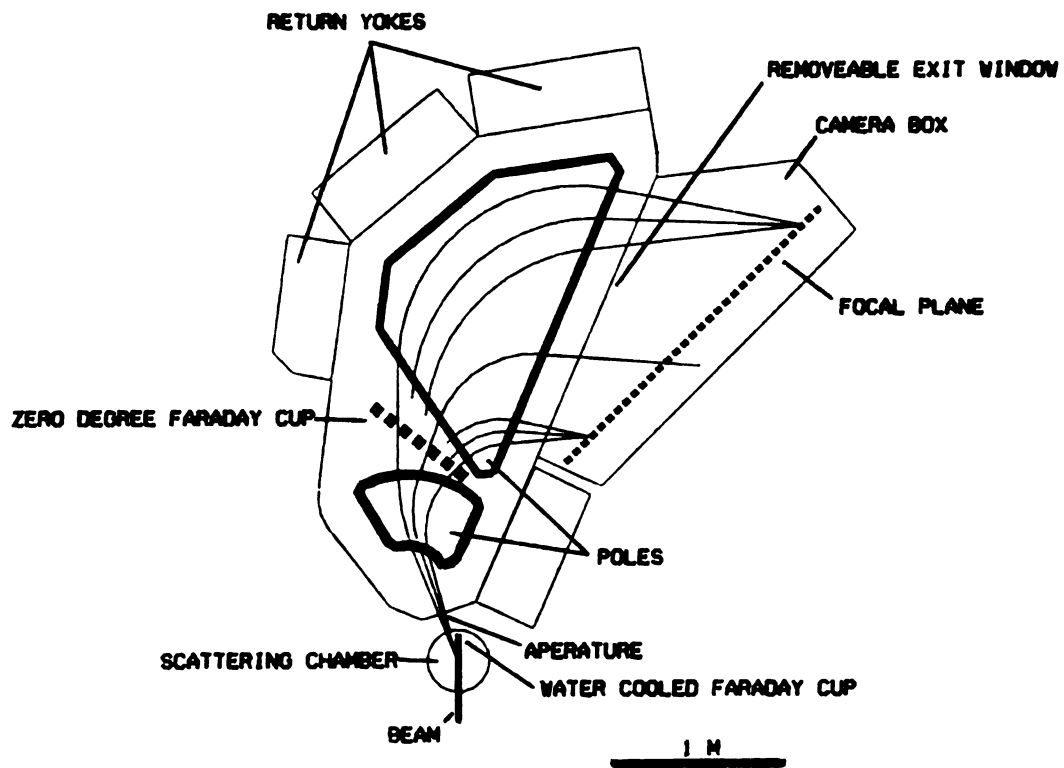


Figure B.1. The Enge split-pole magnetic spectrograph.

The path length through the Enge from the target to the focal plane is approximately:

$$L = 4.745 \rho$$

and the relationship between the NMR probe frequency  $F$  (in MHz) and the magnetic field  $B$  (in Kgauss) is:

$$F = 4.2577 B$$

The approximate empirical relation between the potentiometer setting on the magnetic power supply and the final NMR frequency reading is:

$$\text{pot} = -.9025 + 11.476 F + 4.9023 \times 10^{-10} F^6 - 1.9262 \times 10^{-13} F^8 \\ + 4.5274 \times 10^{-17} F^{10} \quad \text{with } 0 \leq \text{pot} \leq 999.99$$

With no kinematic corrections the relationship between the radius of curvature  $\rho$  and the focal plane position  $DX$  is:

$$DX = 89.557 - 2.48306 \rho$$

The median plane of the focus of the spectrograph is approximately 4.5" above the detector mounting plate.

**B.1.2 Nonrelativistic Kinematic Corrections**

For the reaction  $m_2 + m_1 \rightarrow m_4 + m_3$

where  $m_1$  target  
 $m_2$  beam  
 $m_3$  product  
 $m_4$  residual nucleus

$\theta_L$  = laboratory angle

$$Tx = \sqrt{T_{\text{beam}}/T_{\text{product}}} \quad \rho \sqrt{\frac{m_1 m_3}{m_4}}$$

$$Bk = 1 + \frac{m_3}{m_4}$$

the positions of the two pivot points of the focal plane are changed to accomplish kinematic corrections according to:

$$DS = \frac{.34 \cdot 1.77 \cdot Tx \cdot \sin \theta_L}{(Bk - \frac{Tx \cdot \cos \theta_L}{\rho})} + 2.79$$

$$DL = \frac{.34 \cdot 1.77 \cdot Tx \cdot \sin \theta_L}{(Bk - \frac{Tx \cdot \cos \theta_L}{\rho})} + 2.69$$

$$G = \sqrt{\frac{1024 + (31.7 + DS - DL)^2}{2050.882}}$$

The relationship between radius of curvature  $\rho$  and the focal plane position  $DX$  is:

$$DX = G (89.90556 - 2.49258\rho)$$

For the  $\pi^\pm$  and  $e^\pm$  experiments, there were no kinematic corrections:

$$\theta_L \rightarrow 0 \quad \frac{m_3}{m_4} \rightarrow 0$$

hence:

$$Bk \rightarrow 1 \quad Tx \rightarrow 0 \quad G \rightarrow .99618$$

and the focal plane positions become:

$$DS \rightarrow 2.79$$

$$DL \rightarrow 2.69$$

and

$$DX = 89.557 - 2.48306 \rho$$

The MIW counter's active area was near the center of the focal plane:

$$16.025" \leq DX_{MIW} \leq 35.025"$$

which corresponds to:

$$22.12" \leq \rho_{MIW} \leq 29.77"$$

### B.1.3 Exit Window

The very large range of the particles of interest meant that the camera box of the Enge did not need to be evacuated. This simplified the detector design, but required the construction of a large window of .003" Kapton and of a frame to fit in the between the camera box and the dipole. This removable window extends the entire length and height of the dipole exit. About half the bolts holding the camera box to the dipole around the exit were removed, the window and frame inserted, and longer bolts with brackets to compress the O-ring inserted. The remaining original bolts should not be removed; they hold the camera box onto the dipole. In addition, the upper right hand bolt hole provided a large leak between the camera box and dipole, so that bolt was epoxied in place.

### B.1.4 New Scattering Chamber and Aperture

The  $\pi^\pm$  experiment required a thicker aperture than could be placed in the aperture holder, so a 4.8 mstr copper aperture .8" thick was fabricated and placed in the sliding seal of the target chamber.

The  $e^\pm$  experiment required that the aperture holder and the target chamber be removed. Because of the long range and multiple scattering of the  $e^\pm$ , the existing apertures and holder could not be used. The entire mechanism was removed and a .003" Kapton window placed across the opening

of the spectrograph. The detector was used to determine the solid angle.

The scattering chamber was replaced by a much smaller chamber with thinner walls. A .003" Kapton window covered the exit side of the chamber, leaving about a 7" air gap between the chamber and the dipole entrance, and removed the need to design and construct a sliding seal between the scattering chamber and spectrograph. The original target ladder and mechanism was retained, but was insulated from ground so that the target/converter could be used as the Faraday cup. As beam was expected to produce as much as 7 Watts of heat, which might melt the nylon screws holding the target ladder to the shaft, a copper block cooled by nitrogen gas was attached to the target ladder.

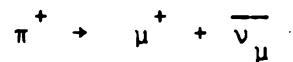
## B.2 General Design of the $\pi^\pm$ experiment

The original  $\pi^\pm$  experimental configuration is shown in Figure B.2. The beam enters the 14" scattering chamber, passes through the target in the center of the chamber, and stops in water inside the the water-cooled Faraday cup. A pion of the correct charge and momentum range passes through the aperture, is bent by the dipole, passes through the exit window, air, MIW proportional chamber, and the  $\Delta E$  scintillator to stop in the E scintillator.

Having the camera box filled with air has several advantages; the detector can be partially outside than the camera box in order to cope with the pion's large range, and the PCOS electronics can be air cooled.

The position of the particle as it crosses the focal plane, measured by the MIW, determines its momentum. The  $\Delta E$  scintillator measures the energy loss, and the E scintillator the remaining energy. Since  $\pi^\pm$  are strongly interacting particles with a lifetime of 26 nS, particle identification is somewhat more complicated than the example in Chapter 2.

For  $\pi^+$ , the decay:



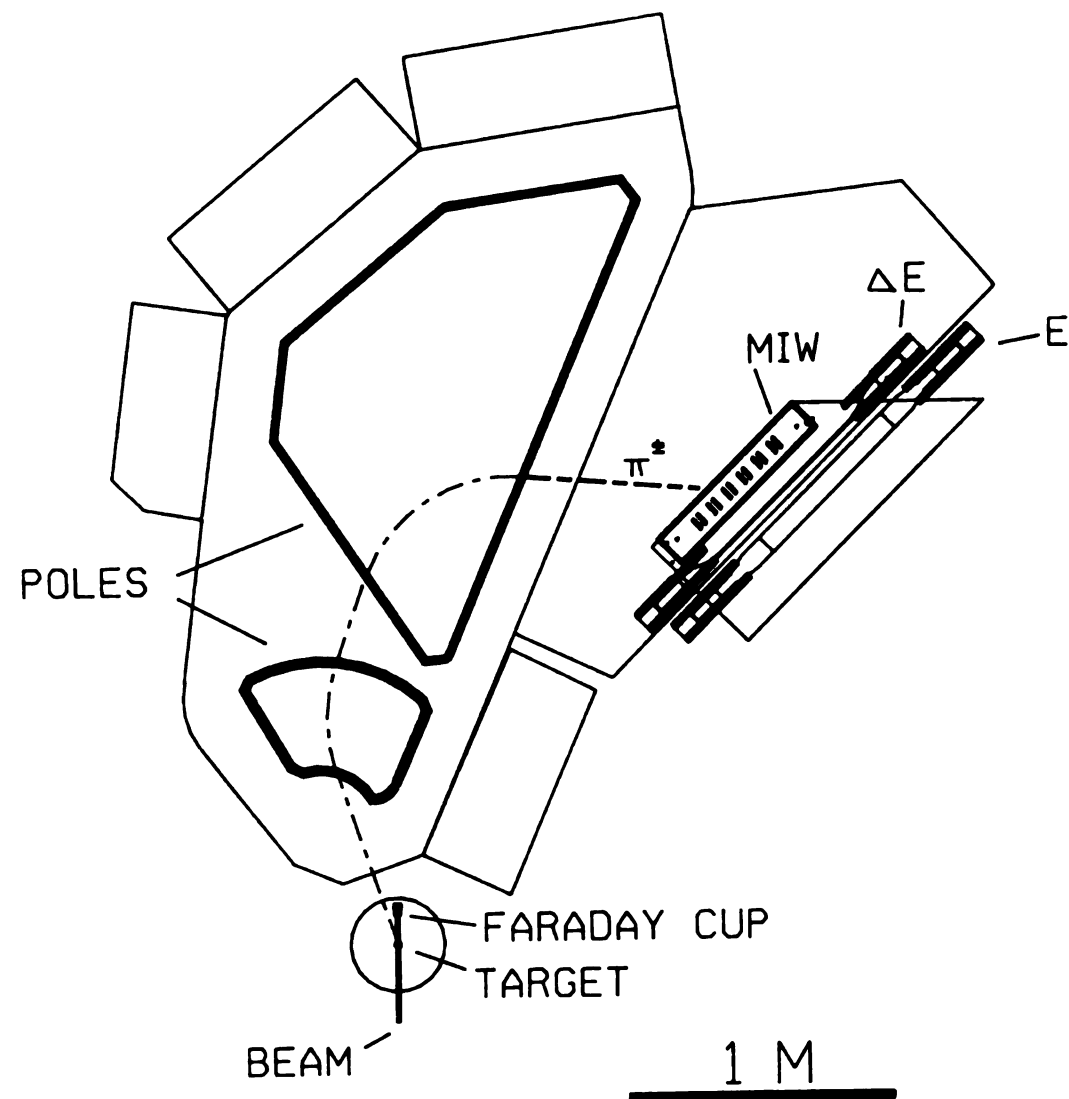


Figure B.2. The  $\pi^\pm$  experimental configuration.

provides a  $\mu^+$  of kinetic energy:

$$T_{\mu} = \frac{(m_{\pi}^2 - m_{\mu}^2)^2}{2m_{\pi}} = 4.1 \text{ MeV}$$

The short range of this  $\mu^+$  means that all its kinetic energy is given to the scintillator in a time comparable to the resolution of the electronics, and just serves to increase the E scintillator signal slightly. The subsequent decay of the  $\mu^+$ :

$$\mu^+ \rightarrow e^+ + \bar{\nu}_e + \nu_{\mu}$$

takes place with a lifetime (2.2  $\mu$ S) which is much longer than the resolution of the electronics, and rarely contributes to the E signal.

As the  $\pi^-$  slows in matter, it becomes increasingly probable that the  $\pi^-$  will become bound to a nucleus via the Coulomb force like an electron. The  $\pi^-$  is about 273 times heavier than an electron, and the orbital is correspondingly smaller, allowing the  $\pi^-$  wavefunction to overlap the nucleus. The  $\pi^-$  is a strongly interacting particle, and is quickly absorbed, giving the nucleus an excitation equal to the  $\pi^-$  rest mass (140 MeV). De-excitation is mainly by particle emission. This "pion star" can increase the apparent E signal by 0-140 MeV depending on the charge distribution of the emitted particles, hampering particle identification. Particle identification is not

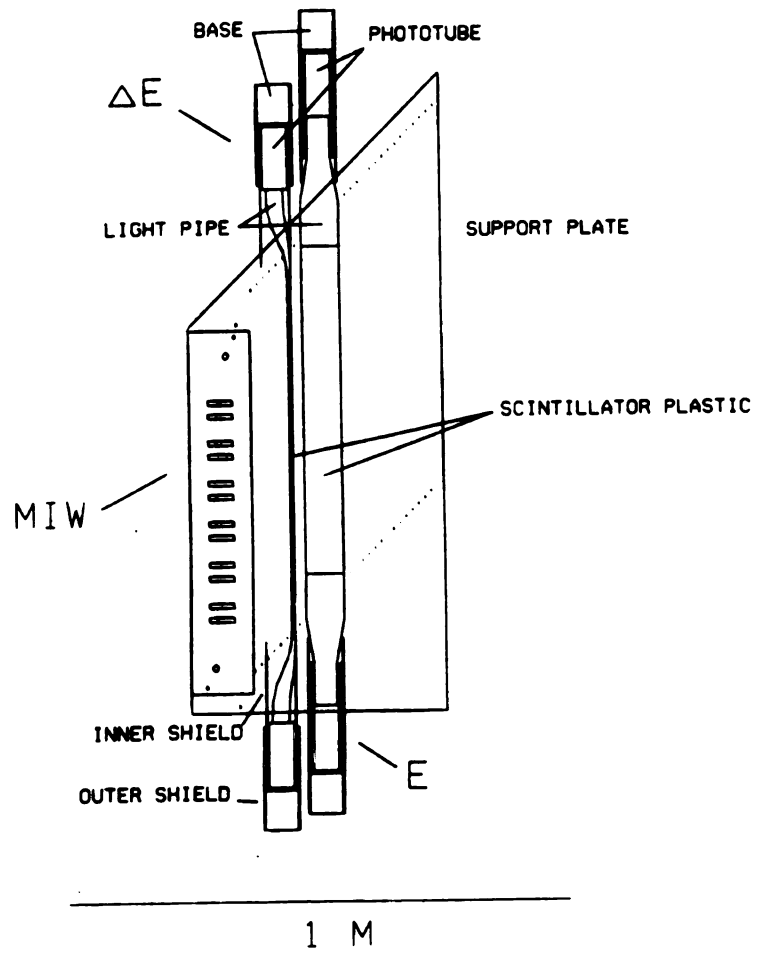


Figure B.3. The  $\pi^\pm$  experiment detector.

significantly impeded since only negative particles likely to reach the focal plane are electrons. Electrons are easily distinguished from the  $\pi^-$ .

In this experiment, the goal was to measure and identify pions with energies of 20-100 MeV. The first scintillator was designed so that the energy loss of a 20 MeV pion traveling  $45^\circ$  to the counter's axis is about 5 MeV (Figure B.3). The size of the E scintillator was determined by the difference in stopping depths of 100 MeV pions with  $36^\circ$  and  $54^\circ$  angles with respect to the counter, corresponding to the maximum solid angle of the spectrograph. An aluminum wedge is placed between the MIW position sensitive detector and the  $\Delta E$  scintillator for runs with pions of energy greater than 40 MeV. The wedge is made such that it slows the pion so that it stops in the E scintillator. Details on the construction of the detector are in Appendix C.

Test runs using the zero degree Faraday cup demonstrated a large background in the scintillators. In an effort to minimize the background a new E scintillator 1" thick was used. This thickness corresponds to the difference in stopping depth for 40 MeV pions entering at  $36^\circ$  and  $54^\circ$ . A wedge was made for this configuration, shown in Figure 2.4. This configuration was designed to operate exclusively for pions of 20-36 MeV.

Further tests indicated the presence of very high energy  $e^\pm$  ( $T_e \sim 100$  MeV) at the detector (Chapter 2), so a

24"x2"x1" plexiglas UVT Cherenkov detector was placed behind the E scintillator (Figure 2.5), and measurements were taken over a wide range of  $e^+$  and  $e^-$  energies. Comparison of the target in and out data indicated that most of the  $e^\pm$ 's were produced by high energy photons from the Faraday cup pair converting to high energy  $e^+e^-$  pairs at the spectrograph aperture.

### B.3 Experimental Electronics

All the information from the detector appears as electronic pulses of short duration; typically 10-100 ns. The conversion of these analog pulses into digital information suitable for storage on magnetic tape by a VAX-750 computer is handled by the electronics, which is divided into three parts: NIM, CAMAC, and PCOS. While PCOS III system is specialized and is discussed in detail in Appendix B.4, the other systems consist of standardized modules easily arranged to suit an individual experiment.

The NIM electronics are analog and logical devices which draw only their power from the standardized NIM crate in which they reside. These include amplifiers, discriminators, gate and delay generators, and coincidence modules. The logical condition specifying an "event" is determined by the NIM logic modules.

The CAMAC system takes pulses from the NIM electronics when it receives an event strobe, and converts these pulses into numbers. The CAMAC modules are under the control of the LSI acquisition system, a Large Scale Integrated PDP 11/23 computer. The CAMAC crate provides support, power, and a communication bus to each module. The CAMAC modules include Analog to Digital Converters (ADC), Time to Digital Converters (TDC), charge (Q) to Digital Converters (QDC),

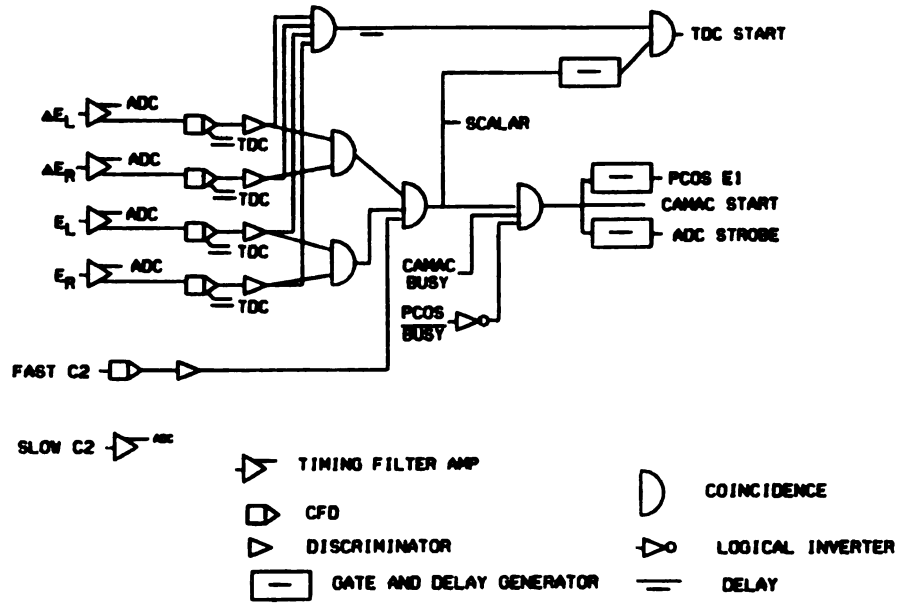


Figure B.4. The  $\pi^+$  experiment electronics.

and scalars. In addition, a module called the a databus allows the PCOS information to be read into the LSI.

The program SARA [Sh85] samples the information gathered by the LSI and performs analysis while the LSI is running, allowing continuous monitoring of the experiment.

### B.3.1 The $\pi^{\pm}$ Experiment Electronics

While the electronic setup was modified many times throughout the development of the experiment, the initial scheme was straight forward. This setup is shown schematically in Figure B.4 and used Timing Filter Amplifiers (TFA) to amplify the direct anode pulses from the photomultiplier tubes. The TFAs proved very nonlinear with such fast pulses.

The TFAs provided signals to both an ADC and to a Constant Fraction Discriminator (CFD). The CFD provides a logic pulse, the timing of which is independent of the pulse height. This pulse is delayed and used to stop the TDC as well as being used in the coincidence logic.

The TFAs were later replaced by fast amplifiers. The dynode of the photomultiplier was connected to a preamp, which shaped and stretched the pulse. A slow amplifier was used to send the pulse to the ADC. The anode pulse went to a fast amplifier, which in turn fed a CFD, providing the signal for the logic and timing circuits.

The coincidence gate, defining when an event of interest had occurred, was varied to reflect the

experimental configuration. In Figure B.4, the requirement is  $\Delta E + E + \overline{BUSY}$ , whereas later it was made  $\Delta E + E + C_2 + \overline{BUSY}$ . The signal  $\overline{BUSY}$  is provided by the LSI and means that the computer is not busy. The signal  $C_2$  is taken from the secondary cathode of the MIW chamber; it is generated later than the photomultiplier signals due to the electron drift time within the MIW. The drift time was measured using a Time to Amplitude Converter (TAC). The start for the TAC was the  $\Delta E + E$  coincidence; the stop was the MIW (primary cathode)  $C_1$  pulse. The output was proportional to the time between them and was put into an ADC channel.

The use of the  $C_2$  signal in the gate suppresses spurious events due to  $(n,p)$ ,  $(n,n')$ , and  $(\gamma,\gamma')$  background by about a factor of 40. The fact that the  $C_2$  signal may be delayed from 0 to -300 ns required the using a wide gate, delaying the scintillator signals, and using the maximum internal delay of the PCOS system (682.5 ns). The coincidence output goes to Gate and Delay Generators (GDG), which provide adjustable width pulses for the ADCs and for the PCOS E1 gate.

The widths of the inputs to the coincidence gate were made wider than the RF period of the cyclotron (~50 ns). This allows an event to be defined even if the pulses from the counters were made by particles from different beam pulses. This provides a way of determining the random coincidence rate. The information from the TDCs determines

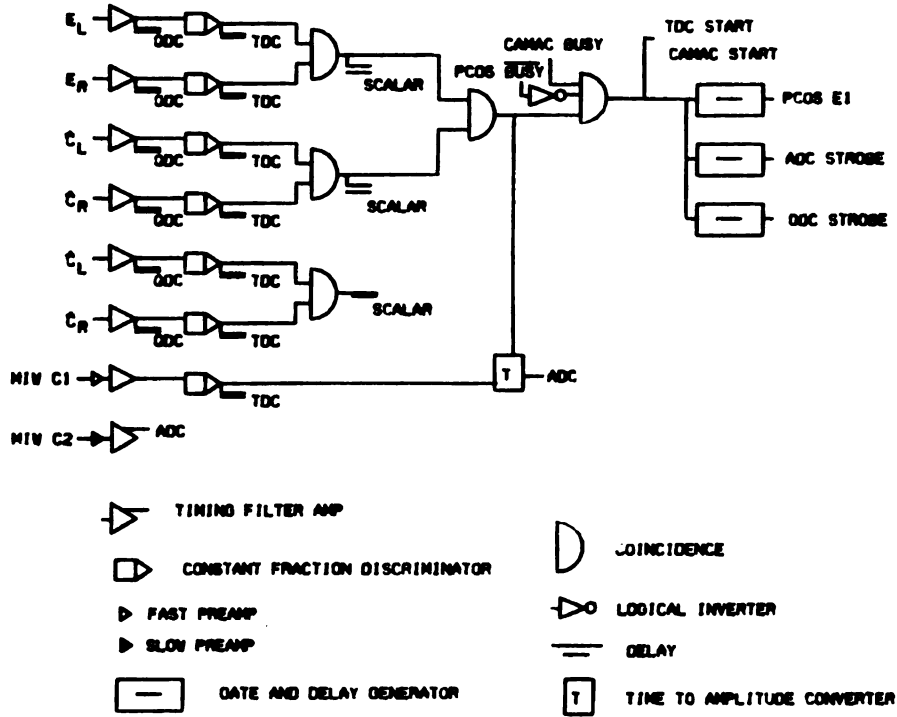


Figure B.5. The  $e^+$  experiment electronics.

whether the event was due to a single beam pulse, and a TDC channel recorded the relative time between the RF pulse and the event. This technique determined that the majority of the events with the gate  $\Delta E+E$  was due to correlated background as described above.

When the presence of high energy electrons and positrons was suspected, the electronics was again changed to include the plexiglas Cherenkov counter. The coincidence was not changed, but another ADC and TDC channel were added.

### B.3.2 The $e^\pm$ Experiment Electronics

In this experiment, the Cherenkov counters ( $\hat{C}_1$  and  $\hat{C}_2$ ) were much less sensitive ( $\sim 100X$ ) to background and were further apart, reducing the spurious event rate to a low level, so the MIW  $C_2$  requirement in the event gate could be omitted. All the time and amplitude information was recorded and available during playback, so the  $C_2$  requirement could be added offline. The definition of an event was  $E+\hat{C}_1$  (Figure B.5). An additional change was made as a response to the suggestion that the observed "particles" in the previous experiment had been the result of pileup in the electronics.

The anode of each photomultiplier was connected to a fast amplifier with two outputs; one went to a CFD, the other to a QDC. The QDC functions similarly to an ADC, but uses a much faster pulse and a smaller time window, greatly reducing the likelihood of pileup. The dynode of each



photomultiplier went to a preamp, spectroscopy amplifier, and then to an ADC. Two entirely separate numbers representing the pulse height were obtained for each event and each phototube. When the ADC value was plotted against the QDC value for a single phototube, the effects of pileup appear as an increase of the ADC signal relative to the QDC.

#### B.3.4 The $\gamma$ Telescope Electronics

The plastic scintillators and Cherenkov counters produce fast ( $\sim 10$  ns) signals, and the CsI converter produces somewhat slower signals ( $\sim 100$  ns). The anode of each of the tubes on the plastic elements has its anode connected to a fast amplifier with two outputs. One output goes to a QDC, and the other to a CFD, and from there to scalers and to the TDC. The outputs of the phototubes on the CsI converter are preamplified and sent into a slow amplifier and then to an ADC. The coincidence gate defining an event is  $\hat{C}_L^1 + \hat{C}_R^1 + \hat{C}_L^2 + \hat{C}_R^2 + \overline{\text{BUSY}}$  (Figure B.6).

#### B.4 PCOS III Electronics

The LeCroy Research Systems Corporation introduced the PCOS III (Proportional Chamber Operating System, third generation) system in 1981. This system is designed for the readout of large multi-wire proportional chambers (MWPC) quickly at a low cost per wire.

To meet these constraints, the PCOS system can only determine if the signal on the MWPC wire exceeded a threshold within a specified gate; it does not record any other pulse height or time information.

The front end of the system is the 2735 amplifier/discriminator card. This 16 channel printed circuit board resides on the detector. Fast amplifiers send the signal from each wire to fast discriminators. The output of the discriminators is a differential ECL (Emitter Coupled Logic) pulse whose width is equal to the time that the input signal exceeds the threshold. All 16 discriminators share the same threshold, which comes from a digital to analog converter in the 2731 Latch&Delay module. The MIW detector uses 12 cards, 6 for each plane.

The differential ECL outputs of two front end cards are connected to a 2731 Latch&Delay module. When this module receives a strobe from its controller, it records which wires produced a pulse above threshold during the strobe. These modules include a unique feature, a programable delay,

where the signals from the front end cards may be delayed from 300 to 682.5 nS according to instructions received by the controller. The programable delay proved not to be a useful feature; the delay was always set to the maximum (to allow time to decide if an event had taken place) and the system was very prone to oscillating and "locking up" in the "on" state. Only one threshold and delay could be set for each Latch&Delay module, corresponding to 32 wires. The 6 modules sit in a CAMAC crate near the detector and are controlled by a 2738 Readout Controller in the same crate.

The 2738 Controller can control up to 23 latches (736 wires). The controller receives the strobe to gate the Latch&Delay modules and generates the busy signal. It also arranges the sequence in which to read the wires out. It receives its instructions from the LSI computer via the 4299 Databus.

The databus resides in the same crate as the QDCs, TDCs, and ADCs. Its sole purpose is to interface the Controller and the rest of the acquisition system, and communicates with the Controller via a 50 conductor ribbon cable.

Great care must be used when cabling the PCOS system together. None of the connectors (except one) used throughout the system are polarized. This includes the power connectors. The 20 conductor ribbon cable specified to carry power to the 2735 cards allows too much voltage drop when used with more than two cards; hence the MIW

detector used 1/4" copper bus bars to distribute the power and the 20 conductor ribbon ran only from the bus bars to each card.

During the course of the experiment, five generations of 2735 cards were issued by the manufacturer in attempts to eliminate the tendency of the cards to oscillate. The final version, the 2735B, proved quite stable, but has 10x less gain than the original cards. Several versions of the 2731 modules were released, but a tendency to lock in the "on" state remained, increasing in probability with the number of modules used.

In the configuration used, the PCOS would send a header word of how many words to follow, one word per wire fired, followed a delimiter word marking the end of the string. Occasionally, the acquisition system would receive bad data from the PCOS system, in the form of string with header followed by a long list of nonexistent wires. This bad data would continue till the buffer of the LSI filled, then the LSI reset the PCOS and the problem disappeared temporarily.

In retrospect, the PCOS III system proved to be a poor choice for a small detector. A similar but simpler system made by Nanometrics of Chicago has become available, and appears to lack the problems of the LeCroy PCOS III system[Br84].

### B.5 Delay Cards

In light of the difficulties with the PCOS III system, and in order to provide a simpler way of testing the MIW detector, as well as a backup to the entire LeCroy PCOS III system, delay cards were made (Figure B.7). Each delay card connects 16 wires to a delay line (Rhombus Industries Inc. 9821 TYB 36-5), and each of the delay line to a coaxial (LEMO RPL 00.250) connector. The difference in delay of each tap on the line is 5 nS, easily resolved using the TDCs.

Although the delay lines were tested, they were never used to take data during an experiment. They are described here primarily as a testing device for detectors designed to use the PCOS III system.

The delay cards have, in addition to the delays and connectors, a 10 K $\Omega$  resistor to ground in the middle, a pair of fast clamping diodes at each end to protect external preamps from sparks, and a 50  $\Omega$  resistor termination at each end.

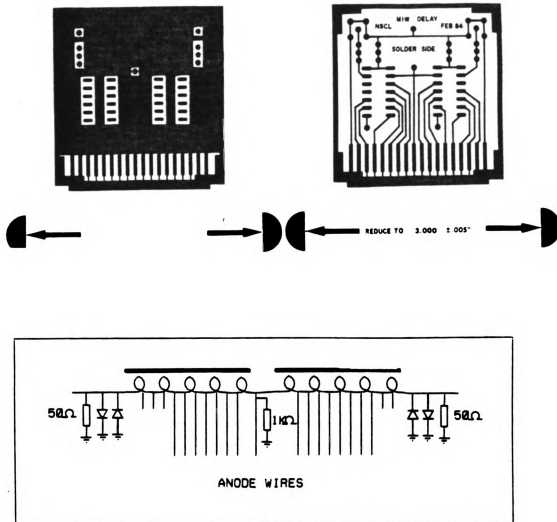


Figure B.7. Design of the delay cards.

## Appendix C

## Detector Development and Design

## C.1 MIW Counter

## C.1.1 Introduction

A magnetic spectrograph distributes particles on its focal plane according to their charge to mass ratio. While a variety of detectors have been built to measure the positions of these particles and to identify them, none of the existing designs was suitable to measure diprotons [Be82].

Three special problems are associated with measuring diprotons in the Enge split-pole spectrograph: the focal plane position of each proton crossing the focal plane must be determined simultaneously, the counter must be able to function in a very high background rate, and the counter must cope with the  $45^\circ$  incidence angle of the protons relative to the focal plane.

A simple design for a focal plane detector is a gas filled proportional chamber with a single resistive anode wire running parallel to the focal plane [Ro77]. The wire is

kept at positive high voltage; the free electrons from the ionization of the gas by the passing particle are drawn to the wire where they are accelerated by the electric field and undergo collisions with the gas, freeing more electrons [Sa77]. The position  $X$  of the particle is determined from the relative amount of charge collected at each end of the length  $L_0$  wire:

$$X = \frac{Q_L}{Q_L + Q_R} L_0$$

If two particles are present, however, this simple scheme does not work. Another way is to subdivide the cathode into strips, and connect each strip to a tap on a delay line [Ma79]. The position is then determined from the time delay in the signal reaching the end of the delay. This presents problems if the count rate is high; there may be many pulses present on the delay line simultaneously.

A high count rate limits the usefulness of a counter with a single wire, since all the ionization collects on that wire, and pileup can occur. In addition, the ionization tends to spread out along the wire, reducing the position resolution of that counter. The Multi-Wire Proportional Chamber (MWPC) overcomes these difficulties by using many wires instead of a single wire.

In the conventional MWPC, the anode wires are vertical and lie in the focal plane, and are about 5x as far from the cathodes as each other [Sa77]. A particle 45° to the focal

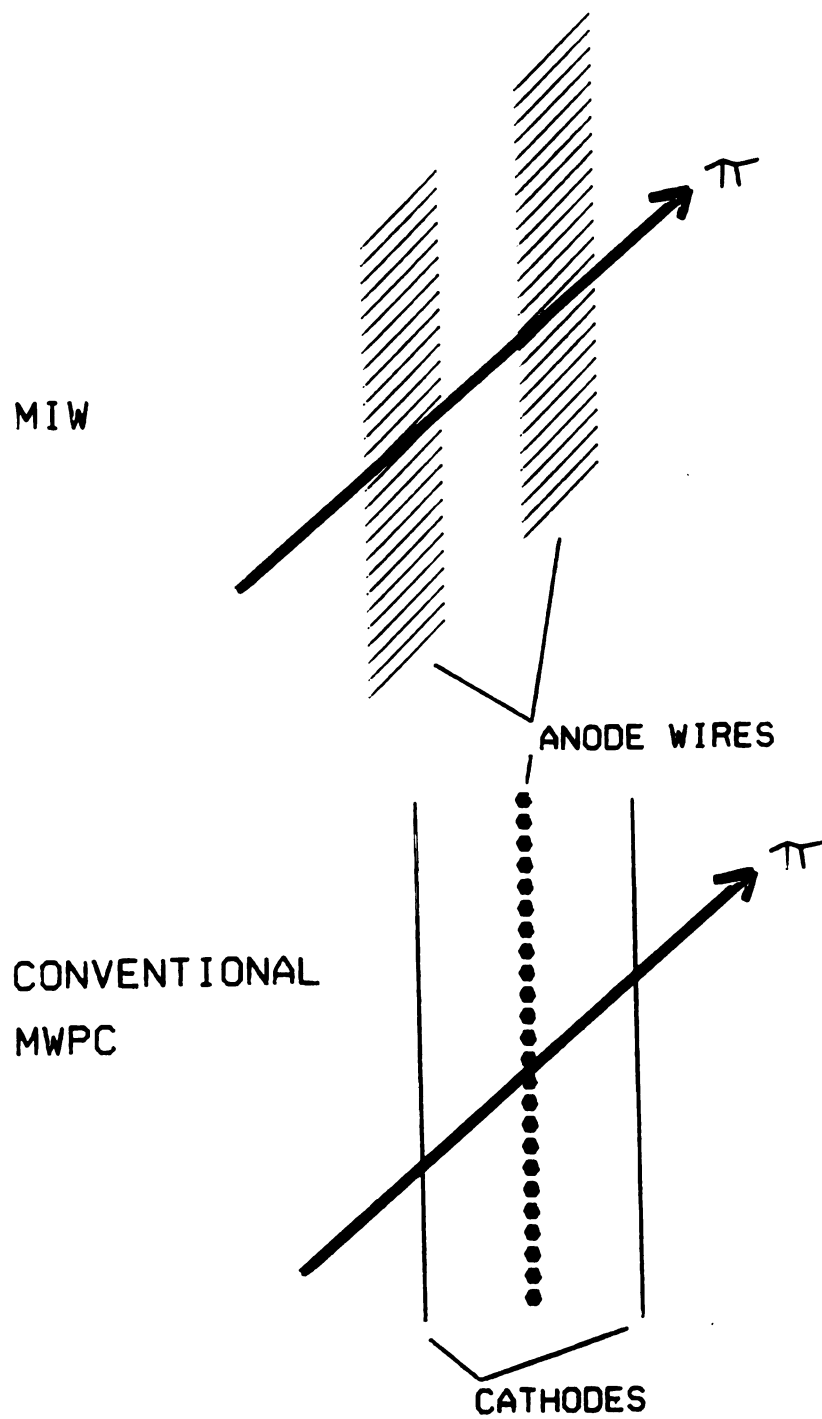


Figure C.1. The Multi-Inclined Wire concept.

plane, as is the case for the split-pole spectrograph, will divide its ionization among 9 wires (Figure C.1). By placing the wires above and parallel to the  $45^\circ$  path, the ionization would be collected by a single wire. This configuration is used in the the Multi-Inclined Wire (MIW) counter.

The MWPC configuration lends itself to a readout system in which each wire is treated as a separate counter, and connected to its own amplifier and discriminator. The LeCroy PCOS III (Proportional Chamber Operating System) was chosen since it was already to be used in the HIT detector then being built by R. Tickle and collaborators[Ti81].

### C.1.2 MIW Prototypes

The MIW detector was designed to be used with the PCOS III electronics. It would be used in air rather than vacuum to provide the cooling requirements of the amplifier/discriminator cards, each of which produced more than 5 W of heat [Le80]. The change of the goal from measuring diprotons to pions to electrons and positrons made little difference to the detector since increasing the operating voltage increases the gain substantially.

The general MIW design calls for a printed circuit board, called the anode board, to support the anode wires. The center region of the board is removed, so the anode wires are stretched across open space. On the other side of the anode board is the secondary cathode, separated from the

MSUX-82-358

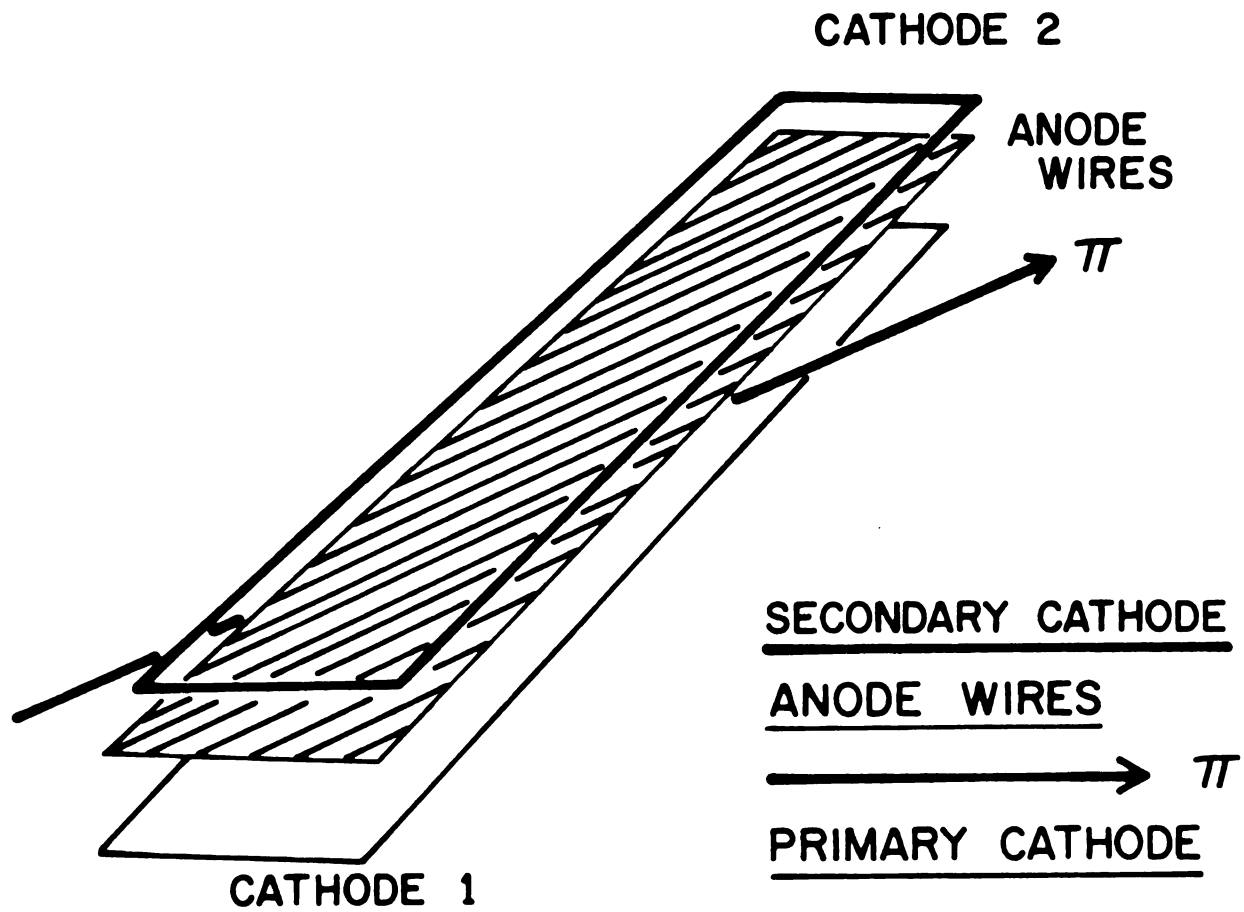


Figure C.2. The MIW counter.

wires by the thickness of the anode board. The secondary cathode is essential to the operation of the counter since a reasonably uniform electric field is required near the wires for good multiplication to take place. On the same side of the anode board as the wires, but separated by a much greater distance, is the primary cathode. The region defined by the open space in the anode board and the cathodes is the active region (Figure C.2). The anode wires remain near ground potential and the voltages on the cathodes are negative high voltage. The approximate ratio of the voltages can be found by solving Laplace's equation for cylindrical geometry.

Free electrons created by ionization in the active region drift in the electric field to the anode wires, where the signal is generated. Free electrons produced outside the active region are drawn to the anode board, but do not undergo multiplication.

The first prototype, MIW I, consisted of 32 wires with a .100" (edge) spacing, an active area ~1" deep, mounted in a large vacuum chamber, with the wires connected via small coaxial cables to the PCOS card in air. This design failed to provide any discernable signals, but several important lessons about the PCOS system and detector design were learned.

First, the detector chamber case must be well grounded to the PCOS cards immediately at the differential inputs. Unless this is done, extraneous signals completely bury the

ones from the detector. Second, the path from the wire to the PCOS card must be minimized. Last, the runners on the anode printed circuit board must be recessed from the edge of the active region, or considerable arcing will take place between the runners and the secondary cathode.

These ideas were incorporated into the next prototype, MIW II, which used the same anode board and cathodes, but mounted them in a metal box. The anode board had wires and runners extending beyond the active wires in order to provide as uniform an electric field as possible over the active region. The connection between the anode board and the connectors for the PCOS cards mounted on the lid was made by a piece of flexible flat multiconductor cable. Windows in the box allowed testing using a  $\beta^-$  source.

As an aid in testing the counter, a card was made to replace the PCOS 2735 amplifier/discriminator card. This card shorted all the wires save one to ground, and connected this wire to a  $50\Omega$  resistor and a coaxial cable leading to an Ortec 109A preamplifier, whose output ran to an oscilloscope.

The MIW II prototype (Table C.1) was tested using a  $^{106}\text{Ru}$  source producing  $\beta^-$  of up to 3.54 MeV and a scintillator placed behind the counter as a trigger, and produced current pulses at the wire of about  $10\ \mu\text{A}$ . The width of the position distribution was due to the large multiple scattering of the  $\beta^-$  particles.

Table C.1. MIW III Specifications

Number of active wires	32
Wires	12.7 $\mu$ m gold plated tungsten
Primary Cathode-Anode Gap	10 mm
Secondary Cathode-Anode Gap	1.57 mm
Gas	1 atm 50-50 argon-ethane
Typical Operating Voltages	
Primary Cathode	-4.53 KV
Secondary Cathode	-1.51 KV
Anode	0 V

Table C.2. MIW connectors.

anode board	Samtec TS-132-G-A (modified)
adaptor board	Samtec SS-132-G-2 (modified)
gas box lid	Viking 3VH18/1JND12

The next prototype, MIW III, used a similar gas box, but had several important improvements. The spacing of the wires as measured along the edge was doubled to 0.200" (5.08 mm) and the primary cathode-anode gap increased to 20 mm. Testing with this prototype indicated that increasing the gap beyond this limit reduced the position resolution of the counter. The anode board was subdivided into two separate counters, each with 16 anode wires, lying in the same horizontal plane, one ahead of another; this provides better rejection of spurious events and a measurement of the angle followed by the ionizing particle.

The connections between the wires and the PCOS cards outside the gas box was made using mating Samtec[Sa85] male connectors on the anode board with every other pin removed (to provide .20" spacing) and an adapter printed circuit board with similarly modified female connectors (Table C.2). The adapter board runners connected the pins of the Samtec connectors to the pins of the wire-wrap style Viking[VI79] 36 pin card edge connectors epoxied to the lid of the gas box. In this way, a large number of reliable, gas tight connections were made to the PCOS card. This consideration was important, since the final detector would have nearly 200 wires to feed through a gas tight seal.

This version was tested extensively, and deliberately allowed to spark in order to determine its region of operation. The final version, MIW IV, would be too difficult to repair after this destructive testing. A plot

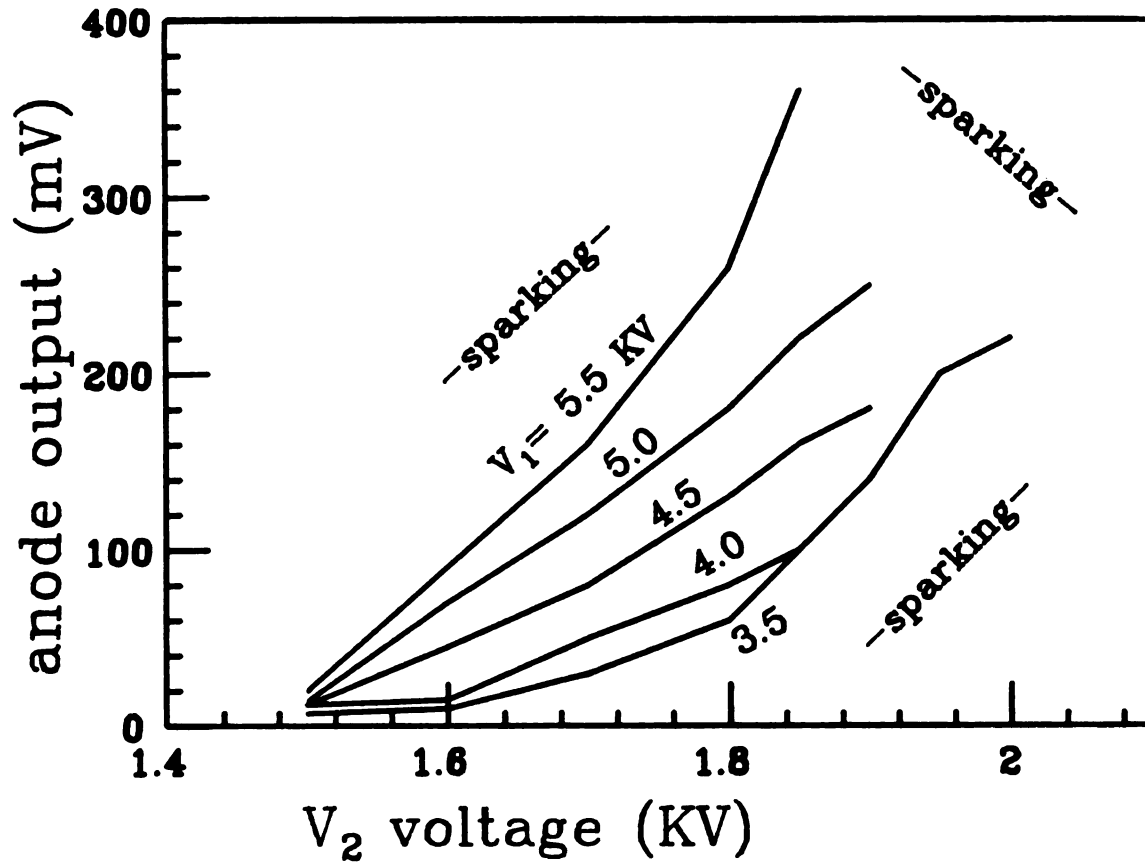


Figure C.3. Operating voltages of the MIW III prototype using 1 atm 50-50 argon-ethane.

of the pulse height out vs. secondary cathode voltage is displayed in Figure C.3.

### C.1.3 MIW IV

The final detector design, MIW IV, (Figure C.4) is very similar in principle to that the prototype MIW III (Table C.3). The gas box is made of aluminum alloy and uses O-ring seals for all removable parts. The Viking card edge connectors were potted into the lid with epoxy to form a gas tight connection. The secondary cathode is epoxied to the anode board to prevent the wire tension from bending the anode board, and polycarbonate supports for the male Samtec connectors on the anode board are used to prevent damage to the connectors. The adapter board is rigidly attached to the lid by screws and .25" phenolic spacers to prevent flexing when the 196 electrical connections (192 wires and 4 grounds) are made or broken. Polycarbonate supports hold the secondary cathode-anode assembly and the primary cathode rigidly, and are not prone to damaging the wires when they are removed, as was a problem in MIW II and III.

The  $1M\Omega$  resistors used for current limiting to each cathode in the case of a spark were moved to a box external to the detector. A .01  $\mu F$  capacitor within the box was connected from the cathode side to a BNC connector so that a signal could be picked off the cathode and run into a preamp. The detector used gas tight MHV connectors rather

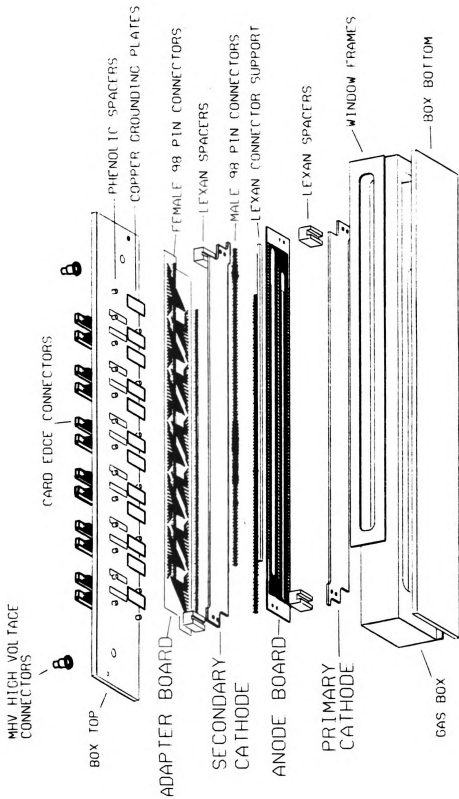


Figure C.4. Assembly view of the MIW IV counter.

Table C.3 MIW IV specifications

Active wires in each plane:	96
Primary Cathode-Anode gap:	.787"
Secondary Cathode-Anode gap:	.062"
Wire spacing (normal to the wires):	0.1414"
Wire spacing (along the focal plane):	.200"
Size of each active region:	19.2" x .7"
Distance between Planes (center to center perpendicular to focal plane):	1.125"
Wire:	.0005" gold plated tungsten
Wire Tension:	5g
Electronics requirements:	12 PCOS 2735 Amplifier/Discriminator Cards requiring +5V@5.4A and -5VDC@7.0A
Typical operating conditions:	
gas:	1 atm. CF <sub>4</sub>
Voltages- Cathode 1:	-5.5 KV
Cathode 2:	-1.96 KV

than SHV since SHV to solder lug gas tight connectors were not available.

## C.2 The $^{12}\text{C}(\alpha, p)^{15}\text{N}^*$ Test of the MIW

A test was needed to determine how well the MIW counter actually worked. The pions it was designed to measure would have a production rate of only  $\sim 1/\text{hour}$ , a rate far too low to use to test or adjust the detector.

Any useful test needed to meet several conditions; the particles must be penetrating enough to penetrate the exit window, air, MIW counter,  $\Delta E$  scintillator and stop in the E scintillator, they must have a rigidity low enough for the Enge spectrograph to bend them to the MIW's focal plane position, and the particles should represent a discrete spectrum with the levels separated by several wires to test the MIW position resolution. The wires in the MIW are .200" apart along the focal plane, corresponding to roughly 17 KeV/channel for 80 MeV protons.

A good choice was the reaction  $^{12}\text{C}(\alpha, p)^{15}\text{N}^*$  at  $E_{\alpha} = 20 \text{ MeV/u}$ . The first excited state of  $^{15}\text{N}$  is about 5.3 MeV above the ground state [Le67] and the cross section for the formation of the ground state should not be very small [Gl71]. With the maximum field, the protons from the ground state would fall well on the detector, and the range of the protons was greater than the thickness of the  $\Delta E$  scintillator.

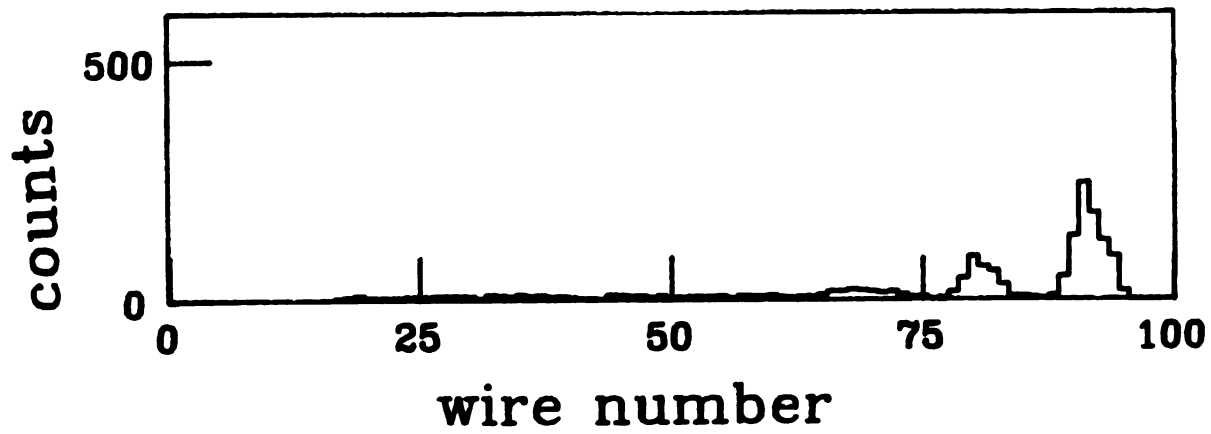


Figure C.5. Spectrum of alpha particles from  $^{12}\text{C}(\alpha, \alpha')^{12}\text{C}$  at  $E_\alpha = 80$  MeV.

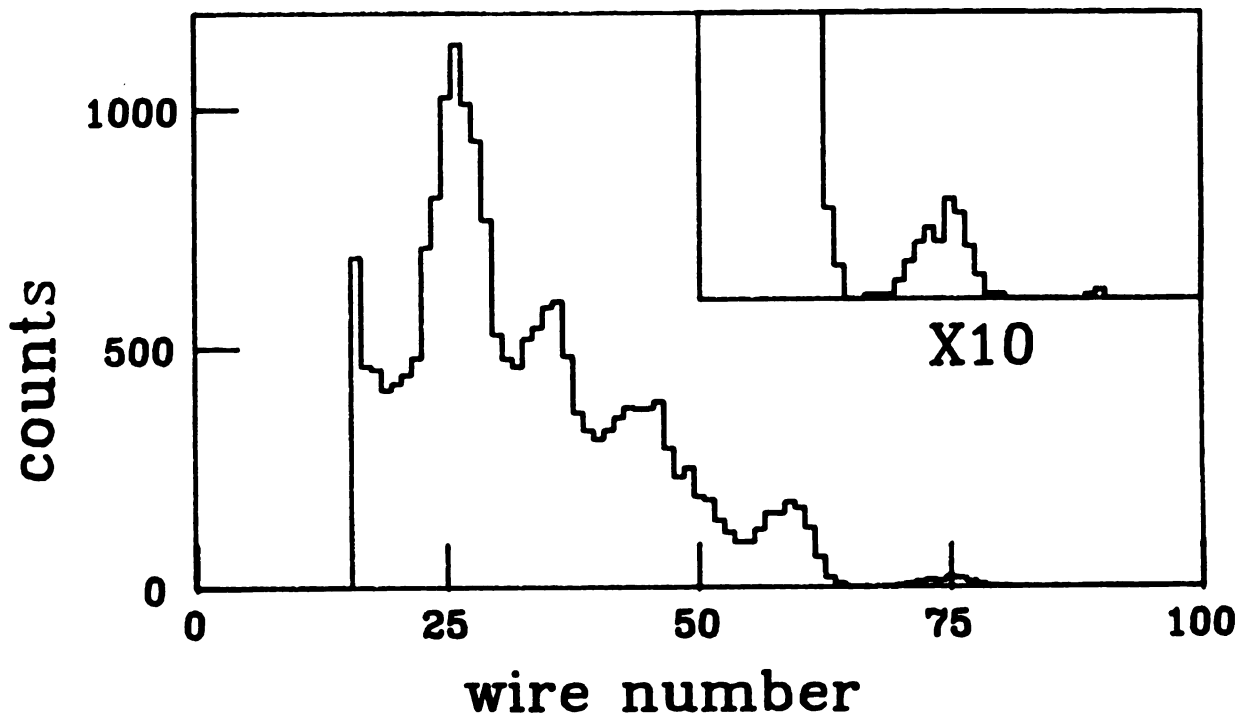


Figure C.6. Protons measured simultaneously using the reaction  $^{12}\text{C}(\alpha, p)^{15}\text{N}$ .

The elastically scattered alphas, however, have nearly the same momentum to charge ratio as the ground state protons. These alphas were numerous enough that reactions taking place within the  $\Delta E$  scintillator were triggering the E scintillator approximately as often as protons were. Using the particle ID plot, however, allowed the complete elimination of the alpha particle background (Figure C.5) and produced a very clean  $^{15}\text{N}$  spectrum (Figure C.6) despite the large number of alphas passing through the MIW, giving justification to its claim of being able to function in high background.

### C.3 Scintillators

#### C.3.1 Introduction

As charged particles penetrate matter, they lose kinetic energy. Scintillators are materials which convert some of this energy into light. By measuring the amount of light produced, the energy loss of the charge particle can be determined.

Many scintillators are commercially available. Inorganic scintillators, such as NaI(Th), BGO, CsI, CaF, produce a relatively large amount of light ( $\sim 1\gamma/25$  eV), with a relatively long decay time ( $\sim 200$  ns)[Ag82]. Plastic scintillators, such as the Bicron BC-400 and Nuclear Enterprises NE-100 series, are not as efficient ( $\sim 1\gamma/100$  eV), but produce all the light within a short time ( $\sim 10$  ns)[Ag82, Bi83, Nu72]. Recently, slow plastic scintillator has been developed, with a decay time similar to that of inorganic scintillator[Hu85].

Plastic scintillators are easily and cheaply machined or cast into large shapes, have a low Z and density, and can be polished for total internal reflection. Low atomic number Z means that plastic is less sensitive to gamma-rays, but the presence of hydrogen makes it more sensitive to neutrons than inorganic scintillator.

### C.3.2 Scintillator Design

All the plastic scintillators used in these experiments were made of Bicron BC-408, plexiglas UVT (Ultra-Violet Transmitting) light pipes, and 2" photomultipliers (both the RCA 8575 and its equivalent the Hamumatsu 329 were used). The size of each scintillator was dictated by the energy loss and multiple scattering of the particle, the solid angle of the spectrograph, and the size of the MIW position sensitive counter.

Since the original experiment was to have measured 20-100 MeV pions, the  $\Delta E$ -E scintillator telescope needed to be able to stop all the pions within the E scintillator. An absorbing wedge behind the MIW and ahead of the telescope could be used to slow the pions above 40 MeV, but left the problem of the pion's stopping position due to the angle of the pion's entry. A pion could enter anywhere between  $36^\circ$  and  $54^\circ$  to the normal of the telescope, meaning the E scintillator needed to be at least 6 cm thick. Multiple scattering of the pion increases the required size somewhat, so the E (later called  $E_3$ ) scintillator was made 3.0" (7.6 cm) thick.

The  $\Delta E$  scintillator was chosen so that a 40 MeV pion passing through it (at  $45^\circ$  to the normal) would lose about 5 MeV. This made the  $\Delta E$  scintillator .25" (.63 cm) thick. The other dimensions of the scintillators were determined by

Table C.4 Dimensions of the active region of the scintillators.

<u>Dimensions (in.)</u>	<u><math>\Delta E</math></u>	<u><math>E_3</math></u>	<u><math>E_1</math></u>
thickness	.25	3.0	1.0
height	2.0	3.0	2.0
length	24.0	26.0	24.0

the spectrograph and the MIW (Figure 2.2), the final scintillator dimensions are shown in Table C.4.

Due to the unavailability of high energy beams to make pions, the experiment was later limited to 20-40 MeV pions. A new E scintillator was made with this in mind, called  $E_1$  (Figure C.7). The decreased size of the E scintillator decreased background by roughly the ratio of the volumes without sacrificing any solid angle.

The light pipes needed to be reasonably efficient. They also needed to reduce the position dependence of the signal as much as possible, and to allow placement of the magnetic shielding around the phototubes.

The  $\Delta E$  scintillator light pipes were made of .25" x 2.0" x 10.0" plexiglas UVT, heated, bent, and polished to mate the flat scintillator to a partial circle on the photomultiplier. This provides light more uniformly distributed on the photocathode of the photomultiplier tube and a much stronger joint. The light pipes of the  $E_3$  scintillator were made of a single large piece of plexiglas UVT about 14" long tapering from a square to a 2" diameter cylinder. The  $E_1$  light pipes were plexiglas UVT pieces 1" x 2" x 3.5" and 1" x 2" x 4.5".

All these designs satisfied the requirements. The  $\Delta E$ ,  $E_3$ , and  $E_1$  scintillators have position dependence of the signals of only about 10%. All three used double magnetic shields, so that there was no measured shift in gain of the tubes even with the spectrograph at its maximum field.

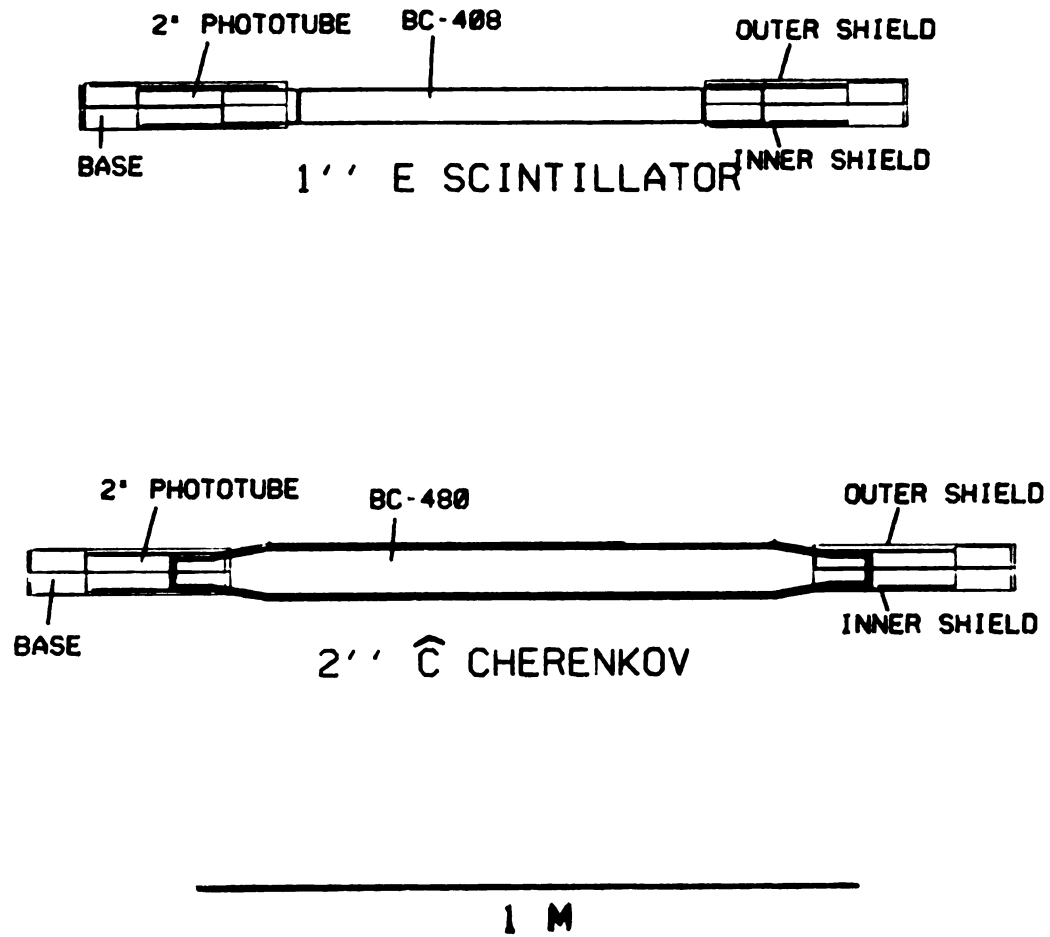


Figure C.7. Scintillator and Cherenkov detector used in the  $e^{\pm}$  experiment.

#### C.4 Cherenkov Detectors

As a charged particle moves through a medium at a speed greater than the speed of light in that medium, light is produced at an angle depending on the speed of the particle and the index of refraction of the medium. This light is called Cherenkov light, and is primarily produced at short wavelengths[Ma69]. The blue glow surrounding the core of a water cooled nuclear reactor is a manifestation of this effect, as large numbers of  $\beta$  particles are ejected by the fission fragments into the water, in turn producing photons of Cherenkov light.

The advantage of a Cherenkov detector is that it is completely insensitive to particles with a velocity less than  $c/n$ . This makes it a powerful tool in discriminating against slower particles. The difficulty is that Cherenkov detectors produce much less light than a scintillator, (typically, for a high energy electron,  $\sim 500 \gamma \sin^2 \theta_c / \text{cm}$ , or  $\sim 1 \gamma / 4 \text{ KeV}$  in plastic)[Ag82]. A drawback, however, is that various gamma ray interactions in the plastic produce relativistic electrons seen by Cherenkov detectors.

The first Cherenkov counter used in these experiments was a single piece of 24"x2"x1" plexiglas UVT (so as to transmit as much light to the tube as possible) with a single phototube glued to the high radius end. Since the electrons ( $\gamma \gg 1$ ) were entering at  $45^\circ$  to the counter, most

of the internally reflected light would be expected to arrive at that end. The critical angle is  $(n - 1.5)$ [Ag82]:

$$\theta_C = \text{Acos} \left\{ \frac{1}{\beta n} \right\} = 66^\circ$$

so that the light on the low radius end would strike the surface near  $24^\circ$  to the surface, and little would be internally reflected.

While this counter was simple, it had two drawbacks. The thermal noise from the tube overlapped the size of the signals, and the counter was not uniformly responsive along its length. The coincidence requirement eliminated most of the thermal noise, but it made determining the efficiency of the counter difficult.

A recent development, Bicron Corp. introduced a plastic wavelength shifter specifically designed for Cherenkov detectors[Hu84]. This plastic, BC-480, shifted the Cherenkov light into longer wavelengths suited to common phototubes and simultaneously re-emits the light isotropically. This greatly decreases the position dependence of the signal.

The  $e^\pm$  experiment essentially eliminated the background from  $\gamma$ -ray interactions and thermal noise by using two separated identical telescopes on BC-480 with phototubes on either end (Figure C.7). The size of the Cherenkov counters was increased to allow for multiple scattering of lower ( $\sim 20$  MeV) electrons, and the ends tapered to allow the use

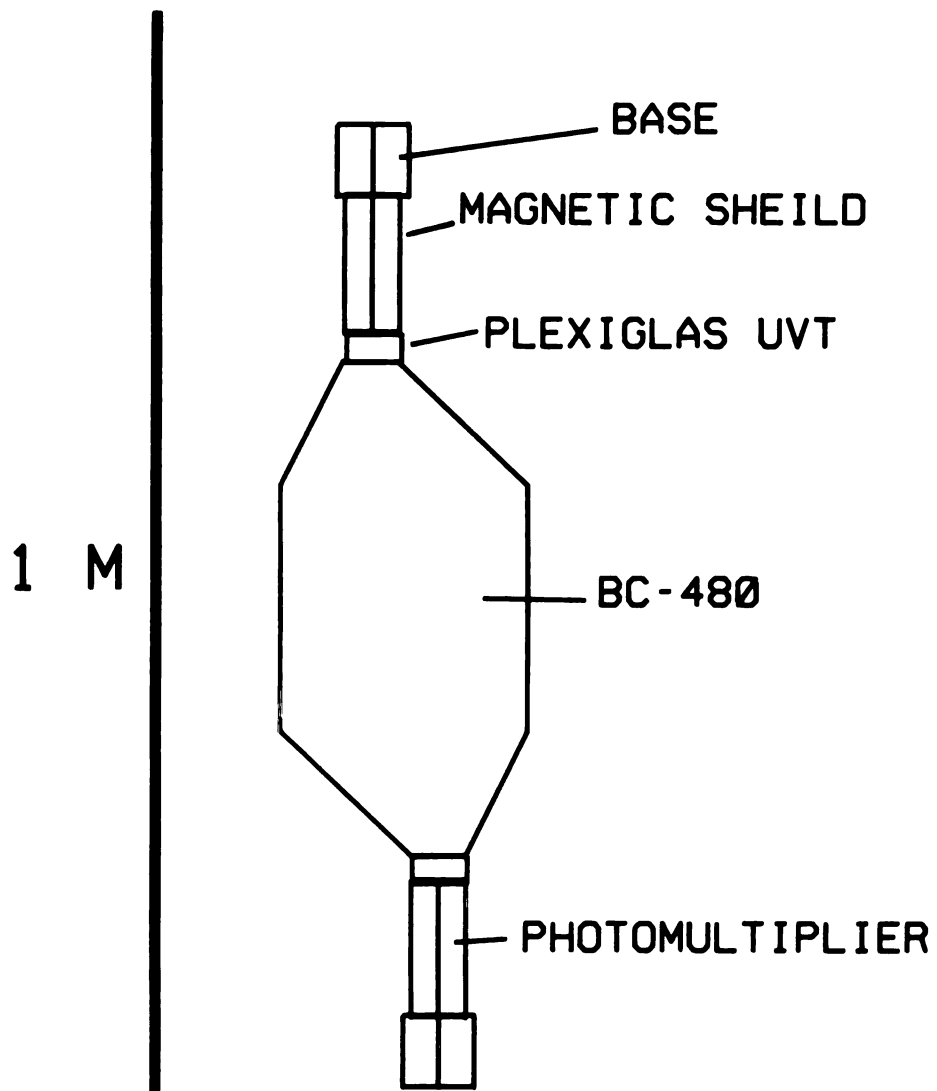


Figure C.8. Cherenkov element of the High Energy Gamma-Ray Telescope.

of magnetic shields. The light pipe was integral with the Cherenkov counter to maximize efficiency.

The same idea was carried over into the High Energy Gamma-Ray Telescope (Figure 5.2). Each Cherenkov element (Figure C.8) would measure the passage of 0, 1, or 2 electrons (or a cosmic ray muon) (Figure 5.5). The muons provided the normalization between the elements. The first element was .5", the next 1", so that low energy  $e^+e^-$  pairs could be better measured. The next 8 elements were 2" thick. Due to their increased thickness, a plexiglas UVT "cookie" was used to adapt the 2" phototubes (RCA, Hamumatsu, and EMI RCA 8575 equivalents) to the elements. The phototubes were offset to allow for clearance of the phototube bases.

## Appendix D

## Computer Codes

**D.1 Acquisition Code**

The code SARA[Sh85] was used for all acquisition and playback of the data for all the experiments. Generally, this code is flexible enough to handle most experiments, with all the user defined parameters and pseudo parameters placed in the subroutine DATA68K called by the main program. The PCOS III system used in the spectrometer experiments produces a variable number of words; two plus the number of wires which fired. This means special care must be taken in decoding the data buffer; it is not listed here since the routine used has been made obsolete by subsequent revisions of SARA. Modifications were also to the histogram updating section of SARA in order to allow multiple updates of a histogram during a single event. This was necessary to monitor the detector for "dead" or "hot" wires; ones which either never or always fired.

The PCOS system was connected to the MIW counter such that each of the latches had channels 0-15 connected left to

right to the front plane and 16-31 right to left to the rear plane behind the front plane. The latch numbers ran 0 to 5 left to right. This was done so that the failure of a single latch would disable only one sixth of the detector rather than a third. The wire numbers run 0-95 left to right on the front plane and 96-191 right to left on the rear plane. This special version of the subroutine, DATAQ2, assigned the average of the front wire numbers to variable "FrontAv", and 191 minus the average of rear wire numbers to "BackAv".

The routine used to decipher the PCOS words taken from the data buffer "IBUF(IPOINT)" is taken from DATAQ2.

## D.2 MIW Detector Simulation SCATTER and Subroutines

```

C
C          SCATTER .....K.Beard 12/6/84
C
C          calculates multiple scattering trajectories through MIW and
C          extracts efficiencies for varies energies and angles
C
C
C
C          real pot
C          character*20 INNAME(40),HNAME(40)
C          character*5  ENAME(0:10)
C          dimension Npart(10),Iw(-10:100,0:5),Eloss(-10:100.5)
C          dimension Rpot(40),Rstep(40),Iwsum(0:40)
C          common/particle/X,Y,Z,angXZ,angY,xM0,T,step,MIW_el
C          common/element/extent(0:10,0:10,0:3)
C          common/statistics/resultz(0:10,6),Tke,Nthpart,Iel
C          common/randM/ISEED
C          ISEED=999999
C
C
C          xM0=.511
C
C
C          type *
C          type *
C          type *, ' program MIWscat.....K.Beard 12/84'
C          type *
C          type *, ' running instructions come from SCATT:, logical'
C          type *, ' name assignment of file generated by program ROSTER'
C
C
C          open(unit=4,name='SCATT:',status='old')
C          icyc=0
86          icyc=icyc+1
C          read(4,87) Npart(icyc),Rpot(icyc),Rstep(icyc),
C          1INNAME(icyc),HNAME(icyc)
87          format(1x,I5,F8.3,F10.5,5x,A20.5x,A20)
C          if(Npart(icyc).ge.1) go to 86
C          icyc=icyc-1
C          close(unit=4)
C
C
C          cycle throuth the list from ROSTER.DAT
C
C          DO kcyc=1,icyc
C
C          pot=abs(Rpot(kcyc))
C          step=Rstep(kcyc)
C
C          read in description of MIW
C
C          open(unit=2,file=INNAME(kcyc),status='old')
C
C          read(2,123) kz1,(extent(0,0,j),j=0,3)
123          format(I5,4F15.5)
C
C          read(2,122) (ENAME(n),n=0,10)
122          format(1x,11A5)
C

```





```

C
C      open(unit=1,file='TEMPORARY.DAT',status='old')
C
C      Ielast=-1
C      Lpart=-1
C      Nthpart=0
C      Iel=0
C
C      do k=0,5
C      do j=1,ibin
C      Iw(j,k)=0
C      enddo
C      enddo
C
C      do while (Npart(kcyc).gt.Nthpart .or.
1          (Npart(kcyc).eq.Nthpart .and. Iel.ge.0))
C
C      read(1,33) Nthpart,X,Y,Z,T,angXZ,angY,Iel
33      format(I10,6F15.5,13)
C
C
C      if(Nthpart.ne.Lpart) then
C          iwr=(X/2.54)/(.2*wide)+1
C          deg=angXZ*180./3.14159
C          Iw(iwr,0)=Iw(iwr,0)+1
C          endif
C
C      if(Iel.eq.Ielast) then
C          Eloss(iwr,Iel)=Tlast-T
C          endif
C
C          Iel<0 ends the particle track
C
C      if(Iel.lt.0) then
C          do ik=1,5
C          if(Eloss(iwr,ik).ge.thrsh) Iw(iwr,ik)=Iw(iwr,ik)+1
C          Eloss(iwr,ik)=0.
C          enddo
C          endif
C
C          Lpart=Nthpart
C          Ielast=Iel
C          Tlast=T
C
C      enddo
C
C      close(unit=1,DISPOSE='DELETE')
C
C      open(unit=3,file=HNAME(kcyc),status='new')
C
C      name of file....
C      write(3,676) HNAME(kcyc),INNAME(kcyc)
676      format(10x,A20,10x,'....with detector configuration ',A20)
C
C      sources for this calculation
C
C      write(3,666) INNAME(kcyc),Rpot(kcyc),Rstep(kcyc)
666      format(' MIW description=',A20,' pot=',F7.2,' step size=',

```

```

1   F6.4,'cm')
c
c           tables
677   write(3,677) (ENAME(1),l=0,10)
      format(/,3x,'bin',3x,A5,1x,A5,1x,A5,1x,A5,1x,A5,1x,A5,1x,A5,1x,A5,
1     1x,A5,1x,A5,1x,A5)
c
      do j=0,5
        Iwsum(j)=0
      enddo
c
      do it=1,ibin
678   write(3,678) it,(Iw(it,k),k=0,5)
      format(7I6)
      do k=0,5
        Iwsum(k)=IW(it,k)+IWsum(k)
      enddo
      enddo
c
679   write(3,679)
      format(6x,'-----')
680   write(3,680) (Iwsum(l),l=0,5)
      format(6x,6I6)
c
      type 600,HNAME(kcyc)
600   format(5x,A20,' written')
c
      close(unit=3)
c
c
c   ENDDO
c
      end

```

```
c
c      subroutine NEXT
c      common/particle/X,Y,Z,angXZ,angY,xM0,T,step,MIW_el
c      common/element/extent(0:10,0:10,0:3)
c
c          proceed to the next detector element
c
c      Zedge=extent(MIW_el,1,3)
c
c      deltaZ=Zedge-Z
c      Z=Zedge
c      X=X+deltaZ/tan(angXZ)
c      Y=Y+sin(angY)*deltaZ/sin(angXZ)
c
c      return
c      end
```

```

c
c      subroutine STATZ
c
c          puts results into array "resultz"
c
c      common/particle/X,Y,Z,angXZ,angY,xM0,T,step,MIW_el
c      common/statistics/resultz(0:10,6),Tke,Nthpart,Iel
c
c      entraning & exiting coords
c      resultz(MIW_el,6)=angY
c      resultz(MIW_el,5)=angXZ
c      resultz(MIW_el,4)=Tke
c      resultz(MIW_el,3)=Z
c      resultz(MIW_el,2)=Y
c      resultz(MIW_el,1)=X
c
c      return
c      end
```

```
subroutine FILEZ(num_part)
C
C      puts results of a particle into a file
C
common/particle/X,Y,Z,angXZ,angY,xM0,T,step,MIW_e1
common/statistics/resultz(0:10,6),Tke,Nthpart,Ie1
C
write(1,33) Nthpart,(resultz(MIW_e1,k),k=1,6),Ie1
33 format(I10,6F15.5,I3)
C
C
return
end
```



```
function Bfield(ypot)
c
c
c
f0=(ypot+.9205)/11.476
f=f0
c
do 100 k=1,25
z=XPOT(f)
if(z.gt.ypot) f=f-f0/2**k
if(z.lt.ypot) f=f+f0/2**k
100 continue
c
freq=f
Bfield=freq/4.2577
end

function XPOT(freq)
xpot=-.9205+11.476*freq+4.9023e-10*freq**6
xpot=xpot-1.9262e-13*freq**8+4.5274e-17*freq**10
end

function xMOMENT(Bkg,DX)
c
Bkg in Kg, DX in inches
rho= (89.557-DX)/2.48306
xMOMENT= Bkg*rho/1.3132465
end
```

```

C
C
C      subroutine NEWDIRECT
C
C          finds the new direction of the particle
C
C      real p,phi
C      common/particle/X,Y,Z,angXZ,angY,xM0,T,step,MIW_el
C
C      angXZ.....angle (in rad.) to X axis in XZ plane
C      angY.....angle (in rad.) to XZ plane
C      theta.....angle (in rad.) particle scattered relative
C                to original direction of travel
C      phi.....azimuthal angle of scatter (with respect to
C                X axis)
C
C
C      first get the theta,phi due to a scattering
C
C      call SCATEL(theta,phi)
C
C
C      find the new angles of the particle
C
C      a=angXZ
C      b=angY
C      th=theta
C      p=phi
C      sa=sin(a)
C      ca=cos(a)
C      sb=sin(b)
C      cb=cos(b)
C      st=sin(th)
C      ct=cos(th)
C      sp=sin(p)
C      cp=cos(p)
C
C      these transformations convert the old direction&theta,phi into
C      the new direction
C
C      aprime=Atan2(ct*sa*cb-ca*cp*st-sa*cb*sp*st,
1 sa*cp*st-ca*sb*sp*st+ct*ca*cb)
C
C      bprime=Asin(-cb*sp*st+sb*ct)
C
C      angXZ=aprime
C
C      angY=bprime
C
C      return
C      end

```

```

C
C
C      subroutine NEWCOORD
C
C      finds new XYZ coords given direction & old coords
C
C      X.....parallel to focal plane (cm)
C              zero at lowest active wire,+ toward greater radii
C      Y.....vertical (cm)
C              zero on median plane,+ up
C      Z.....horizontal perpendicular to focal plane (cm),
C              & away from Split-Pole
C
C      common/particle/X,Y,Z,angXZ,angY,xM0,T,step,MIW_el
C      common/element/extent(0:10,0:10,0:3)
C
C      X=X+step*cos(angY)*cos(angXZ)
C      Y=Y+step*sin(angY)
C      Z=Z+step*cos(angY)*sin(angXZ)
C
C      T=T-dEdX(MIW_el,T)*step
C      return
C      end
C
C      function dEdX(Ielement,xKE)
C      common/element/extent(0:10,0:10,0:3)
C
C      dEdX in MeV, step in cm, density in g/cm**2
C
C      density=extent(Ielement,0,1)
C      dEdX=1.9*density
C      end

```

```

C
C
C      function inside(MIW_el,X,Y,Z)
C
C      returns a true or false depending whether XYZ lies within or without
C      detector element #MIW_el
C
C      common/element/extent(0:10,0:10,0:3)
C
C      there are coords for each corner of the element in extent
C
C      extent.....gives the physical extent of the element
C                  (MIW_el,point#,X or Y or Z (1,2,3))
C                  point#0= # of points to describe a quadrant
C                  (MIW_el,0,3)...Z coord of front edge
C                  (MIW_el,1,3)...Z coord of back edge
C
C
C                  test to see if within Z extent of element
C
C      kpts=extent(MIW_el,0,0)
C      Zedge=extent(MIW_el,1,3)
C      Zthick=extent(MIW_el,kpts,3)
C
C                  implicit 45 deg offset of detector elements
C                  included in definition of "Xa"
C
C      xa=abs(X-Zedge)
C
C      ya=abs(Y)
C
C      za=Z
C      if(za.lt.Zedge) then
C                  inside=.false.
C                  return
C      endif
C      if(za.ge.Zedge+Zthick) then
C                  inside=.false.
C                  return
C      endif
C
C                  if within Z extent, check XY plane
C
C      dir=Atan2(ya,xa)
C
C      do k=extent(MIW_el,0,0),2,-1
C
C      xc=extent(MIW_el,k,1)
C      yc=extent(MIW_el,k,2)
C
C      if(Atan2(yc,xc).ge.dir) kpair=k
C      enddo
C
C      x1=xc
C      y1=yc
C      x2=extent(MIW_el,k-1,1)
C      y2=extent(MIW_el,k-1,2)
C

```

```

c
front_edge=extent(MIW_e1,1,3)
c
c      set center
c
Z0=front_edge
X0=0.
Y0=0.
c
c      slope & intercept of line connecting corners
a=(Y1-Y2)/(X1-X2)
b=(Y1*X2-X1*Y2)/(X2-X1)
c
c      point on line closest to X,Y
X1=(X+a*Y+a*b)/(1.+a*a)
Y1=a*X1+b
c
c      distances to center
dEdge2=(X1-X0)**2+(Y1-Y0)**2
dXY2=(Xa-X0)**2+(Ya-Y0)**2
c
if(dXY2.lt.dEdge2) then
inside=.true.
else
inside=.false.
endif
end

```

```

C
C
C      descriMIW.....K.Beard 12/7/84
C
C      requests critical MIW detector parameters and puts
C      them into a file called "descriMIW.dat" using the
C      proper format for program "MIWscat" to read
C
C
C      the form of the data file:
C
C      0(focal plane),# elements,0,0,0
C      name element,name element,.....
C      #element,# of description pts,density,Z atomic,A atomic
C      #element, 0, X,Y, front edge location
C      #element, 0, X,Y, 0
C      #element, 0, X,Y, 0
C      #element, radiation legnth,X,Y, thickness
C      .
C      .
C      .
C
C      character*5 ENAME(0:10)
C      dimension extent(0:10,0:10,0:3)
C      open(unit=1,file='descriMIW.dat',status='new')
C
C      do l=1,10
C      ENAME(l)=' '
C      enddo
C
C      zeroth element is the MIW mwpc
C      ENAME(0)='MIW'
C
C      type *,'how many elements to this configuration '
C      type *,'          not including the MIW gas detector?'
C      accept *,Last
C      extent(0,0,0)=Last
C      type *
C      do k=1,Last
C      type *,' element#',k
C      type *,' front edge to focal plane distance (cm)'
C      accept *,Zedge
C      extent(k,1,3)=Zedge
C      type *
C      type *,' description of element.....'
C      type *,' name of element (A5)'
C      read(5,76) ENAME(k)
C      format(A5)
76      type *,' how many points for a quadrant description'
C      type *,' including axis?'
C      accept *,kpts
C      extent(k,0,0)=kpts
C      type *
C      m=1
C      type *,' point#',m,'          rotating from horizontal'

```



```

C
C
C      program          ROSTER
C
C      makes list of combinations to run in MIWSCAT
C      and puts them in ROSTER.DAT
C
C
C      character*20 INNAME,OUTNAME,HNAME,blk
C      open(unit=1,file='ROSTER.DAT',status='new')
C      blk='
C      type *
C      type *, ' program ROSTER.....K.Beard 12/84'
C      type *
C      type *, ' first run descriMIW then rename the output file'
C      type *, ' (originally named descriMIW.dat)'
C      type *
C      type *, ' end inputs with a 0,0,0'
889  type *, ' input the number of particles to be run, pot setting,
1 and step size (cm)'
      accept *,Npart,xpot,step
      if(Npart*xpot*step.le.0) then
            Npart=0
            write(1,2) Npart,xpot,step,blk,blk
            stop
            endif
      type *, ' name of the file containing the description of the MIW'
      read(5,3) INNAME
      type *, ' name to hold histogram information'
      read(5,3) HNAME
3      format(A20)
      write(1,2) Npart,xpot,step,INNAME,HNAME
2      format(1x,I5,F8.3,F10.5,5x,A20,5x,A20)
      go to 889
      end

```

### D.3 Pair Production Simulation GAMMATEE and Subroutines

```

C
C      GammaTee.....K.Beard 1/9/85
C      modified to read instructions from file 1/10/85
C      modified to include target and energy loss 1/14/85
C      modified to give output in counts/1M gamma 2/12/85
C      modified to use Plank distribution 3/5/85
C
C      takes a distribution of gamma rays and converts
C      to an electron/positron distribution using the
C      correct cross sections
C
C      common/Plank/ Xplank,Yplank,Temp
C      common/lookup/ sigT,Fze,XintFze,Egamma
C      common hv,Ze,Z
C      dimension Xplank(0:500),Yplank(0:500)
C      dimension sigT(2,100),fze(2,100,0:100),XintFze(2,100,0:100)
C      dimension Z(2),A(2),Den(2),thick(2)
C      dimension Pmom(0:200),Igam(0:200),iEbin(0:200),sigTOTAL(2),Xprob(2)
C      character*30 GammaFile,PositronFile
C      real hv,k,NA,mc2
C      iseed=9999
C      type *, ' program GammaEE.....by K.Beard'
C      type *, ' instructions from file "GEF:"'
C      type *
C      type *, ' files written:'
C
C
C      1: target
C      2: converter
C
C      units:
C      NA=6.023E+23 !atoms/mole
C      A=g/mole
C      Den= g/cm**3
C      Thick: cm
C      mc2=.511 !MeV
C      dEdx= 1.9 !MeV/(g/cm**2)
C
C
C      open(unit=5,file='GEF:',status='old')
C      read(5,8) Z(1),A(1),Den(1),thick(1)
C      format(1x,4F8.3)
C      if(Z(1).eq.0) stop
C      read(5,10) Z(2),A(2),Den(2),thick(2),sc1,Mgamma,GammaFile,Positronfile
C      format(1x,5F8.3,I10,1x,A30,1x,A30)
C
C      generate the normalized functions giving kinetic energy of positron
C      call ISIG
C
C      Temp=sc1 !MeV
C
C      generate normalized Plank distribution generating function
C      call PLANKgen
C
C      do izi=1,2
C      do m=0,100
C      type *,izi,m,FZE(izi,10,m),XintFze(izi,10,m)
C      enddo
C      enddo
C
C

```

```

do m=0,100
  Igam(m)=0
  iEbin(m)=0
  Pmom(m)=0
enddo

C
C
C
c1=1/sc1 !1/MeV
Emin=10. !MeV

C
C
do icyc=1,Mgamma

C
C
C
      Gamma distribution
44  Egamma = Eplank(RAN(iseed))
      k=Egamma/mc2

C
      iE=Egamma/10.
      m=Egamma/5.
      if( m.gt.100) go to 44
      Igam(m)=Igam(m)+1
      if(iE.gt.99) iE=99

C
C
      interpolate total cross section
      sigTOTAL(1)=(sigT(1,iE+1)-sigT(1,iE))*(Egamma/10.-iE)+sigT(1,iE)
C
C
      conv1=NA/A(1)*Den(1)*sigTOTAL(1) * 1.E-26 !prob/cm
C
C
      Xprob(1)= -log(1-RAN(iseed))/conv1
C
C
      sigTOTAL(2)=(sigT(2,iE+1)-sigT(2,iE))*(Egamma/10.-iE)+sigT(2,iE)
C
C
      conv2=NA/A(2)*Den(2)*sigTOTAL(2) * 1.E-26 !prob/cm
C
C
      Xprob(2)= -log(1-RAN(iseed))/conv2

C
C
      if(Xprob(1).le.thick(1)) then

C
C
      ep=Xeff(1,iE)*(k-2)+1 !mc2 units
      Epos=ep*mc2 !MeV

C
C
      energy loss passing through target
      Epos=Epos-dEdx*Den(1)*(thick(1)-Xprob(1))

C
C
      energy loss passing through converter
      Epos=Epos-dEdx*Den(2)*thick(2)
      if(Epos.lt.mc2) Epos=mc2

C
C
      Xmom=sqrt(Epos**2-mc2**2) !MeV/c
      Xke=Epos-mc2 !MeV

C
C
      m=Xmom/5.
      Pmom(m)=Pmom(m)+1
      m=Xke/5.
      iEbin(m)=iEbin(m)+1

```

```

C
C           else
C           if(Xprob(2).le.thick(2)) then
C
C               ep=Xeff(2,iE)*(k-2)+1 !mc2 units
C               Epos=ep*mc2 !MeV
C
C               energy loss due to converter
C               Epos=Epos-dEdx*Den(2)*(thick(2)-Xprob(2))
C
C               if(Epos.lt.mc2) Epos=mc2
C               Xmom=sqrt(Epos**2-mc2**2) !MeV/c
C               Xke=Epos-mc2 !MeV
C
C               m=Xmom/5.
C               if(m.lt.0 .or. m.gt.100) type *, ' mmmmm=' ,m
C               Pmom(m)=Pmom(m)+1
C               m=Xke/5.
C               iEbin(m)=iEbin(m)+1
C
C           endif
C
C       endif
C
C   enddo
C
C       open(unit=11,file=GammaFile,status='new')
C       open(unit=12,file=PositronFile,status='new')
C
C       do i=2,30
C           E=i*5
C           i1=Igam(i)+1
C           fi1=i1*1./(Mgamma*1.E-6)
C           i2=iEbin(i)+1
C           fi2=i2*1./(Mgamma*1.E-6)
C           write(11,7) E,fi1
C           write(12,7) E,fi2
7       format(3x,F15.7,',',E15.7)
C       enddo
C
C       write(6,88) GammaFile,PositronFile
88       format(5x,A30,5x,A30)
C       close(unit=11)
C       close(unit=12)
C   go to 9
C   end

```

Function Xeff(iel,iEx)

```

C
C   randomly generated Xeff from extrapolated positron yield tables
C
C   common/lookup/ sigT,Fze,XintFze,Egamma
C   dimension sigT(2,100),fze(2,100,0:100),XintFze(2,100,0:100)
C
C   iE=Egamma/10.
C   y=RAN(iseed)
C   i=100/2

```

```
      j=i
      id=i
      do l=1,7
c
        if(XintFze(iel,iEx,i).gt.y) then
              i=i-(id+1)/2
          else
              i=i+(id+1)/2
          endif
c
        if(XintFze(iel,iEx+1,j).gt.y) then
              j=j-(id+1)/2
          else
              j=j+(id+1)/2
          endif

        id=id/2
      enddo
c
      Xeff=( (j-i)*(Egamma/10.-iE) + i )/100.
c
      return
      end
```

```

Subroutine PLANKgen
C
C generates integral of Plank distribution from Egam0
C toward infinity
C
common/Plank/ Xplank,Yplank,Temp
dimension Xplank(0:500),Yplank(0:500)
dimension sto(0:500)
C
C
Egam0=10. !MeV
Emax=500. !MeV
Estep=1. !MeV
C
SUMhv=0
do inh=Egam0,Emax,Estep !MeV
hv=inh
sto(inh)=SUMhv
SUMhv=SUMhv + fhv(hv/Temp)*Estep/Temp
enddo
C
do inh=Egam0,Emax,Estep !MeV
hv=inh
Xplank(inh)= hv
Yplank(inh)= sto(inh)/SUMhv
enddo
C
return
end

function fhv(x)
C
C plank distribution (unnormalized)
C for dN/dEgamma = (dEinterval/dw) * 1/w
C hw = Egamma
C dEinterval = N * hw
C
if(x.lt. 88.) then
fhv=(x**2)/(exp(x)-1.)
else
fhv=0
endif
return
end

```

```

Function Eplank(y)
C
C looks in Xplank,Yplank table made by PLANKgen
C and finds Egamma for 0<y<1
C
common/Plank/ Xplank,Yplank,Temp
dimension Xplank(0:500),Yplank(0:500)
C
C
size=500.
iYtry=size/2
do k=2,13
idY=size/2**k+.5
if(iYtry.lt.0) iYtry=0
if(iYtry.gt.size) iYtry=size
if(Yplank(iYtry).lt.y) iYtry=iYtry+idY
if(Yplank(iYtry).gt.y) iYtry=iYtry-idY
enddo
C
if(iYtry.gt.499) iYtry=499
C
dX=Xplank(iYtry+1)-Xplank(iYtry)
if(Yplank(iYtry+1).ne.Yplank(iYtry)) then
dV=Yplank(iYtry+1)-Yplank(iYtry)
else
dV=1.
dX=0.
endif
delY= Y-Yplank(iYtry)
C
Eplank=Xplank(iYtry) + dX/dV*delY ! gamma energy in MeV
return
end

```

```

C
C SIG(x).....K.Beard 1/9/85
C modified to match GammaEE 1/14/85
C
C finds cross section for a gamma ray of energy "Egamma"
C to covert to a e+/e- pair with positron energy "ep"
C
C x is the fraction of available kinetic energy in the positron
C
C units of SIG fm**2/MeV
C
C uses Bethe-Heitler Formula: Screened Point Nucleus for Extreme-
C Relativistic Energies
C
C eqn 3D-1003 in Rev.Mod.Phy.1968,41,p607
C
C Function SIG(x)
C
C common hv,Ze,Z
C real k,phi1,phi2,mc2,hv,Z(2)
C mc2=.511 !MeV
C alpha=1./137.
C r02=(2.82)**2 !fm**2
C
C k= hv/mc2
C ep=x*(k-2)+1
C em=k-ep
C
C gamma=100*k/(ep*em*(Ze**(1./3.)))
C G = 1.36*gamma
C
C cgamma= 0.5249857*EXP(-0.4980655*gamma)+ 0.01528705
C
C if(G.le.1.) then
C phi1= 20.868 - 3.242*G + 0.625*G*G
C phi2= 20.209 - 1.930*G + 0.086*G*G
C else
C phi1= 21.12 - 4.184*Log(G+0.952)
C phi2= phi1
C endif
C
C if(gamma.lt.2.) then
C
C sigv=alpha*Ze*Ze*r02/k**3 * ( (ep**2+em**2)*(phi1-4*Log(Ze)/3)
1 + 2*ep*em/3 *(phi2-4*Log(Ze)/3) )
C
C else
C
C sigv=4*alpha*Ze*Ze*r02/k**3 *(ep**2+em**2+2*ep*em/3) *
1 (log(2*ep*em/k) - 1./2. - Cgamma)
C
C endif
C
C sigv in units fm**2/mc**2
C
C sig= sigv * 1/mc2
C sig units fm**2/MeV
C
C return
C end

```

```

C
C
C      Isig.....K.Beard 1/9/85
C      modified to match GammaEE      1/14/85
C      corrected                        2/22/85
C      corrected                        2/25/85
C
C      integrates selected pair cross sections and produces
C      a total cross section "sigT" and a normalized (to 1)
C      integrated cross section "fze"
C
C      Subroutine ISIG
C
C      common/lookup/ sigT,Fze,XintFze,Egamma
C      common hv,Ze,Z
C      dimension sigT(2,100),Fze(2,100,0:100),XintFze(2,100,0:100)
C      dimension sto(0:100),Z(2),summ(0:100)
C      real mc2
C
C      mc2 = .511 ! MeV
C
C      do m=1,2
C      do i=1,100
C      hv=i*10. !MeV
C
C          Ze=Z(m)
C          sigT(m,i)=0.
C          do j=0,100
C          y=j/100.
C          sto(j)=sig(y)
C          dEplus = (hv - 2*mc2)/100
C          sigT(m,i)= sigT(m,i) + sto(j)*dEplus
C          enddo
C          sumSto=0.
C          do j=0,100
C          sumSto=sumSto+sto(j)
C          summ(j)=sumSto
C          enddo
C          do j=0,100
C          Fze(m,i,j)=sto(j)/sumSto
C          XintFze(m,i,j)=summ(j)/sumSto
C          enddo
C
C      enddo
C      enddo
C      return
C      end

```

## List of References

- A185 J. Aichelin, private communication
- Ag82 M. Aguilar-Benitez, R. I. Crawford, R. Frosch, G. P. Gopal, R. E. Hendrick, R. I. Kelly, M. J. Losty, L. Montanet, F. C. Porter, A. Rittenberg, M. Roos, L. D. Roper, T. Shimada, R. E. Shrock, T. G. Trippe, Ch. Walck, C. G. Wohl, G. P. Yost, and B. Armstrong, "Particle Properties Data Booklet", 25th Ed., Lawrence Berkely Laboratory, Berkeley, 1982
- Ba86 W. Bauer, W. Cassing, U. Mosel, M. Iohyama, "High Energy  $\gamma$ -Ray Emission in Heavy-Ion Collisions", to be submitted to Nuclear Physics
- Be70 D. B. Beard and G. B. Beard, "Quantum Mechanics with Applications", Allyn and Bacon, Inc., Boston, 1970
- Be79 W. Benenson, G. Bertsch, G. M. Crawley, E. Kashy, J. A. Nolen, Jr., H. Bowman, J. G. Ingersoll, J. O. Rasmussen, J. Sullivan, M. Koike, M. Sasao, J. Péter, and T. E. Ward, Phys. Rev. Lett. 43, (1979) 683
- Be80 K. B. Beard, code SPECKINEX, National Superconducting Cyclotron Laboratory, (1980)
- Be82 K. B. Beard, J. Kasagi, E. Kashy, and B. H. Wildenthal, D. L. Freisel, H. Nann, and R. E. Warner, Phys. Rev. C 26, (1982) 720
- Be84 W. Benenson, private communication
- Be85a W. Benenson, private communication
- Be85b G. Bertsch, private communication
- Bi83 Bicron Corporation, "Premium Plastic and Liquid Scintillators"
- Br84 P. Braun-Munzinger, P. Paul, L. Ricken, J. Stachel, P. H. Zang, G. R. Young, F. E. Obenshain, and E. Grosse, Phys. Rev. Lett. 52, (1984) 255

- Br84a C.Bromberg, private communication
- Bu81 M.P.Budiansky, Ph.D. thesis, University of California, Berkeley, 1981.
- Bu82 M.P.Budiansky, S.P.Ahlen G.Tarle, and P.B.Price, Phys. Rev. Lett 49, (1982) 361
- Ga48 E.Gardner and C.M.G.Lattes, Science 107, 270 (1948)
- Gl71 J.E.Glenn, C.D.Zafiratos, and C.S.Zaidins, Phys. Rev. Lett. 26, (1971) 328
- Gs50 H.Goldstein,"Classical Mechanics", Addison-Wesley Publishing Company, Inc., Reading, Massachusetts, 1950
- Go77 J.Gosset, H.H.Gutbrod, W.G.Meyer, A.M.Poskanzer, A.Sandoval, R.Stock, and G.D.Westfall, Phys. Rev. C 16, (1977) 629
- Gr82 M.C.Green,"Pion Production and Absorption in Nuclei-1981", Conference on Pion Production and Absorption in Nuclei, AIP Conf. Proc. No. 79, edited by Robert D. Bent (AIP, New York, 1982)
- Ha85a D.Hahn, private communication
- Ha85b D.Hahn and H.Stöcker, preprint #MSUCL-505, Michigan State University, (1985)
- Ha85c B.E.Haselquist, G.M.Crawley, B.V.Jacak, Z.M.Koenig, G.D.Westfall, J.E.Yurkon, R.S.Tickle, J.P.Dufour, and T.J.M.Symons, Phys. Rev. C 32, (1985) 145
- He84 H.Heckwolf, E.Grosse, H.Dabrowski, O.Klepper, C.Michel, W.F.J.Müller, H.Noll, C.Brendel, W.Rösch, J.Julien, G.S.Pappalardo, G.Bizard, J.L.Laville, A.C.Mueller, and J.Péter, Zeitschrift für Physik A315, (1984) 243
- Hu84 C.Hurlburt, Bicron Inc., private communication
- Ja75 J.D.Jackson, "Classical Electrodynamics", Second Edition, John Wiley & Sons, New York, (1975)
- Ja76 R.Jahn,G.J.Wozniak,D.P.Stahel, and J.Cerny, Phys. Rev. Lett. 37, (1976) 812
- Ko85 C.M.Ko, G.Bertsch, and J.Aichelin, Phys. Rev. C 31, (1985) 2324

- Kr86 J.F.Krebs, J.-F.Gilot, P.N.Kirk, G.Claesson, J.Miller, H.G.Pugh, L.S.Schroeder, G.Roche, J.Vincente, K.Beard, W.Benenson, J.van der Plicht, B.Sherrill, J.W.Harris,  
"Subthreshold Negative Pions and Energetic Protons Produced at  $\theta_{C.M.} = 90^\circ$  in 246 MeV/nucleon  $^{139}\text{La} + ^{139}\text{La}$  Collisions", LBL-18267 Preprint, submitted to Phys. Lett. B
- Le67 C.M.Lederer, J.M.Hollander, and I.Perlman,  
"Table of Isotopes", 6th Ed.,  
John Wiley & Sons, Inc., New York, (1967)
- Li80 U.Littmark and J.F.Ziegler,  
"Handbook of Range Distributions for Energetic Ions in All Elements", Vol. 6, Pergamon Press, New York, 1980
- Ma69 Pierre Marmier and Eric Sheldon, "Physics of Nuclei and Particles", Vol. I, Academic Press, New York, 1969
- Ma79 R.G.Markham,  
Nucl. Instr. and Meth. 162, (1979) 327
- Mo69 J.W.Mothz, H.A.Olsen and H.W.Koch,  
Rev. Mod. Phys 41, (1969) 581
- Ni85 H.Nifenecker and J.P.Bondorf,  
Nuclear Physics A442, (1985) 478
- No76 W.Nörenberg and H.A.Weidenmüller,  
"Introduction to the Theory of Heavy-Ion Collisions",  
Springer Verlag, Berlin, 1976
- No84 H.Noll, E.Grosse, P.Braun-Munzinger, H.Dabrowski, H.Heckwolf, O.Klepper, C.Michel, W.F.J.Müller, H.Stelzer, C.Brendel, and W.Rösch,  
Phys. Rev. Lett. 52, (1984) 1284
- No85 H.Noll, Gesellschaft für Schwerionenforschung,  
Report No. GSI-85-9, 1985 (ISSN No. 0171-4546)  
(unpublished)
- Nu72 Nuclear Enterprises, Inc.  
"Plastic Scintillators, Light Pipes and Cerenkov Detectors"
- Pr75 M.A.Preston and R.K.Bhaduri,  
"Structure of the Nucleus"  
Addison-Welsey Publishing Company, Inc., Reading, Mass. (1975)

- Rc73 RCA Electronic Components  
"Photodetector 8575", RCA 1973
- Re83 B.Remington, G.Crawley, A.Galonsky, J.Kasagi, A.Kiss,  
and Z.Seres, "The Neutron Chamber and Beam Line",  
Annual Report of the Michigan State University  
Cyclotron Laboratory, 1982-83
- Ri50 C.Richman and H.A.Wilcox, Phys. Rev. 78, (1950) 496
- Ri65 F.Rief,  
"Fundamentals of Statistical and Thermal Physics"  
McGraw-Hill Book Company, New York, 1965
- Ro77 L.Robinson,  
"A High Resolution, Nodular Resistive Wire Counter",  
Annual Report of the Michigan State University  
Cyclotron Laboratory, 1976-1977
- Sa77 F.Sauli,  
"Principles of Operation of Multiwire Proportional  
and Drift Chambers", CERN, Geneva, 1977
- Sa85 SAMTEC  
SAMTEC Strip Products Catalog S-83  
New Albany, Indiana, (1983)
- Sh83 B.Sherrill, K.Beard, W.Benenson, B.A.Brown, E.Kashy,  
W.E.Ormand, H.Nann, J.J.Kehayias, A.D.Bacher, and  
T.E.Ward,  
Phys. Rev. C 28, (1983) 1712
- Sh84a R.Shyam and J.Knoll  
Phys. Lett. 136B, (1984) 221
- Sh84b R.Shyam and J.Knoll  
Nucl. Phys. A426, (1984) 606
- Sh85 B.M.Sherrill, Ph.D. thesis,  
Michigan State University (1985)
- Sh86 R.Shyam and J.Knoll  
Nucl. Phys. A448, (1986) 322
- Sp67 J.E.Spencer and H.A.Enge,  
Nucl. Instr. and Meth. 49, (1967) 81
- St79 D.P.Stahel, R.Jahn, G.J.Wozniak, and J.Cerny,  
Phys. Rev. C 20, (1979) 1680
- St84 J.Stevenson, private communication

- St85a J.Stachel, P.Braun-Munzinger, R.H.Friefelder, P.Paul, S.Sen, P.DeYoung, P.H.Zhang, T.C.Awes, F.E.Obershain, F.Piasil, G.R.Young, R.Fox, and R.Ronnigen, preprint #25.79.-Z, University of New York at Stony Brook, (1985)
- St85b J.Stevenson, private communication
- St85c J.Stevenson,"High Energy  $\gamma$ -rays and Electron-Positron Pairs from Heavy Ion Collisions at  $E/A=40$  MeV", invited talk at the 1985 Fall Meeting of the Division of Nuclear Physics, American Physical Society
- Ti81 R.Tickle,G.Crawley,W.G.Lynch,M.B.Tsang, and J.Yurkon "Construction of a Multiwire Proportional Chamber", Annual Report of the Michigan State University Cyclotron Laboratory, 1980-1981
- Va84 D.Vasak, W.Greiner, B.Muller, Th.Stahl, and M.Uhlig, Phys. A428, (1984) 291c
- Vi79 Viking Connectors, Condensed Catalog, Chatsworth, California, (1979)
- We73 R.Weidner and R.Sells,"Elementary Modern Physics", Alternate Second Edition, Allyn and Bacon, Inc., Boston, 1973
- We81 R.C.Weast and M.J.Astle, "CRC Handbook of Chemistry and Physics", 62nd Ed., CRC Press Inc., Baco Raton, 1981

MICHIGAN STATE UNIVERSITY LIBRARIES



3 1293 03082 8895